https://dx.doi.org/10.1016/j.enconman.2022.116342

Potential Passive Cooling Methods based on Radiation Controls in Buildings

Yin Hoi Chan [a], *Yi Zhang* [b], *Thilhara Tennakoon* [b], *Sau Chung Fu* [a], *Ka Chung Chan* [b], *Chi Yan Tso* [c], *Kin Man Yu* [d], *Man Pun Wan* [e], *Bao Ling Huang* [f], *Shu Huai Yao* [f], *Hui He Qiu* [f], *Christopher Yu Hang Chao*[*a,g]

[a] Department of Building Environment and Energy Engineering, The Hong Kong Polytechnic University, Hong Kong, China

[b] Department of Mechanical Engineering, The University of Hong Kong, Pokfulam, Hong Kong, China

[c] School of Energy and Environment, City University of Hong Kong, Tat Chee Avenue, Kowloon, Hong Kong, China

[d] Department of Physics, City University of Hong Kong, Tat Chee Avenue, Kowloon, Hong Kong, China

[e] School and Mechanical and Aerospace Engineering, Nanyang Technological University, 639798, Singapore

[f] Department of Mechanical and Aerospace Engineering, The Hong Kong University of Science and Technology, Clear Water Bay, Kowloon, Hong Kong, China

[g] Department of Mechanical Engineering, The Hong Kong Polytechnic University, Hong Kong, China

* Corresponding author E-mail address: christopher.chao@polyu.edu.hk (Christopher Yu Hang Chao)

Abstract

Buildings inevitably absorb solar (thermal) radiation through the envelope, i.e., window, roof and wall, whose characteristics, in terms of material, thickness, area etc., affects the performance of space cooling, thereby inducing energy wastage by air-conditioning system to maintain satisfied indoor thermal comfort. Metropolises with congested-built architectures and humid climates consume tremendous energy in space cooling, contributing to massive carbon emissions. Space cooling has been the most soaring electricity end-user and its increasing carbon emission amplifies global warming, which in turn increases occupants' dependence on artificial cooling, especially in hot climates. The urgency of the climate crisis has put passive cooling technologies, which can efficiently manage heat transfer of buildings, to the forefront of research. Thermochromic smart windows, daytime radiative coolers and reflective paints are three prominent technologies that have drawn industries' attention. These technologies respond to incident sunlight and thermal radiation differently, compared to conventional building envelope, and can passively mitigate solar radiation absorbed at the building envelope, reducing electricity consumption for air-conditioning. This review article comprehensively discusses the characteristics of the three passive energy-efficient techniques that can be integrated with building façade (window, roof and wall), and their feasibility in building cooling applications through thermal analyses. Through this review, the ideal spectral properties of these technologies will be distinguished. Although the properties of these technologies have been abundantly explored, the research on their long-term cooling performance under the influence of weatherability and aging remains scarce. Further, their cost-effectiveness is essential for realizing commercialization and reducing hesitancy in adopting these novel passive cooling technologies for taking a significant leap towards carbon neutrality.

Keywords: Thermochromic smart window, Daytime radiative cooling, Reflective coatings,

Passive cooling, Building energy saving, Radiation control

Nomenclature

WWR	Window-to-wall ratio
IR	Infrared
NIR	Near-infrared
UV	Ultraviolet
λ	Wavelength
R	Reflectance of material
TCW	Thermochromic smart window
T_{lum}	Luminous transmittance
$T_{lum,l}$	Luminous transmittance in the cold state of thermochromic window
$T_{lum,h}$	Luminous transmittance in the hot state of thermochromic window
T_{sol}	Solar transmittance
ΔT_{sol}	Solar modulation ability
SHGC	Solar heat gain coefficient
T_c	Critical/transition temperature
LCST	Lower critical solution temperature
LSPR	Localized surface plasmon resonance
PNIPAm	Poly(N-isopropylacrylaminde)
HPC	Hydroxypropyl cellulose
IL	Ionic liquid
LC	Liquid crystal
DPRC	Daytime passive radiative cooler
AW	Atmospheric window
P_{net}	Net cooling power
P_{rad}	Radiative flux emitted by the daytime passive radiative cooler
P_{atm}	Atmospheric radiation at ambient air temperature
T_a	Ambient air temperature
P_{sun}	Solar radiation absorbed
P_{cond}	Conductive heat gain (non-radiative heat transfer)
P_{conv}	Convective heat gain (non-radiative heat transfer)
A	Surface area of daytime passive radiative cooler
ε_{atm}	Atmosphere's spectral emissivity
PDMS	Polydimethylsiloxane
PTFE	Polytetrafluoroethylene
PMMA	Poly(methyl-methacrylate)
NP	Nanoparticle
e_{in}	Emissivity within the atmospheric window
e_{out}	Emissivity outside the atmospheric window
A_{sol}	Solar absorptance
TP	Thermochromic pigment
TC	Thermochromic paint
HGM	Hollow glass microsphere
HGB	Hollow glass bead
R_{NIR}	Reflectance in the near-infrared spectrum
R_{sol}	Reflectance in the solar spectrum
TSR	Total solar reflectance
WCA	Water contact angle
WSA	Water slide angle

1. Introduction

Building, as a shelter for various functions, is required to provide thermal and bodily comfort for occupants in terms of mean radiant temperature, air temperature and humidity etc. [1] To maintain thermal comfort, air-conditioning is indispensable especially for buildings in tropical climates, for instance, it is responsible for 28% of the total electricity consumption in Hong Kong [2]. Cooling demand is considerably affected by the building materials and their heat gain [3, 4], owing to building façade, viz. window, wall and roof, being the most influential variables that constitute about 50% of heat gain of a building (average window fraction: 30%) [5]. Thus, an energy-ineffective façade can lead to excessive cooling and eventually energy wastage of air-conditioning system. Additionally, architectural design, e.g., window-to-wall ratio (WWR) has been substantiated to influence space cooling [6], especially for skyscrapers. It was revealed that higher WWR induces higher cooling demand (in warm climates and cooling period) to overcome the solar radiation gain through the increased window area [7].

The fundamental heat transfer mechanisms in a building includes conduction, convection and radiation. Examples of notable techniques that can actively and passively regulate building heat transfer are tabulated in Table 1. Convention can be enhanced by exploiting passing wind stream as natural ventilation to reduce cooling demand. Yet, this method requires holistic architectural design approaches such as wing walls and thermal chimney, and the effectiveness is limited depending on the geographical location and building types. In addition, the excellent thermal insulation of materials like glass wool and expanded polystyrene have been proved by being widely adopted in buildings for decades. William et al. [5] analyzed the energy performance of a building with envelope of different materials: extruded polystyrene, polyurethane and glass wool, of different thicknesses, and reflective paint, in three cities of Egypt using simulation software. The results revealed that reflective paint achieved the greatest energy saving and carbon reduction among all materials. The major difference between

reflective paint and the other investigated materials is that the former directly interacts with solar radiation, as it is applied on the outer surface of the building façade (roof and exterior walls). Incident solar radiation (insolation) is an unavoidable heat source from the external environment into a building, which is the main source of heat that associates with the building's external surface; ergo, it is another key factor that affects cooling (and heating) demand, apart from the selection of building material. The energy of incident solar radiation consists of approximately 47% of visible light (0.38 μm ≤ λ ≤ 0.78 μm), 46% of infrared (IR) (λ > 0.78 μm) and 7% of ultraviolet (UV) (λ < 0.38 μm) [8]. It is noteworthy that IR-radiation is the major energy source, i.e., the heating-generating spectrum. Additionally, the temperature difference between objects can lead to sharp increase in radiation exchange [1], and thus reducing insolation absorbed in the form of heat and material selection are crucial. Another imperative factor is that whether additional electricity input is required to reduce the solar heat gain, which may exacerbate the electricity use, leading to usage restriction of the technique depending on factors such as building type and operating form. Hence, passivity is desired to feasibly utilize the technologies in various buildings, while avoiding the possibility of increasing electricity use. In short, solar radiation and passivity are the two critical keywords for developing cooling technologies in buildings, and therefore, are the focus of this review paper.

Table 1. List of technologies for building energy-saving.

Type	Facade	Passive/Active	Application
Low-emissivity coating	Window	Passive	Between glass panels inside glazing unit
Multilayer glazing units	Window	Passive	Conventional method for thermal insulation
Thermochromic Smart Window	Window	Passive	Advanced glazing unit
Electrochromic Smart Window	Window	Active	Advanced glazing unit
Photochromic Smart Window	Window	Passive	Advanced glazing unit
Radiant Barrier	Roof	Passive	On the underside of roof
Daytime Radiative Cooler	Roof	Passive	On external surface of roof facing outdoor
Insulation materials	Roof, Wall	Passive	Between/inside envelopes to reduce heat exchange through envelopes
Green Façade	Roof, Wall	Passive	On external surface to mainly control

Reflective Paint	Roof, Wall	Passive	conduction/convection Directly interact with incident sunlight

Building façade is one of the most paramount elements of a building as it serves as a barrier that offers protection against external environment and weather events, such as rain, wind, sun, etc., which could damage the building structure. This review paper discusses some of the particularly prevailing technologies that are passive (without additional electricity input) and promising for mitigating solar radiation (heat) gain by integrating with building envelope:

(1) Window (Section **3**): thermochromic smart window, whose optical properties change by temperature variation, is an advanced glazing that selectively allows sunlight into buildings to reduce solar heat gain, while allowing interaction with the outdoor;

(2) Roof (Section **4**): radiative cooler on roofs can reflect incident sunlight and emit thermal radiation to the outer space in the atmospheric window (8-13 μm);

(3) Roof & Wall (Section **5**): reflective paints on roof and exterior walls absorb less near-infrared (NIR) radiation, in other words, have higher reflectivity compared to conventional paints.

Fig. 1a summarizes the passive technologies of diverse base materials that will be introduced in terms of the respective building membranes they can be incorporated with. It is noted that the "wall" mentioned in this review merely refers to external wall, and the reviewed technologies are to be applied on the outermost layer of the building façade (outdoor).

Recent advancements in cooling technologies are well documented in erstwhile published reviews, yet their focus has been on the design approach of existing technologies, and less on their integration with buildings [9-11]. In particular, some reviews that report on the application aspects of passive radiative cooling in buildings make only cursory references to selective photonic cooling apparatus as they cover both nocturnal and diurnal radiative cooling [12] and/or focus on cool roofs that are made of bulk materials, but not the latest DPRC material

[13]. Moreover, while it is vital to consider the materials used and spectral properties carefully, it is equally important to corroborate the cooling performance of the technologies with thermal analysis. Therefore, this work will:

(1) introduce three potential passive cooling technologies: thermochromic smart windows, daytime passive radiative coolers and reflective paints, which can mitigate solar heat gain at building façade,

(2) characterize their spectral properties that describe the response of the technologies/materials to incident solar radiation within different spectrums: UV, visible light and IR, and determine the favorable spectral properties of each technology,

(3) present thermal analyzes and compare their thermal properties that endorse the feasibility in cooling applications,

(4) identify their current research hotspot and focuses on the studies conducted over the past decade to foresee their future development with reported economic analyses, and

(5) more importantly, shed a light on the perspectives of passive energy-efficient technologies and requirement that shall be fulfilled to passively reduce incident solar radiation into buildings, providing a prominent direction to achieve net zero building design.

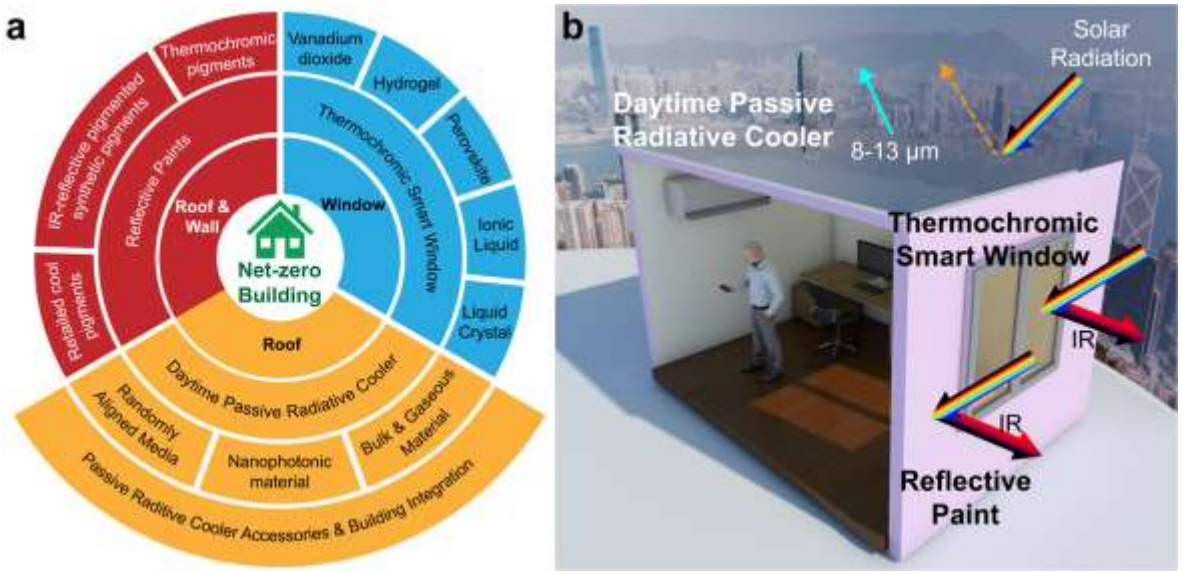

Fig. 1. a) Summary and b) illustration of passive cooling technologies for incorporating with different building membranes: (1) window, (2) roof and (3) roof & wall introduced in this review.

2. Methodology of Thermal Analysis

The cooling effect of materials can be investigated via three methods: (1) laboratory experiment (indoor), (2) field experiment (outdoor) and (3) energy simulation under different conditions. Among which, indoor and field experiments are widely used by simply measuring the temperature difference between developed and conventional materials under irradiation of solar lamp or natural sunlight to directly examine the feasibility of reflective materials in reducing solar heat transmitted into buildings. Fig. 2 illustrates how field experiment can be conducted for the three passive cooling technologies. As daytime passive radiative coolers (DPRCs) require the presence of the cold universe that acts as heat sink, they must be placed on roof facing the sky, while the other two technologies, thermochromic smart windows (TSWs) and reflective paints can be applied on multiple external surfaces at different orientation. Thermocouples are attached to the surfaces of substrates (surface temperature) and/or inside setup (interior air temperature) to measure and record the temperature profile under direct sunlight. Although laboratory and field experiment are straightforward evaluation methods, their duration generally last from an hour to few months [14-16], thereby the long-term cooling effect (a year or above) is unknown. More importantly, the energy performance of buildings with passive cooling technologies under different climates is not rigorously examined. EnergyPlus, developed by Lawrence Berkeley National Laboratory [17], is an example of energy simulation software that can estimate the year-around energy performance/improvement of buildings by changing the properties and materials of envelopes with respect to reference model. Simulation studies consider various factors like building types

and climate that are crucial in determining cooling demand. For instance, in the cases of TCWs, the optical properties and total window thermal performance indices, which are calculated by Optics and WINDOW computer program, can be imported to simulate the energy consumption of simulation model with TCWs. There is a built-in thermochromic glazing module that allows users to define the TCW's properties at different temperatures; when the simulation is running, the glazing layer switches between the hot and cold states depending on its surface temperature. The model considers heat transfer across the building envelope and internal loads including occupants, interior lighting and equipment, determining its temperature at a given instance.

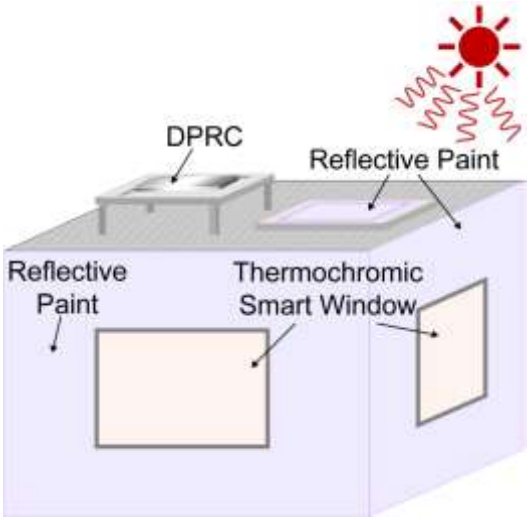

Fig. 2. Illustration of conducting field experiment for examining thermal performance of the three reviewed passive cooling technologies: daytime passive radiative cooler (DPRC), thermochromic smart window and reflect paint, under natural sunlight.

3. Window: Thermochromic Smart Window

Windows are the openings in architectures that provide visual comfort, air-ventilation, daylighting and some degree of heat control, yet achieving all these requirements is rather difficult. The thermal performance of ordinary windows is poor and significantly affects the energy demand of buildings. In typical houses, roughly one-third of the total heat loss passes

through the glazing [18]. For example, in summer, the radiation transmitted to indoor through windows is assumed to be entirely absorbed, by virtue of the cavity effect. The warming interior surfaces in turn warm the air in the room and radiate heat to its occupants. Therefore, most of the cooling load is due to the solar heat gain though glazing. However, sunlight is preferred to enter and light up indoor spaces. Present architectural trends are to increase the window areas such that the energy issue may become even more pressing in the future. Therefore, regulating heat penetration through windows is an important consideration in building designs. That is why the dynamic control of sunlight is termed as "Holy Grail of the Fenestration Industry" [19].

Smart windows are such kinds of advanced technologies that can dynamically modulate the solar radiation, and therefore can be used to mitigate the energy loss for space cooling. Smart windows are coated with materials, whose light transmittance in a certain range of solar radiation such as UV, visible, and NIR can be tuned dynamically and reversibly in a "smart way". For smart windows, light transmission properties can be controlled by the application of voltage (electrochromism) [20], light (photochromism) [21], or heat (thermochromism) [22]. Among which, thermochromism is the property of substances that change their color, owing to change in temperature. Thermochromic smart window (TCW) is highly competitive due to its unique characteristics: low cost, passivity (electrochromism needs energy/electricity input) and rational stimulus response [23]. A window that changes its color when the ambient temperature is high is desired for cooling indoors, while photochromism is relatively less suitable than thermochromism as solar irradiance is not directly related to ambient temperature. TCWs have higher transparency in cold weather to allow solar radiation to enter rooms for heating (clear/cold state) and lower transparency in hot weather to block sunlight for cooling (tinted/hot state). Besides the radiation control, it is also necessary to diminish the non-radiative (conductive and convective) heat transfer, which is possible in evacuated vacuum glazing.

This review will only focus on TCWs and not include dual-mode smart windows, where the thermochromic system integrates with other solar modulation systems such as electrochromism. Materials for producing TCWs include vanadium dioxide, hydrogel, perovskites, ionic liquids, and liquid crystals. Among these, ionic liquids, liquid crystals and perovskites thus far can only tune visible light. Vanadium dioxide is suitable for tuning NIR, and hydrogels can achieve simultaneous tuning in the visible and NIR spectrum.

Luminous transmittance (T_{lum}) and solar modulation ability (ΔT_{sol}) are the two most important indices in the TCW field [24]. They are more commonly used in smart window research than U-value and solar heat gain coefficient (SHGC). T_{lum} is used to quantify the ratio of visible light transmitted by the windows that is useful for human vision under normal conditions and is defined in Equation (1). Similarly, T_{sol} quantifies the ratio of solar thermal energy entering a building via solar transmittance and is defined in Equation (2). The solar modulation ability is then defined in Equation (3) as ΔT_{sol}.

$$T_{lum} = \frac{\int_{\lambda=380\ nm}^{780\ nm} \bar{y}(\lambda)T(\lambda)d\lambda}{\int_{\lambda=380\ nm}^{780\ nm} \bar{y}(\lambda)d\lambda}, \quad (1)$$

$$T_{sol} = \frac{\int_{\lambda=300\ nm}^{2500\ nm} AM_{1.5}(\lambda)T(\lambda)d\lambda}{\int_{\lambda=300\ nm}^{2500\ nm} AM_{1.5}(\lambda)d\lambda}, \quad (2)$$

$$\Delta T_{sol} = T_{sol}^{cold} - T_{sol}^{hot} \quad (3)$$

where $T_{lum}(\lambda)$ is the luminous (visible) transmittance of the window at wavelength, λ, and the waveband for calculation is 380 nm $\leq \lambda \leq$ 780 nm, corresponding to the limits of human vision. $T_{sol}(\lambda)$ is the solar transmittance of windows at wavelength, λ and the waveband for calculation is 300 nm $\leq \lambda \leq$ 2500 nm. The CIE (International Commission on Illumination) standards for photopic luminous efficiency of human eye, ($\bar{y}(\lambda)$), and solar irradiance spectrum for an air mass of 1.5, $AM_{1.5}(\lambda)$, are used as weighting functions for the wavelength dependent

transmittance.

High T_{lum} windows can give residents both positive and negative experiences [25]. On the one hand, the primary role of a window is to provide a visual portal for residents to external environments. Additionally, a high transmittance is needed to save energy for lighting during daytime. On the other hand, more daylight through high T_{lum} windows is accompanied by increased solar gains (thermal discomfort in summer) and glare, which is a source of visual discomfort and defined as the contrast lowering effect within a visual field, due to the presence of bright light sources [26]. ΔT_{sol} has a strong relationship with the energy saving potential of a smart window and larger solar modulation is especially helpful in warm climate, where cooling demand dominates.

Some commercial window techniques, float glass for instance, have been employed in most buildings. Since iron oxide (Fe_2O_3) is added during the fabrication process, float glass has a characteristic absorption at the wavelength of 1 μm, which can slightly reduce T_{sol}. Other commercial windows for statically regulating solar energy are low-emissivity windows and solar control windows. Low-emissivity windows have high transmittance from 0.38 μm to 3 μm, and high reflectance in the 3 μm to 50 μm range, while solar control windows have high transmittance only in the 0.38 μm to 0.78 μm range, and high reflectance from 0.78 μm to 50 μm.

3.1. Vanadium Dioxide-based Smart Window

A number of transition metal oxides show thermochromic property owing to metal insulator transitions taking place at a well-defined critical temperature (T_c) [27]. Vanadium dioxide (VO_2), whose thermochromism was first reported in 1959 [28], is the most extensively studied material for smart windows because its thermochromic behavior happens at a tunable critical

temperature, T_c [29]. When the temperature is lower than the T_c, VO_2 has a monoclinic crystal structure and is electrically insulating due to the localization of the outer-shell vanadium electrons from the dimerization of vanadium ions [30]. When above the T_c, the VO_2 lattice relaxes to a rutile structure and its electrical conductivity rapidly increases up to ~5 orders. Simultaneously, the reversible phase transition of VO_2 also involves an abrupt change in NIR transmittance, which makes VO_2 an attractive candidate for smart window applications. This transition can be highly repeatable in a thin film and the change of structure can happen in the picoseconds to femtoseconds range [31]. However, the transition time in a practical window is limited by the heat capacity of the substrate and pure VO_2 has some intrinsic drawbacks for smart window application. (1) Due to absorption in the visible range in both semiconducting and metallic states, VO_2 has a low T_{lum} of less than 50%, which is too low for most applications in architecture [32]. Although the VO_2 film would be more transparent if it were thinner than 50 nm, such films show lowered ΔT_{sol}. (2) Energy saving using VO_2 TCWs is not efficient because of its low ΔT_{sol}. The typical value is only 5% for VO_2 film. (3) VO_2 has high T_c of ~68°C, which is too high for buildings. Other challenges include the intrinsic yellow-brown color of the material, its low resistance to oxidization and laborious control of the fabrication process. VO_2 TCWs have attracted much attention since the concept was reported in 1985 [33]. Since then, arduous efforts have been made to improve the low T_{lum} and ΔT_{sol} of VO_2, including chemical doping, anti-reflection coatings, micro-nanopatterned films, and nanocomposites.

3.1.1. Chemical Doping

To deal with the high T_c, researchers have found that doping with some metal ions of high valence can greatly decrease T_c close to room temperature. For example, Jin et al. [34] studied the relationship between tungsten (with a high valence state of 6+) concentration and the T_c. It was found that doping with tungsten linearly decreased T_c by 23°C for each increase in the

atomic percentage of tungsten as shown in Fig. 3a, and significantly reduced the thermal hysteresis loop width in the temperature against transmittance graph [34]. Scientist have used different fabrication methods including chemical vapor deposition [35], reactive radio-frequency (RF)-sputtering [36], reactive ion-beam sputtering [37], reactive DC magnetron sputtering [38], and sol-gel method [39], to demonstrate that doping tungsten can decrease T_c. The amount of tungsten for doing this seems to depend on the degree of crystalline order in the VO_2 but the relationship is not well understood [32]. However, the thermochromism of the films is crucially affected after doping. A significant number of defects in the crystal lattice will greatly degrade the optical properties [40], thus T_{lum} and ΔT_{sol} will dramatically decrease. Li et al. [41] found that doping magnesium (Mg) into VO_2 thin film can simultaneously increase luminous transmittance in the cold state, $T_{lum,l}$, from 45.3% to 47.5% and ΔT_{sol} (from 11.6% to 12.8%). Likewise, Mlyuka et al. [42] lowered the T_c of their developed films by ~3 K/at. %Mg (Fig. 3b). The low T_{lum} is partly due to the strong optical absorption at < 500 nm, which is connected with the small optical band gap of VO_2. The addition of Mg^{2+} led to band gap widening in proportion to the degree of doping therefore the T_{lum} increases. However, the T_c could only be reduced to 47°C even at a high doping level. Therefore, Wang et al. [43] co-doped tungsten and magnesium in VO_2, and a good combination of low T_c (~35°C) and high T_{lum} (81.3%) was achieved. Please note that if there is no specification, T_{lum} means the average luminous transmittance in the cold state, $T_{lum,l}$, and hot state, $T_{lum,h}$.

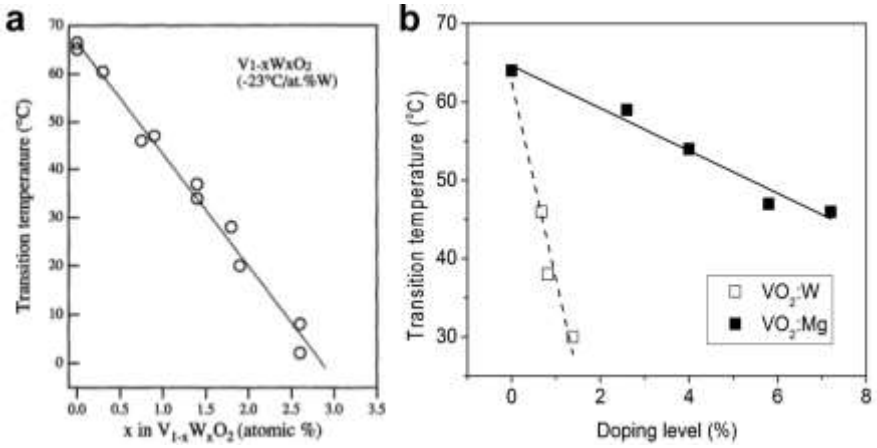

Fig. 3. a) T_c versus x for the $V_{1-x}W_xO_2$ films [34]. b) T_c versus x for 50 nm thick $V_{1-x}Mg_xO_2$ films [42].

3.1.2. Anti-reflection Coatings

Anti-reflection coatings have been invented to reduce reflection and increase the transmittance in many fields, such as camera lens, eyeglass lens, and solar cells. Designed anti-reflection coatings have also been applied to VO_2 TCWs to increase the T_{lum}. The principle of the anti-reflection coating can be explained by destructive interference of two reflected light beams from air-coating and coating-substrate interfaces, thereby canceling each other and increasing the transmittance. Jin et al. designed a window composed of VO_2 film with TiO_2 antireflection coating [44]. A TiO_2 (40 nm)/VO_2 (50 nm) structure was optimized, and the maximum $T_{lum,l}$ increased from 32.3% to 47.2% and ΔT_{sol} increased from 4.41% to 6.99%. Later, Jin et al. [45] and Mlyuka et al. [29] designed a three-layer structure ($TiO_2/VO_2/TiO_2$) and a five-layer structure ($TiO_2/VO_2/TiO_2/VO_2/TiO_2$), respectively. The films were made by reactive DC magnetron sputtering. $TiO_2/VO_2/TiO_2$ films displayed T_{lum} significantly higher than that of bare VO_2 films (from 43.5% to 60.4%) as depicted in Fig. 4a, and $TiO_2/VO_2/TiO_2/VO_2/TiO_2$ films could yield a large ΔT_{sol} (from 6.7% to 12.1%). TiO_2 can also yield desirable multifunctionality and serve as a photocatalytic, self-cleaning and superhydrophilic layer. Xu et al. [46] deposited

a ZrO_2 layer on a VO_2 thin film as an anti-reflection layer. The ZrO_2 has two functions: (1) suppress reflectance and (2) shift transmission peak to the vicinity of wavelength with maximum luminous efficiency for photopic vision, resulting in an improvement of T_{lum} from 32.3% to 50.5%. More recently, Liu et al. [47] used refractive index-tunable anti-reflection coatings as illustrated in the inset figure of Fig. 4b. VO_2 has a higher refractive index (RI) at low temperature than at high temperature for most visible and NIR ranges, which causes higher Fresnel reflection at the lower temperature and is one of the main reasons that lead to intrinsically low ΔT_{sol}. Therefore, more antireflection offered in the cold state can maximize ΔT_{sol}. The transmittance spectra with and without the antireflection layer are shown in Fig. 4b. The best performing window has a maximized ΔT_{sol} (from 6.6% to 11.3%) and increased T_{lum} (from 39.9% to 55.4%) simultaneously.

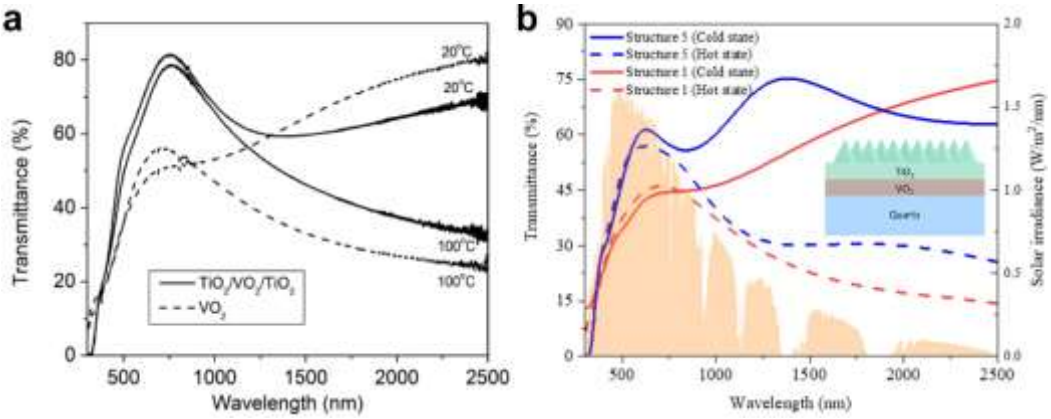

Fig. 4. a) Transmittance of three-layer $TiO_2/VO_2/TiO_2$ films [29]. b) Transmittance spectra of VO_2 TCWs with and without the anti-reflection layer. The inset figure is the cross-section of the nano-cone anti-reflection coating [47].

3.1.3. Micro-/nano-patterned films:

Various micro-/nano-patterned structures have been utilized to enhance the optical performance of VO_2 TCWs, including T_{lum}, ΔT_{sol}. In this review, we will briefly introduce two structures:

the nanopore-structured and nanocone-structured. The inclusion of nanopores in VO_2 films serves to decrease RI and extinction coefficient, in conjunction with the optimization of material thickness. This results in the depression of reflection in both the visible and IR regions, overcoming the physical limitations of continuous films. Liu et al. [48] introduced an orderly-patterned nano-holes structure into VO_2 thin film, and used Finite Difference Time Domain (FDTD) simulations to optimize the thin film parameters. They found the best performing results of T_{lum} and ΔT_{sol} to be 76.7% and 14.0%, respectively, by varying the film thickness, cell periodicity, grid dimensions and variations of grid arrangements. Later, based on simulation results, Lu et al. [49] fabricated the periodic micro-patterned VO_2 thin film via mesh printing method, where the experimental results showed improved T_{lum} of 43.4% and ΔT_{sol} of 14.9%. However, the periodic porous VO_2 is rather difficult to fabricate. Therefore, Kang et al. [50, 51] adopted polymer assisted deposition to get VO_2 nanopores film with random pores (Fig. 5a). The optimized single-layered VO_2 film exhibited high integrated $T_{lum,l}$ of 43.3%, $T_{lum,h}$ of 39.9%) and ΔT_{sol} of 14.1% with a mean pore size of 28 nm. Cao et al. [52] utilized freeze drying in VO_2-film fabrication. Films with different porosities from 15% to 45% were obtained by varying the pre-freezing temperature and precursor concentration. The optimized T_{lum} was 50% and ΔT_{sol} was 14.7%.

Taylor et al. [53] developed a bioinspired method to solve the low T_{lum} and ΔT_{sol}. The structure contains a nanocone-shaped SiO_2 substrate and a thin layer of VO_2 on top of it as shown in Fig. 5b. Based on their simulation results, the ΔT_{sol} reached 23.1% whilst maintaining T_{lum} as 36.5%. The biomimetic structure is a RI gradient antireflection layer. Qian et al. [54] successfully fabricated a bioinspired VO_2 TCW (Fig. 5c). The experimental results showed the improvement to be very limited. The T_{lum} achieved was only 44.5% with ΔT_{sol} of 7.1%. However, the tapered arrays enhanced the contact angle with self-cleaning function.

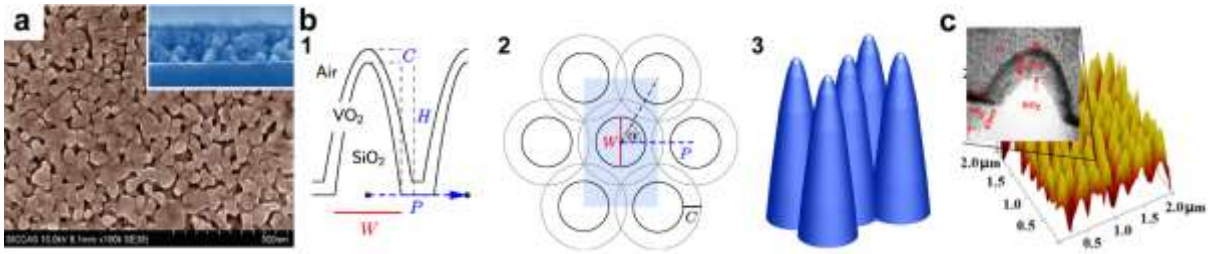

Fig. 5. a) Porous morphology of a 147-nm-thick VO_2 film, from the top and side view (inset) [50]. b) (1) Side and (2) top elevations of a nanotextured surface with hexagonally arranged circular paraboloid cones, and (3) the shapes of the cones [53]. c) AFM image of moth-eye antireflection layer, inset: TEM cross-section image to show the thickness of VO_2 coatings on SiO_2 [54].

Most researchers assume that solar radiation has normal incidence. However, most regions receive solar radiation from different angles in different seasons due to the rotation of the earth and its revolution around the sun. Therefore, Zhou et al. [55] designed a VO_2 TCW with 3D printed inclined columnar microstructures separated by void spaces. In winter, the solar radiation can transit through the gaps between two columns, leading to high T_{lum} and T_{sol}. While in summer, the solar radiation needs to pass through the columns, which leads to low T_{lum} and T_{sol}. In this way, the solar modulation ability is maximized.

3.1.4. Nanocomposites (Nanothermochromics)

In recent years, nano-thermochromism, which integrates VO_2 nanoparticles in a transparent matrix, has gained much more attention since it has been proved to increase T_{lum} and ΔT_{sol} simultaneously. In addition, the polymer film containing VO_2 nanoparticles is freestanding and is preferable for retrofitting existing windows. VO_2 nanoparticles can be prepared by various techniques but will not be discussed further here [56]. Li et al. [32, 57] used effective medium theory to calculate the effect of dilute suspensions of VO_2 nanoparticles, as well as VO_2 core

shell nanoparticles in a dielectric host. They discovered that VO_2 nanocomposites with VO_2 nanoparticles can significantly enhance T_{lum} jointly with much enhanced ΔT_{sol}, compared with VO_2-based continuous films. However, the particle size should be ~20 nm or less to prevent optical scattering. In addition, the nanospheres absorb rather than reflect. They also concluded that thin-walled hollow spherical VO_2 nanoshells can give significantly higher values of ΔT_{sol} than solid nanoparticles. The mechanism behind is that the RI of the internal nanofillers can be modulated, which can decrease the scattering caused by the RI mismatch between nanoparticles and their polymer matrix. However, VO_2 gradually oxidized into the toxic but thermodynamically stable oxide, V_2O_5, in wet ambient atmospheres (especially VO_2 nanoparticles due to their relatively small size and large specific surface area) [58], which leads to considerable deterioration of its thermochromic properties. Therefore, scientists put VO_2 as the core and covered it with a shell. Gao et al. [59] developed an all solution prepared silica-coated VO_2 (denoted as VO_2@SiO_2) core-shell structured nanoparticles polymer composite. A reactive silane coupler was used to enhance the dispersion of VO_2@SiO_2 particles in the PU matrix. The films are shown in Fig. 6a, 1 and the inset figure is the TEM image of VO_2@SiO_2 particles. After being integrated with a polymer into a VO_2@SiO_2/PU composite, the film had T_{lum} of 27.8% and ΔT_{sol} of 13.6% (Fig. 6a, 2). Coating VO_2 nanoparticles with a thin SiO_2 shell significantly improved their anti-oxidation and anti-acid abilities. In addition, the nanocomposite decreased the hysteresis width from 31 to 9.3°C, except for using SiO_2 as the shell. Chen et al. [60] designed a VO_2@ZnO nanoparticle-based thermochromic film, which showed robust durability (ΔT_{sol} remained at 77 % after 10^3 hours in a hyperthermal and humid environment) as demonstrated in Fig. 6b, high T_{lum} (48.8%) and high ΔT_{sol} (19.1%). However, these “shells” showed acceptable but limited protective effects on mitigating the deterioration of the VO_2 “core”. The infinite effect of current core-shell structures can be attributed to the following reason: in the phase transition process, VO_2 shows different lattice parameters

between the monoclinic and rutile phase, and a volume change occurs. This may affect the shell materials and weaken the protective function of VO_2 core-shell structures, resulting in limited enhanced stability.

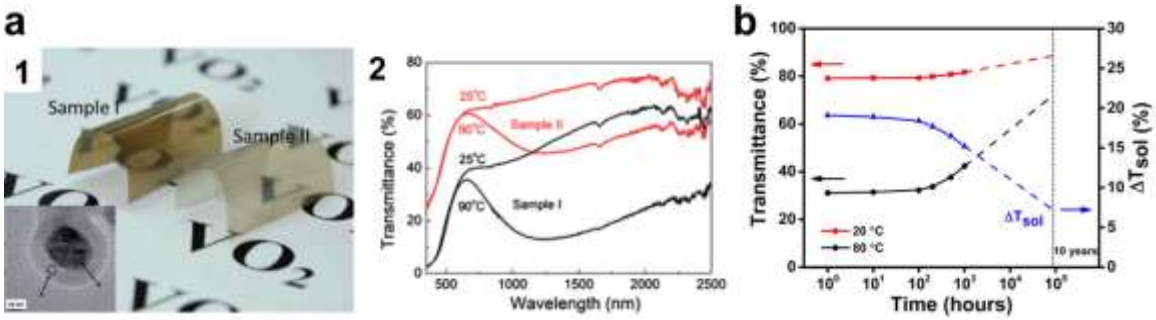

Fig. 6. a) (1) Photograph of VO_2@SiO_2/PU composite. The inset figure is TEM image of VO_2@SiO_2 particles, and (2) Transmittance spectra of VO_2@SiO_2/PU composite [59]. b) Longtime stability tests of VO_2@ZnO film [60].

Glass strongly absorbs for wavelength longer than 3 μm, and the emissivity is as large as 87% [61]. Thus, the regulation of room-temperature thermal radiation is also important for windows. Most recently, Wang et al. [62] designed a VO_2 TCW that not only can modulate the solar transmittance but also modulate the emissivity of long-wave infrared (2.5-25 μm) radiation (LWIR). This means that the window has a high front side thermal emissivity at high temperature to promote radiative cooling and a low front side thermal emissivity at low temperature to suppress radiative cooling. The window maintains a low thermal emissivity on the back side to minimize the heat exchange between the indoors and outdoors. The LWIR regulation is due to the W-doped VO_2 nanocomposite/poly (methyl-methacrylate)(PMMA) spacer/low-E structure, which forms a Fabry-Perot resonator. The authors also conducted energy consumption simulation of a tunable thermal emissivity TCW. The results show that the energy saving can be up to 324.6 MJ/m^2.

3.2. Hydrogel-based Smart Window

Hydrogel is a three-dimensional network of hydrophilic polymers (may contain moderately hydrophobic segments or a mixture of hydrophilic and hydrophobic groups) that can swell in water and hold large amount of water while maintaining the structure, due to chemical or physical cross-linking of individual polymer chains. Hydrogels usually undergo reversible volume phase transition or gel-sol phase transition in response to certain physical and chemical stimuli, such as temperature and pH. Back in the late 1990s, to address the deficiencies of VO_2 as an efficient TCW material, novel temperature-response materials such as hydrogel materials were explored [63]. For hydrogel, drastic transmittance change takes place in both visible and NIR ranges. Therefore, hydrogel has a relatively large ΔT_{sol}. The mechanism of hydrogel's thermochromism is that they undergo reversible hydrophilic/hydrophobic phase transition around the lower critical solution temperature (LCST). When the temperature is below the LCST, intermolecular hydrogen bonds dominate and could prevail between the polymer chains and surrounding water molecules. Incident light is allowed to pass through at low temperature. However, when the temperature goes above the LCST, the intramolecular hydrogen bonds between C=O and N-H groups inside the polymer chains are broken, resulting in phase separation and polymer aggregation. Therefore, incident light is strongly scattered by the difference in the refractive indices of the scattering centers of the aggregated polymer microparticles and free water domain. The extensively studied thermochromic hydrogels include poly(N-isopropylacrylamide) (PNIPAm) [64], polyampholyte hydrogel (PAH) [65], and hydroxypropyl cellulose (HPC) [66], N-vinylcaprolactam (PNVCL). The list is not complete, but serves to illustrate the current dynamics of the field of research. As PNIPAm is the most studied thermochromic hydrogel, this review will focus on introducing PNIPAm TCWs but also introduce some other hydrogel-based TCWs.

3.2.1. Poly(N-isopropylacrylaminde) (PNIPAm)

As one of the temperature-sensitive hydrogels, PNIPAm has been widely used in drug delivery research before its application in TCWs. Zhou et al. used a sandwich structure with PNIPAm hydrogel between two slices of glass substrates to construct a hydrogel TCW [64]. The PNIPAm-based TCWs showed different optical transmission spectra with different thicknesses (Fig. 7a, 1). The optical images of hydrogel with different thicknesses are shown in Fig. 7a, 2. After optimization, $T_{lum,l}$ of 87.9%, $T_{lum,h}$ of 59.9%, ΔT_{sol} of 20.4%, and LCST of 32°C were achieved. Since PNIPAm has high transmittance in the NIR range in both cold and hot states, which is unfavorable for cooling in summer, two approaches have been investigated to overcome this problem. The first approach is to extend the wavelength region where thermochromism occurs to the NIR region. The second one is to combine with NIR-shielding materials. For the first approach, Li et al. [67] reported a hydrogel TCW based on the tunable scattering behaviors of temperature-responsive poly(N-isopropylacrylamide)-2-aminoethylmethacrylate hydrochloride (PNIPAm-AEMA) hydrogel microparticles. The mechanism and transmittance spectrum are shown in Fig. 7b, 1, and 2, respectively. The average size of PNIPAm-AEMA microparticles changed from 1,388 nm to 546 nm when the temperature increased from 25°C to 35°C, yielding excellent ΔT_{IR} (modulation ability in IR-region) of 75.6% and high $T_{lum,l}$ of 87.2% (Fig. 7b, 3). Another strategy in the first approach is to combine NIR-thermochromic materials to enlarge the thermochromic wavelength range. Zhou et al. [68] integrated VO_2 nanoparticles inside PNIPAm hydrogel with $T_{lum,l}$ of 82.1 %, $T_{lum,h}$ of 43.2 % and ΔT_{sol} of 34.7 %.

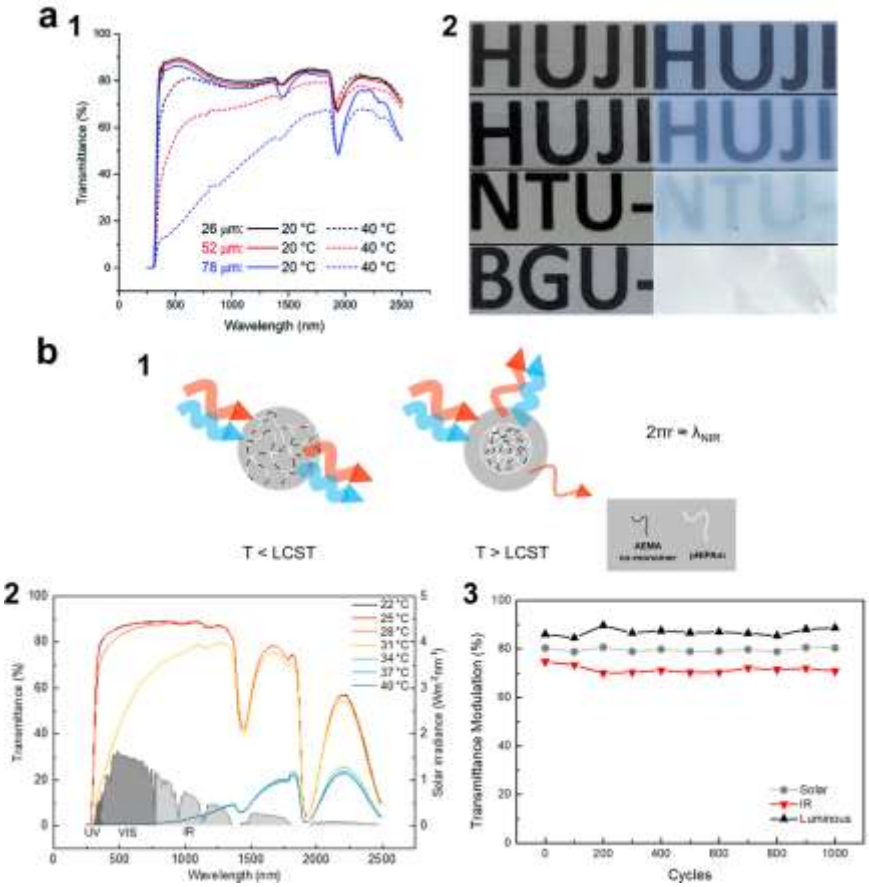

Fig. 7. a) (1) Optical transmittance spectra of the three samples with different thicknesses between 20°C and 40°C, and (2) smart hydrogel thin films at room temperature (left) and in sunshine at 35°C (right) with different thickness [64]. b) (1) Light manipulating with the aid of the phase transition PNIPAm-AEMA co-polymerized microparticles. Visible light and IR light are represented by blue and red arrows, respectively, (2) transmittance spectra of PNIPAm-AEMA hydrogel with a layer thickness of 240 μm at different temperatures, and (3) spectra of Cs_xWO_3/PAM-PNIPAm window, Cs_xWO_3 film, PAM-PNIPAm window, and single-layer glass window [67].

The second approach is to combine the PNIPAm with some NIR-shielding materials. The majority of NIR-shielding materials are photothermal materials, which allow hydrogels to respond to solar radiation through an absorption-induced heating effect. Lee et al. [69] dispersed antimony-tin oxide (ATO) in PNIPAm. The NIR-absorbing ATO acts as a nanoheater

to induce optical switching of the hydrogel and at the same time, ATO absorbs NIR-radiation (localized surface plasmon resonance (LSPR) due to n-doping) for excellent NIR-shielding. The optimum results for ATP/PNIPAm were T_{lum} of 78.2%, $T_{lum,h}$ of 62.7%, $\Delta T_{380\text{-}780}$ of 35.7%, and $\Delta T_{780\text{-}2500}$ of 18.1%. Similarly, Wu et al. [70] designed a window with high NIR-shielding and controllable visible light transmittance. As depicted in Fig. 8, 96.2% of NIR from 800 to 2500 nm was shielded and large portion of visible light was permitted for indoor lighting (T_{lum} of 78.2% and 45.3% before and after the LCST). The window was constructed by a photothermal cesium tungsten bronze (Cs_xWO_3) film and thermoresponsive PAM-PNIPAm hydrogel. The indoor temperature with the smart window was ~21°C lower than that with a regular single-layered glass window under one sun irradiation.

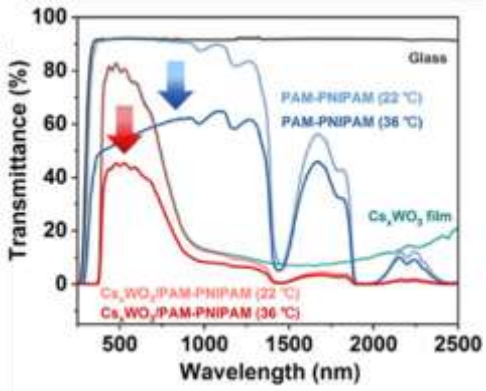

Fig. 8. Optical photos for 1 m^2 large-scale window testing at a different time of a day. The TRL is half-filled in the window (0.5 m × 1 m) [70].

Recently, Zhou et al. [71] developed a high thermal energy storage hydrogel TCW (Fig. 9a). The window had T_{lum} of 90% and ΔT_{sol} of 42.5% with high specific heat capacity of 4.35 kJ/kg·K. The excellent thermal performance was proved by actual outdoor demonstration (temperature reduction of 34°C during daytime and comparable temperature during nighttime, as shown in Fig. 9b). The energy-saving potential of using the hydrogel was compared with low-E glass numerically. It was found that using the hydrogel can cut off 44.6% of annual

HVAC energy consumption, as shown in Fig. 9c. The difference between their PNIPAm TCW and the others was that the former was synthesized by dispersing PNIPAm particles into water and forming a homogeneous solution. This method endows the hydrogel with free-flowing property. Lin et al. [16] proposed an ultra-boardband hydrogel TCW which has a PNIPAm-silver-nanowires composite structure. In winter, the window has high solar transmittance for solar heating and low thermal emittance for heat insulation. While in summer, the window has low solar transmittance and high thermal emittance for heat dissipation. The high luminous transmittance (78.3%) and low transition temperature (31°C) make it feasible for real applications. The thermal regulation in mid-infrared region is archived through water molecules within the PNIPAm network, which are pumped out due to the thermally induced hydrophobic-hydrophilic transition of PNIPAm. As water can strongly emit IR-radiation, the window can be switched from thermal reflective to emissive. The energy simulations revealed that the window is suitable for various climates and can save energy both in winters and summers.

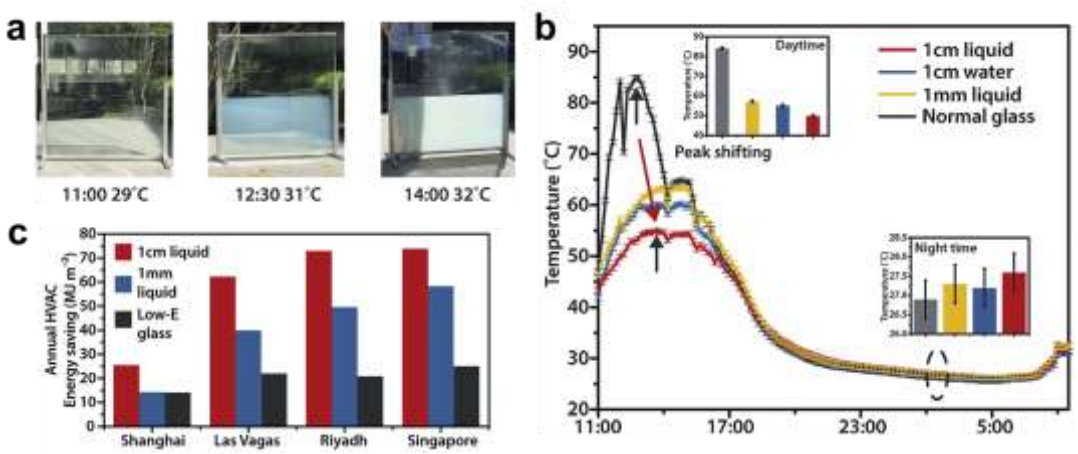

Fig. 9. a) 24 h air temperature curve for the outdoor demonstration in Singapore. The inserts are the daytime (12:00) and night (3:00) temperature reading for normal glass, 1-mm liquid, 1-cm water, and 1-cm liquid, respectively; b) 24 h temperature curve for the outdoor demonstration in Singapore; c) annual HVAC energy-saving performance [71].

3.2.2. Hydroxypropyl cellulose (HPC)

LCST of PNIPAm can be manipulated by adding various salts, such as sodium chloride (NaCl) [72]. However, the fabrication process of PNIPAm is complicated and it is difficult to remove odor and control gelation time. Hydroxypropyl cellulose (HPC) is easier to synthesize than PNIPAm. To allow hydrogel-based TCWs to work properly in cold locations and not freeze in winter, Nakamura et al. [73] adjusted the freezing temperature by adding glycerol, an anti-freezing agent. The glycerol promoted the release of water from the HPC fibers even at low temperatures because of the strong hydrogen bonding between glycerol and water. The glycerol prevented the mixture of gel from freezing at -10°C for 180 min. The LCST of HPC hydrogel-based TCW can also be easily controlled by adding NaCl. Upon increasing the concentration of NaCl from 0.5 to 5 wt%, the LCST reduced from 42 to 30°C [74]. Yang et al. [75] put VO_2 into a thermal sensitive microgel synthesized from HPC and acrylic acid, and obtained high ΔT_{sol} of 36% and high $T_{lum,l}$ of 80% and $T_{lum,h}$ of 33%.

However, some challenges are faced with hydrogel thermochromic materials. Rigorous encapsulation is required because of the nature of liquid phase. During their utilization, leakage of thermoresponse material could occur followed by dramatic decrease in performance [23]. Other challenges are the structural damage during transitions and evaporation. When the temperature is above T_c, the polymer chains embedded into the thermochromic hydrogel begin shrinking and collapsing, because of the disruption of hydrogen bonds between the polymer chains and surrounding water molecules, damaging the structure and reducing the reproducibility and durability.

3.3. Perovskite-based Smart Window

The perovskite is usually written using the general formula, ABX_3 (as shown in Fig. 10a), in

which anion X is bonded to a larger cation A (positioned at the corner) and a smaller cation B located at the center of the unit cell. There has been tremendous scientific interest in the development and application of perovskites, especially for photovoltaics, lasers, and LED devices. Researchers have made much effort to integrate perovskite solar cells (PSCs) into windows as it opens the prospect of employing PSCs to the entire façade of buildings for solar power generation, rather than limiting them on roof [76]. The effect is even more significant in modern buildings where WWR dramatically increases. Unlike conventional solar cells, where power conversion efficiency (PCE) is the most important index, color properties, T_{lum}, and PCE are all critical criteria for PSCs [77]. In the early stage, transparent and semitransparent PSCs attracted much attention [76, 78]. However, there is tradeoff between PCE and high T_{lum} in these windows. In recent years, new methods have been proposed to solve this tradeoff, and these methods simultaneously enable the combination of two state-of-the-art techniques: TCW and photovoltaics.

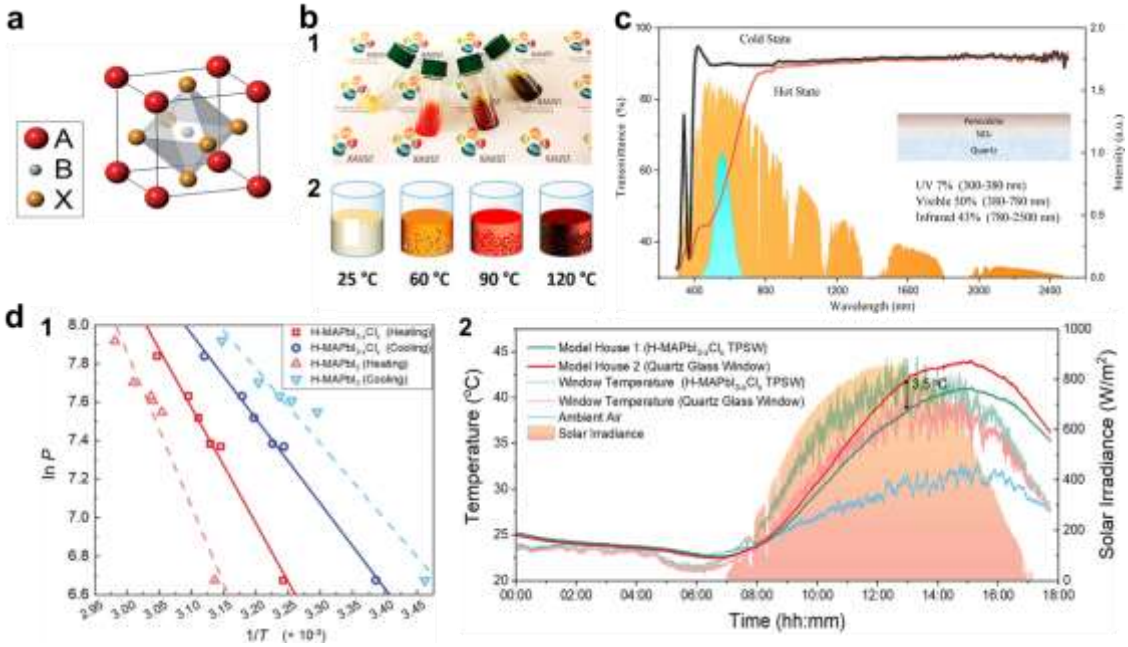

Fig. 10. a) The ABX_3 perovskite crystal structure. b) (1) Photograph and (2) schematic representation of the perovskite at inks 25, 60, 90, 120°C [79]. c) The transmittance spectra

of a water vapor hydrated/dehydrated perovskite TCW at cold and hot states [80]. d) (1) The fitted curve in the Clausius-Clapeyron diagram for hydration/dehydration process of perovskite TCW, and (2) 18 h temperature curve for the model house field test [81].

At present, thermochromic perovskite materials can be divided into two categories. One is based on thermochromic perovskite inks and the other is based on thermochromic perovskite thin film. For thermochromic perovskite inks, Bastiani et al. [79] utilized a unique crystallization process of bi-constituent perovskite solution and designed liquid-phase TCW, which exhibits complete reversible chromatic variation, ranging from yellow to black as the temperature increases from 25°C to 120°C (Fig. 10b, 1 and 2). The underlying mechanism is different precipitation rates or crystallization temperatures of black iodine-based perovskite and orange bromide-based perovskite. For thermochromic perovskite thin films, Halder et al. [82] explored the thermochromic behavior of hydrated lead halide hybrid perovskites, $CH_3NH_3PbI_3$, and attributed the thermochromism of perovskite to the reversible hydration/dehydration process of $CH_3NH_3PbI_3$ when it encounters moisture.

$$CH_3NH_3PbI_3 + 3\,CH_3NH_3I \overset{H_2O}{\longleftrightarrow} (CH_3NH_3)_4PbI_6 \cdot 2H_2O \quad [82]. \tag{4}$$

Equation (4) has been derived based on XRD results of thin film materials before and after the hydration/dehydration process. In the cold state, the hydrated perovskite, $(CH_3NH_3)_4PbI_6{\cdot}2H_2O$ is in the non-perovskite phase and can be considered as zero-dimensional network of isolated $[PbI_6]^{4-}$ octahedral, neutralized by surrounding $CH_3NH_3^+$ cations. On the other hand, in the hot state, it becomes normal $CH_3NH_3PbI_3$, which is held together by ionic interactions between organic and inorganic portion, as well as hydrogen-bonding interactions between hydrogens on the NH_3^+ head and the iodide atoms. Zhang et al.

[80] utilized this kind of perovskite material and developed a perovskite TCW towards achieving high ΔT_{sol}, whilst maintaining high T_{lum} and low T_c. The thermochromic region of the perovskite TCW is mainly in the visible light region (Fig. 10c). The T_c was found to depend on relative humidity of the environment. There is a characteristic strong excitonic peaks at about 370 nm of the hydrated phase, which is due to absorption of the isolated $[PbI_6]^{4-}$ octahedral [83]. Zhang et al. [84] simulated the energy consumption of an office building with their proposed perovskite TCW. The implementation of the perovskite TCW had more pronounced effect in cities where cooling demand dominates and could reduce the total energy consumption by almost 10% in Hong Kong, Singapore and Cairo. Most recently, Liu et al. [81] developed a hydrated $MAPbI_{3-x}Cl_x$ TCW, which has tunable low T_c of 29.4-51.4°C, controllable and narrow hysteresis width (7.7-13.2°C). They developed a Clausius-Clapeyron model to predict the T_c of their perovskite TCWs at different humidity conditions (Fig. 10d, 1). A field test demonstrated that the $MAPbI_{3-x}Cl_x$ TCW reduced indoor air temperature by 3.5°C (Fig. 10d, 2).

Some of the PTWs combine two state-of-the-art technologies: smart window and solar cell into one window, aiming to achieve two targets of energy saving and energy generation in the same device, which is an attractive and important topic to be explored. Wheeler et al. investigated reversible switches of $MAPbI_3$ film by exposing it with methylamine vapor (CH_3NH_2). The formed complex is a metal halide perovskite-methylamine complex ($MAPbI_3 \cdot CH_3NH_2$) [85]. This complex can reversibly transition between transparent state (T_{lum} of 68%) and the colored state (T_{lum} of less than 3%) at a transition temperature above 60°C. The transmittance spectrum and efficiency are shown in Fig. 11a, 1 and 2, respectively. Later, Rosales et al. [83] found that $MAPbI_3$ can also react with methanol and form a bleached $MA_6PbI_8 \cdot 2MeOH$. The weaker bonding of methanol with $MAPbI_3$ compared to water vapor effectively reduces the complex transition temperature to 50°C. Lin et al. [86] developed a smart photovoltaic window using

$CsPbI_{3-x}Br_x$ perovskite material (Fig. 11b, 1). The photovoltaic window could change from the transparent cold state with T_{lum} of 81.7% to the colored hot state with T_{lum} of 35.4% (optical image of the window is shown in Fig. 11b, 2). Device efficiency above 7% has been achieved in these thermochromic photovoltaic windows in the hot state. However, their thermochromic solar cells showed high T_c (100-350°C) and long transition time (up to 25 hours). No matter water vapor, methylamine, or methanol, they all intercalate in $MAPbI_3$ by hydrogen bond. The H-bonds are strong enough to form stable colorless complexes at room temperature but weak enough to dissociate upon heating. This is the reason why thermochromism of perovskite could happen.

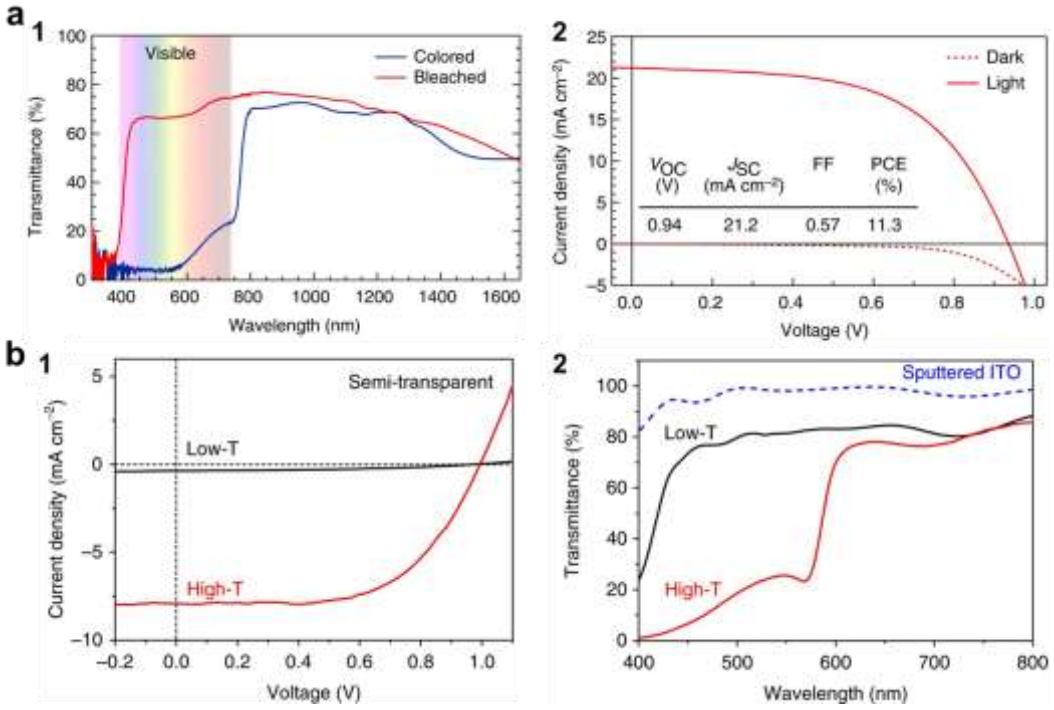

Fig. 11. a) (1) Transmittance spectra of perovskite TCW in the bleached ($MAPbI_3 \cdot CH_3NH_2$) and colored ($MAPbI_3$) states, and (2) J-V curves of the perovskite TCW solar cell in the dark (dashed) and under illumination (solid) [85]. The inset table shows photovoltaic performance metrics of the device before being bleached. b) (1) J-V curves of the perovskite TCW solar cell made of $CsPbI_{3-x}Br_x$, and (2) The transmittance spectra of the perovskite TCW solar cell

made of $CsPbI_{3-x}Br_x$ in low temperature and high temperature phases [86].

3.4. Ionic Liquid-based Smart Window

Ionic liquid (IL) is a vast group of salts with melting temperature below 100°C. By introducing thermochromic transition metal complexes into IL, a stable thermochromic IL can be prepared. The thermochromic property is based on an octahedral-tetrahedral configuration change of transition metal complexes assisted by interaction with donor solvent molecules. IL can change color from colorless to blue upon temperature changes, as shown in Fig. 12a [87]. However, the solar modulation is only limited to the visible range (656-705 nm) and ΔT_{sol} is not high (~8-11%). Zhu et al. [88] and Chen et al. [89] dispersed VO_2 nanoparticles in two different thermochromic IL: nickel-chlorine-ionic liquid (Ni-Cl-IL) and nickel-bromide-ionic liquid (Ni-Br-IL), respectively, to enhance the solar modulation ability. The results showed that for VO_2/Ni-Cl-IL, ΔT_{sol} reached 26.45% while maintaining high T_{lum} ($T_{lum,l}$ of 66.44%, $T_{lum,h}$ of 43.93%). For VO_2/Ni-Br-IL, ΔT_{sol} was 27.0% while $T_{lum,l}$ was 65.9% and $T_{lum,h}$ was 55.3%. Lee et al. [90] designed another IL-based TCW named polyurethane (PU) ionogel TCW (Fig. 12b). Ionogel, as the name implies, is “gel containing ionic liquid”. It is a composite material with a three-dimensional network percolating throughout IL and can retain IL’s vital properties. What distinctly differentiates ionogel from hydrogel is its stability even at high temperatures (250°C) due to the intrinsic thermal stability of IL. The advantages also include no volume change upon heating, absent of freezing point and volatility. The ionogel is highly transparent at room temperature since complete phase mixing. When the temperature is higher than T_c (about 33°C), the subtle interaction balance between IL and PU network breaks due to molecular repulsion and IL-rich domains forms which causes light scatting and reduce transmittance. The T_c can be tuned from subzero to over 100°C by introducing a second IL into the system. Fig. 12b, 2 shows the transmittance of PU-based ionogel at different temperatures. The high

durability (stable for more than 5000 heating-cooling cycles) of constant optical properties of this TCW is shown in Fig. 12b, 3. Above all, IL-TCWs have many advantages in terms of optical performance and stability, however, the high cost of raw materials needs to be solved before real application.

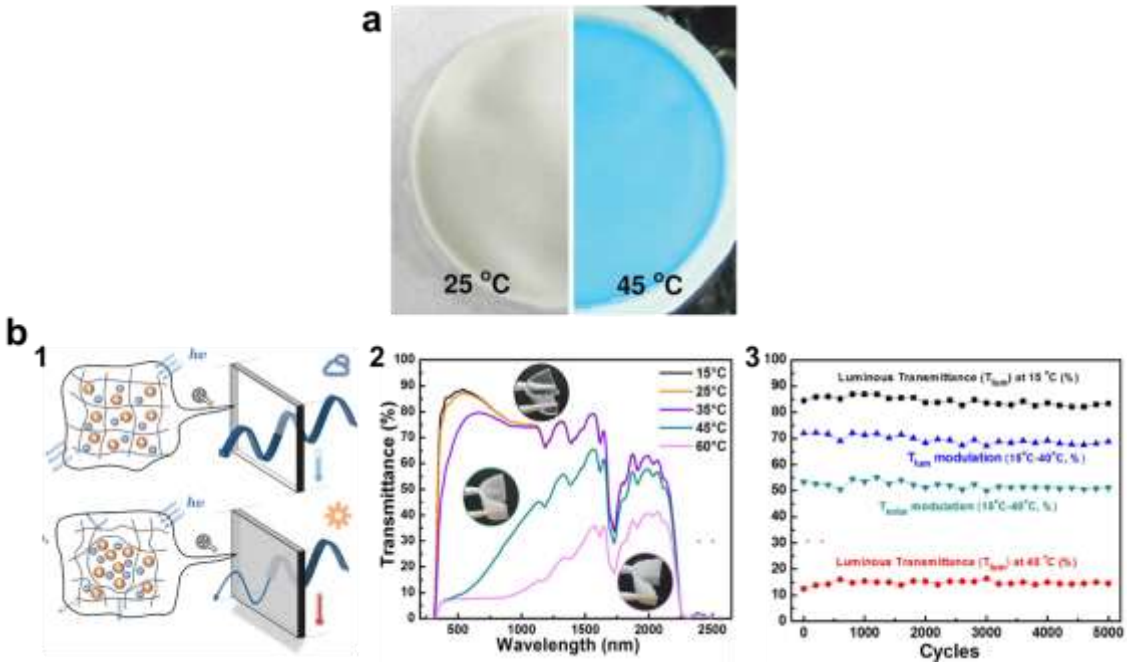

Fig. 12. a) Color of translucent composite films of poly(vinylidene fluoride), ionic liquid and nickel complexes changes upon temperature variation [87]. b) (1) Design concept illustrating thermochromic ionogel optical transmittance change in response to temperature, (2) the transmittance spectra of ionogel at various temperatures, and insets show the transparent, translucent, and opaque states of the flexible ionogel, and (3) the optical performance reversibility of ionogel during 5000 cycles [90].

3.5. Liquid crystal-based Smart Window

A new system of liquid crystal (LC)/polymer composite may offer new opportunities for making thermochromic materials in response to temperature [91, 92]. One typical type is based on reversibly crystal orientation transition between the smectic (SmA, long-molecular-axis

structure) and chiral nematic (N*, helix-molecular-structure) phases (the transition is called SmA-N* phase transition). As shown in Fig. 13a, for the low temperature state, the SmA phase is homeotropically oriented and stabilized by the porous polymer matrix. The whole device is transparent because the RI of long-molecular-axis of the SmA and the polymer matrix are perfectly consistent. After the temperature surpasses the T_c, the spontaneously twisted helix-molecular-structure of the N* phase will result in a spatially varied RI and scatter visible light. The T_c can be adjusted according to different concentrations of SmA in LC. Liang et al. developed a multi-responsive smart film containing tungsten bronze (Cs_xWO_3) nanorods and LC/polymer composite [92]. The window can change its T_{lum} between 67% and 1.5% by temperature, electric fields and NIR-light, and it can block 95% of NIR (800-2500 nm). The SEM figure and photograph of this kind of TCW are shown in Fig. 13b, 1 and b, 2, respectively.

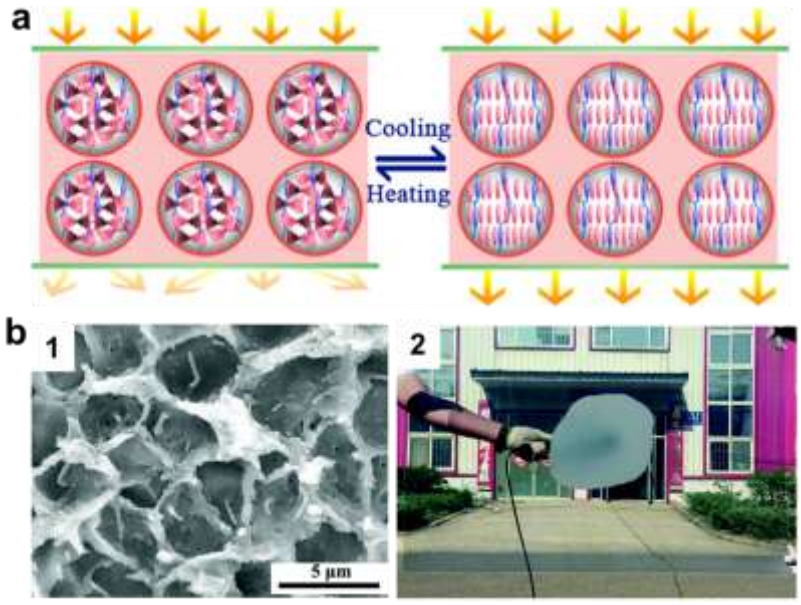

Fig. 13. a) Schematic of the smectic A (SmA) to chiral nematic (N*) phase transition [93]. b) (1) Enlarged SEM image of the morphology of the polymer structure observed from a top view, and (2) the large-scale manufacturing of the film [92].

3.6. Comparison of Reviewed Thermochromic Smart Windows

Fig. 14 depicts the two crucial criteria of reviewed TCWs, i.e., (1) luminous transmittances in cold (clear) and hot (tinted) states, $T_{lum,l}$ and $T_{lum,h}$, respectively, against (2) solar modulation ability, ΔT_{sol}. Among various types of TCWs reported, hydrogel-based TCW has wider range of ΔT_{sol}, compared to other TCWs, from approximately 5% to 80%, resulting in $T_{lum,l}$ as high as 90% and $T_{lum,h}$ as low as 0%. Yet, becoming opaque in the hot state is a concern if outdoor view is needed. Apart from hydrogel-based TCWs, perovskite-based TCWs also have high $T_{lum,l}$ of above 75%, albeit with a much lower ΔT_{sol} of around 25%. Overall, VO_2-based TCWs have a narrow range of ΔT_{sol} and T_{lum} in both states, which is about 20% or below, suggesting poor visual access to the outdoor. In addition, the T_{lum} of VO_2 does not depend strongly on temperature. For all the different techniques to improve T_{lum} and ΔT_{sol} of VO_2 TCWs, the improvements are relatively small. Therefore, we can say that T_{lum} is about 50% and ΔT_{sol} is about 10% for VO_2 TCWs. The tungsten doping is still the most effective and common method to reduce the transition temperature. TCW may come in two different categories: (1) heat-reflecting TCW, which includes hydrogel, and liquid crystal TCWs, and (2) heat-absorbing TCWs, which includes vanadium dioxide, perovskite, and ionic crystal TCWs. In the hot state, the reflectivity of heat-reflecting TCW increases, while the absorptivity of heat-absorbing TCWs increases. Both categories experience decreases in transmittance. Heat-reflecting TCWs seem to be more advantageous for energy-saving purpose since they bounce back most of the solar irradiation (by light scattering) from entering the building during the hot state. However, when reaching T_c, the windows become opaque and thus residents cannot appreciate the outdoor view anymore. In addition, psychological well-being and health benefits associated with visual contact with the ambience are gaining more attention. In contrast, heat-absorbing TCWs stand out for applications where a permanent view from inside is needed. Most of the techniques mentioned in Section 3 are suitable for fabricating new windows. However, the

nanocomposite VO_2 TCW can be made into a flexible foil and used for upgrading existing windows. Table 2 summarizes the optical properties of the reviewed TCWs, along with details such as the fabrication method and T_c of the window.

For TCWs, the materials used are VO_2, hydrogel, perovskite, and ionic liquid. The raw chemicals to fabricate these materials are all expensive. As for the fabrication cost, most of them are cheap since they are solution-based fabrication methods. However, VO_2 thin film or nanoparticle needs to be fabricated by high-temperature treatment. Especially for VO_2 thin film, the annealing temperatures are up to 600°C. Therefore, to let customers choose TCWs, decreasing the cost is a major challenge and should be properly addressed in the following studies.

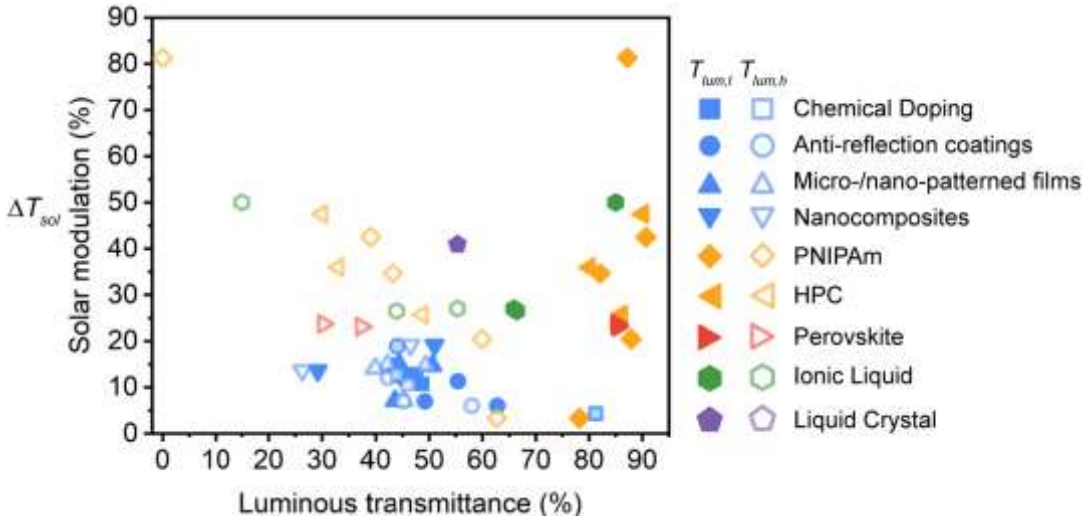

Fig. 14. Illustration of luminous transmittances in the cold (clear) state, $T_{lum,l}$, and the hot (tinted) state, $T_{lum,h}$, against solar modulation ability, ΔT_{sol} of respective thermochromic smart window reported in this review. The values are provided from the literature. Symbols in blue, orange, red, green and grey represent VO_2-based, hydrogel-based, perovskite-based, ionic liquid-based, and liquid crystal-based TCWs, respectively.

Table 2. Optical indices and thermal analysis of reviewed thermochromic smart window (TCW).

Materials	Techniques	Fabrication Method	T_{lum}[a] (%)		ΔT_{sol}[d] (%)	Waveband[e] (nm)	Details	Ref
			$T_{lum,l}$[b]	$T_{lum,h}$[c]				
Vanadium dioxide (VO_2)-based	Chemical doping	Tungsten doping	-		-	NIR	lower the T_c[f] by ~23 K/at.% W	[34]
		Fluorine doping	48.7	45.9	10.7	NIR	T_c is 35°C at 2.93 at.% F	[94]
		Magnesium doping	47.5	44	12.8	NIR	lower the T_c by ~3 K/at.% Mg	[41, 42]
		Tungsten & magnesium co-doped	81.3		4.3	NIR	T_c is 35°C at 2 at.% W and 4 at.% Mg	[43]
	Antireflective layer	TiO_2/VO_2	49.2	45.1	6.99	NIR	-	[44]
		$TiO_2/VO_2/TiO_2$	62.8	58	6	NIR	-	[29]
		$TiO_2/VO_2/TiO_2/VO_2/TiO_2$	45	42.3	12.1	NIR	-	[29]
		ZrO_2/VO_2	55	50.5	-	NIR	-	[46]
		Index tunable ARC/ VO_2	46.3	41.4	18.9	NIR	-	[95]
		TiO_2 nanocones/VO_2	55.4		11.3		-	
	Micro-/nano-patterned	Nano-gridded	79.2	74.2	14.0	NIR	Simulation	[48]
			44.4	42.2	14.9	NIR	Experiment; screen printing method	[49]
		Porous VO_2	43.3	39.9	14.1	NIR	Experiment; polymer-assisted deposition	[50, 51]
			50.6	49.4	14.7	NIR	Experiment; freeze dried	[52]
		Moth-eye structure	39.4	33.6	23.1	NIR	Simulation	[53]
			43.6	45.3	7.1	NIR	Experiment; self-cleaning	[54]
	Nanocomposites	VO_2@SiO_2 core shell	29.2	26.3	13.6	NIR	Anti-oxidation; anti-acid	[59]
		VO_2@ZnO core shell	51.0	46.5	19.1	NIR	High durability up to 1000 hours	[60]
Hydrogel	PNIPAm	PNIPAm	87.9	59.9	20.4	Mainly 300-1900	LCST[g] of 32°C	[64]
		PNIPAm-AEMA	87.2	0	81.3	300-2500	T_c is 31°C; visible/NIR simultaneous tuning	[67]
		PNIPAm/VO_2	82.1	43.2	34.7	300-2500	T_c is 30°C	[68]
		PNIPAm/ATO	78.2	62.7	3.3	300-2500	Dual responsive	[69]
		PNIPAm particles in water	90.7	39.1	42.5	300-2500, depends on thickness	High thermal energy storage capability	[71]
	HPC (solubility	HPC/NaCl	86.1	48.7	25.7	Mainly	LCST reduced from 42 to 30°C	[66]

	change of the polymer in water)					300-1500 until 44°C		
		HPC/glycerol	-		-	300-1500	Freezing resistance	[73]
		HPC/VO_2	80	33	36	300-2500	T_c is 50°C	[75]
		HPC/PAA	90	30	47.5	300-2500	T_c is 26.5°C	[96]
Perovskite	Hydration and dehydration	$MAPbI_3$	85.4	37.4	23.1	300-800	Transition properties are related to humidity	[80]
	reversible process	$MAPbI_{3-x}Cl_x$	85.2	30.3	23.7	300-800	Lower transition width	[81]
		$CsPbI_{3-x}Br_x$	81.7	35.4	-	300-800	Thermochromic windows combined with solar cells	[86]
Ionic Liquid	Light scattering at interfaces of IL and PU domains	PU-based ionogels	87	17	50	300-2200	LCST can be from subzero to over 100; stable more than 5000 cycles	[90]
	$[NiCl_{6-x}(C_2OHminBF$	Ni-Cl-IL	90.6	81.1	8.38	656-705	Colorless to blue	[88]
	and $[NiCl_4]^{2-}$ reversible change	VO_2/Ni-Cl-IL	66.4	43.9	26.4	300-2500	Brown to green	[88]
	$[NiBr_{6-x}(C_2OHminBF$	Ni-Br-IL	92.2	87.1	11.5	300-780	Colorless to blue	[89]
	and $[NiBr_4]^{2-}$ reversible change	VO_2/Ni-Br-IL	65.9	55.3	27	300-2500	Brown to green	[89]
Liquid crystal	A smectic A (SmA) to chiral nematic (N*) phase transition	VO_2/LC	55.3		40.9	-	Temperature/voltage dual responses	[91]
		Cs_xWO_3-LC-polymer composite	67	1.5	-	-	Roll-to-roll fabrication; 95% of NIR irradiation can be screen out	[92]

[a), b), c)] T_{lum} is the average of luminous transmittances in the cold (clear) state, $T_{lum,l}$, and the hot (tinted) states, $T_{lum.,h}$; [d)] ΔT_{sol} is the solar modulation ability of TCW; [e)] Waveband of NIR is approximately between 780 nm to 2500 nm; [f)] T_c represents the transition temperature of TCW; [g)] LCST is the lower critical solution temperature of hydrogel.

4. Roof: Daytime Passive Radiative Cooler

Water vapor, gaseous atmospheric constituents and aerosols in the terrestrial atmosphere absorb and backscatter thermal radiation from the earth surface. However, the atmosphere has a transparent window in the 8-13 μm waveband which coincides with the peak thermal radiation emitted by a blackbody at ambient temperature (300 K, terrestrial heat sources). This allows objects to eliminate heat through thermal radiation to outer space which acts as a heat sink. When the outgoing emitted radiation exceeds the heat absorbed from solar irradiance and atmospheric thermal radiation, a passive cooling effect is produced. This phenomenon is called radiative cooling and is an integral part of the Earth's heat balance mechanism. Instead of rejecting waste heat to the surroundings like conventional cooling technologies (vapor compression-based cooling), radiative cooling sends excessive heat to the outer space and achieves cooling without additional energy consumption.

The use of radiative cooling for refrigeration dates back to the first dynasty of Egyptian civilization, when clay trays with water were placed on beds of wood shavings and/or straw on clear nights to make ice, and in ancient Persia where yakhchāl (ice pits) were used to harvest and store ice [97]. The earliest scientific reference to passive radiative cooling by Arago F. [98] in 1826 discussed its potential for indoor climatization with temperature drops up to 6-8°C reported under a clear and calm night sky. However, since the peak demand for cooling occurs during the day, the focus has shifted from nocturnal radiative cooling to daytime radiative cooling, which combines the properties of both broadband solar reflectors and selective emitters. For this reason, daytime radiative cooling will be emphasized in this section. The net cooling power, P_{net} produced by such a cooler with surface temperature, T, is defined by,

$$P_{net}(T) = P_{rad}(T) - P_{atm}(T_a) - P_{sun} - P_{cond} - P_{conv} . \quad (5)$$

Where P_{rad} is the radiative flux emitted by the daytime passive radiative cooler (DPRC), P_{atm} is the atmospheric radiation at ambient air temperature, T_a, absorbed by the cooler, P_{sun} is the solar radiation absorbed; and P_{cond} and P_{conv} are the conductive and convective heat gains (nonradiative heat transfer) respectively. It is important to note that the radiative heat exchange in Equation (5) is only between the radiative cooling surface, the atmosphere, and the sun; and neglects the influence of the surrounding buildings, trees, and the ground. This is only valid if the cooler surface is horizontal or placed with a small tilt angle. If the coolers are mounted on vertical walls, the net cooling power will be reduced due to the heat transfer with the surroundings. P_{rad}, P_{atm}, P_{sun}, P_{cond}, and P_{conv} can be calculated as shown below [99]:

$$P_{rad}(T) = A \int \mathrm{d}\Omega \cos\theta \int_0^\infty \mathrm{d}\lambda I_{BB}(T,\lambda)\varepsilon(\lambda,\theta) , \quad (6)$$

$$P_{atm}(T_a) = A \int \mathrm{d}\Omega \cos\theta \int_0^\infty \mathrm{d}\lambda I_{BB}(T_a,\lambda)\varepsilon(\lambda,\theta)\varepsilon_{atm}(\lambda,\theta) , \quad (7)$$

$$P_{Sun} = A \int d\lambda \varepsilon(\lambda,\theta_{Sun})\, I_{AM1.5}(\lambda) , \quad (8)$$

$$P_{cond} + P_{conv} = hA(T - T_a) . \quad (9)$$

Where A is the surface area of DPRC, $\varepsilon(\lambda, \theta)$ is the spectral and directional emissivity of the cooler, $\int d\Omega$ is the angular integral over a hemisphere ($2\pi \int_0^{\frac{\pi}{2}} d\theta \sin\theta$), θ is the zenith angle, I_{BB} is the blackbody spectral intensity, ε_{atm} is the atmosphere's spectral emissivity, $I(\lambda)$ is the solar irradiance distribution, h is a heat transfer coefficient that accounts for non-radiative heat gain arising from the DPRC's contact with air and adjacent surfaces. If the directional effect on the cooler's emissivity is disregarded by assuming that the DPRC faces the sun, the spectral emissivity at the zenith, θ_{Sun} can be used.

The ideal DPRC must be perfectly opaque in the transparent window (8-13 μm) and reflect all

other wavelengths. Rephaeli et al. [100] found that quasi-total (more than 90%) solar reflectivity was vital if meaningful cooling power was to be achieved. The cooling device also performs better in environments with low relative humidity (RH): the presence of precipitable water (PW), which is the main source of infrared absorption in the atmosphere increases its emissivity and consequently P_{atm}. Some devices also utilize the secondary atmospheric window (AW) between 16-23 μm; however, it is much weaker and its transparency deteriorates rapidly with high PW.

4.1. Daytime Radiative Cooling Materials

For daytime radiative cooling, achieving high solar reflectance (R_{sol}) simultaneously with high emissivity over the AW is a challenge. In 2014, Raman et al. [99] first demonstrated daytime radiative cooling below the ambient temperature using a photonic radiative cooler. Since then, various DPRCs have been invented. These materials will be discussed in the following sections.

4.1.1. Bulk and Gaseous Material

DPRCs typically consist of a thermally emissive layer on a solar reflective substrate. DPRCs that use spectrally selective polymers (for the emissive layer) have a significant advantage over other radiative coolers in terms of manufacturability and cost. Polydimethylsiloxane (PDMS) and polytetrafluoroethylene (PTFE) plastic surfaces have high infrared emissivity in the AW and therefore have been considered for DPRCs. Kou et al. [101] presented a PDMS-based thin film cooling device (Fig. 15a), which achieved a temperature differential of 8.2°C at noon under direct sunlight in Pasadena, California. Lin et al. [102] developed a scalable PDMS-based radiative cooler that achieved sub-ambient cooling in Hong Kong's hot and humid climate. An average temperature drop of 2.4°C was demonstrated without wind/sun shields. Although PDMS is cheap, available abundantly and can be easily deposited on substrates, it

experiences thermal degradation when exposed to direct sunlight. Yang et al. [103] reported a dual layer structure of sintered PTFE on a silver film that achieved a record-high R_{sol} of 0.99, and a mid-IR thermal emittance of 0.9. The reflection and scattering mechanisms responsible for its selective emissivity are illustrated in Fig. 15b.

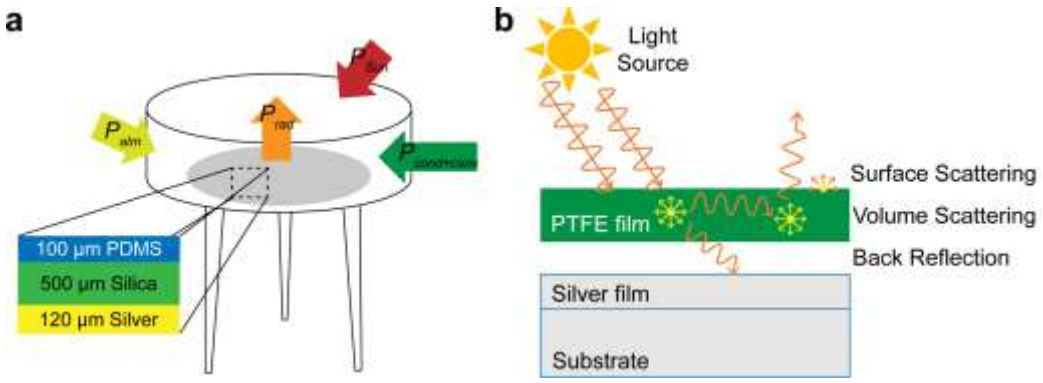

Fig. 15. a) Structure of PDMS on silver mirror PRC with energy input/output terms labelled. b) Depiction of surface reflection and volume scattering mechanisms responsible for the enhanced R_{sol} of the dual layer PTFE-Silver mirror structure.

Most polymer-based DPRCs adopt a metal solar reflective layer which is vulnerable/susceptible to oxidation by oxygen and moisture. This threatens its long-term solar reflectivity. Mandal et al. [104] developed a polymer-based radiative cooler with micro- and nanoscale pores in poly(vinylidene fluoride-cohexafluoropropene) ($P(VdF\text{-}HFP)_{HP}$) through phase inversion method to achieve high solar reflectivity in all directions and sub-ambient temperature reduction of 6°C. The solution-based fabrication process is conducted at room temperature, which allows such coatings to be applied to most building materials like wood, plastic and glass. The porous polymer has also been demonstrated to switch reversibly from a reflective (cooling) to a transparent (heating) state upon wetting with fluid. By equipping cooling panels based on this material with a wetting/drying mechanism, the cooling penalty of DPRCs in winter can be avoided [105]. Wang et al. [106] fabricated a PMMA cooler with

periodic scattering micropores embedded with random nanopores. Their cooler realized 6.0-8.9°C below ambient temperature during midday without the need of metallic back reflectors. In addition to synthetic polymers, modified generic building materials have also been studied. Li et al. [107] engineered a natural material, wood, through a process of delignification and densification. The randomly aligned nanofibers and vascular chambers in the wood serve as scattering elements, which provide broadband reflection whilst the molecular stretch vibrations provide high emissivity in the infrared region.

Gaseous alternatives are superior to solid coatings in that they do not require an additional heat transfer fluid to deliver the cooling power of the DPRC. Slabs of these gases, namely ammonia (NH_3), ethylene (C_2H_4) and ethylene oxide (C_2H_4O), in cells backed by reflective mirror-like surfaces have been investigated for their cooling potential [108-110]. In addition to IR-selectivity, they are cheap, widely available and have a low boiling point. C_2H_4 is highly emissive in the central region of the AW. C_2H_4O is strongly absorbing at the high and low frequency ends of the interval. Therefore, mixtures of the two gases have optimized radiative properties. Ammonia is superior in terms of cooling power generated near ambient temperature [109, 110]. Despite promising results, the full cooling potential of these gases could not be realized as a result of the poor insulation of the device, i.e., there is a need for more efficient convection shields that are sufficiently infrared transparent. Moreover, the enclosure deteriorates the radiative properties of the enclosed gas due to residual absorption, and the integration of solar reflectors is more complicated for gaseous PRCs than alternatives.

4.1.2. Nanophotonic Structures

Bulk materials with both high solar reflectivity and selective emissivity are rare. Instead, materials can be artificially engineered to have desired optical properties through their geometry and orientation, i.e., metamaterials. These emerging photonic crystals, or

nanophotonic devices, with periodic subwavelength structures, can be a periodically layered multi-stack (1-D) or multidimensional (hole lattices/multiple 2-D layers stacked together).

4.1.2.1. One-dimensional Nanophotonic Structures:

The index mismatch between adjacent layers of a multilayered DPRC gives rise to electromagnetic wave reflection. Interference of waves reflected from the cascade of boundaries results in selective emissivity of the structure. The stacking sequence and the layer thicknesses of the cooler are optimized to increase the optical path length that the EMR (electromagnetic radiation) travels through interference, thereby achieving broadband emissivity in the mid infrared region of the spectrum [111].

The earliest such example is the 7-layer alternating high index HfO_2 (hafnium dioxide)/low index SiO_2 (silicon dioxide) and a silver layer DPRC by Raman et al. [99], which is the first DPRC to demonstrate sub-ambient cooling under direct sunlight with a superior R_{sol} of 0.97 (Fig. 16a, 1). The bottom four layers of SiO_2 and HfO_2 are thinner and primarily responsible for solar reflection, while the top three layers are much thicker and designed for thermal radiation. Collectively, these material properties and the interference effects facilitate cooling density of 40.1 Wm^{-2} and temperature difference of 4.9°C below ambient, when exposed to 850 Wm^{-2} of direct sunlight using a test set-up to minimize nonradiative heat losses, as shown in Fig. 16a, 2 [99]. The HfO_2 layer could be replaced with a less expensive TiO_2 layer. An optimized multilayer TiO_2/SiO_2 structure by Jeong et al. [15] was able to achieve temperatures 7.2°C lower than ambient in humid conditions (60-70% RH). Chen et al. [112] used a vacuum chamber setup with ZnSe windows as the wind shield in a field test to minimize parasitic heat gains and provide a silicon nitride (Si_3N_4)/Si/Al emitter with radiative access to the outer space respectively. Additionally, a mirror cone and sun-shade were used to ensure that the emitter was exposed to diffuse sunlight when the experimental setup was under direct sunlight (Fig. 16b) [112]. A maximum temperature reduction of 42°C was recorded at peak solar radiance

under a clear winter sky in Stanford, California.

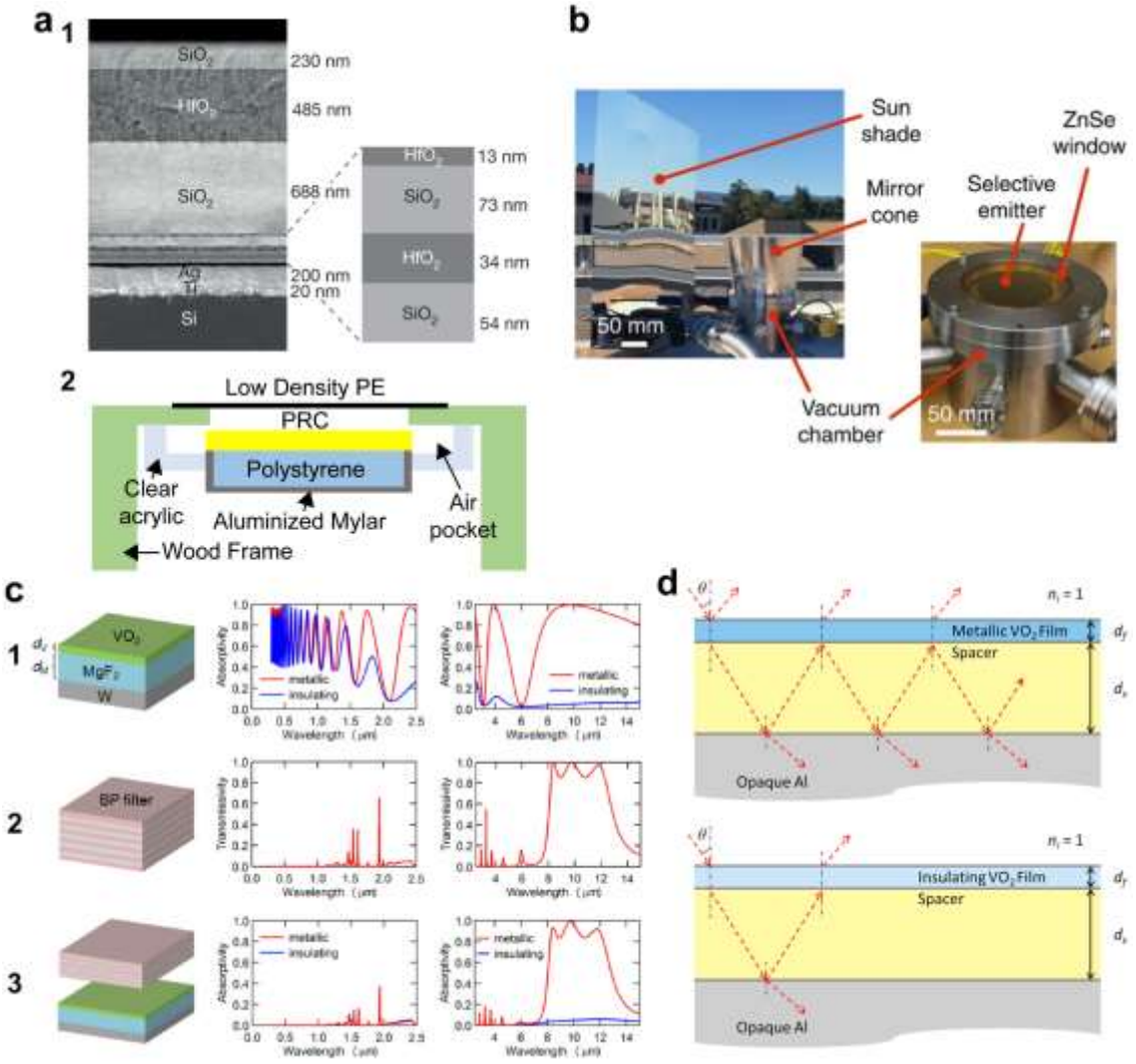

Fig. 16. a) (1) SEM image showing numerically optimized thickness of sublayers in HfO_2/SiO_2 photonic PRC and (2) typical configuration of test set up of the DPRC with an air pocket to minimize heat gain [99]. b) Apparatus used to eliminate thermal gains from ambient and optimize radiative output [112]. c) Absorptivity and transmissivity spectra of (1) $VO_2/MgF_2/W$ photonic structure, (2) bandpass filter and (3) combined system [113]. d) Schematic representation of wave propagation in VO_2-based Fabry Perot emitter in its metallic (cooling ON) and insulating (cooling OFF) states [114].

The use of complex and costly techniques like evaporation deposition used to fabricate the

cooling stack is a hurdle in terms of scalability, given the large coverage areas of roof radiators. Bao et al. proposed a more cost-efficient ($ 7/m^2) spray coated double layer coating composed of densely packed TiO_2 and SiO_2/SiC nanoparticles on a reflective aluminum substrate [115]. The TiO_2 nanoparticle layer serves as a solar reflector, due to its strong sunlight scattering behavior. The device meets the prerequisites for sub-ambient cooling with R_{sol} of 90.7% and average emissivity of 90.11% in the transparent window. Although the TiO_2/SiC coating cooled an aluminum substrate by up to 8°C during field tests on a rooftop in Shanghai, the elevated humidity prevented the device from reaching sub-ambient temperatures, despite theoretical predictions of 5°C.

Polymer incorporated cooling stacks have promising prospects as daytime radiative coolers. Gentle and Smith [116] used an all-polyester mirror comprising of 300 coextruded bilayers of the birefringent polymers PET and ECDL, with R_{sol} of 0.97 and spectral emissivity of 0.96 in the sky window, to generate temperatures 2°C below ambient without convection shields. This material is highly durable, even under direct sunlight. Numerical analyses by Takahiro et al. [117] found that the net emissive power of a PMMA-based cooling device was compromised when the precipitable water vapor increased, as it caused the secondary AW at 16-25 μm to lose transmissivity. Therefore, it is imperative for DPRCs to be adopted in warmer and humid regions, to minimize the emissivity of wavelengths outside the primary sky window (8-13 μm) if practical daytime cooling is to be achieved.

The use of VO_2-based thermochromics (TC) has also been studied for automated temperature control using PRCs. The thermochromicity of VO_2 allows the PRC to passively adapt from radiatively cooling to suppressing thermal emission and vice versa, depending on temperature. Such self-adaptive PRC was designed by Ono et al. [113], whose device consists of a three-layer VO_2/MgF_2/W structure. At high temperatures, when the VO_2 exists in its metallic state, the device acts as a Salisbury screen absorber, i.e., a portion of the incident radiation is reflected

at the top layer (VO_2); the split wave travels through the spacer material and is reflected at the ground plane (W) to eventually undergo destructive interference at the surface with the first wave. This phenomenon is absent when the VO_2 is in its semiconducting phase. Therefore, the emissivity of the structure is suppressed. In simulations of a typical sunny day in Stanford, California, the DPRC achieved maximum temperature difference of 9°C. Its performance was supplemented by a selective filter (optimized 11-layer Ge/MgF_2 stack) that acted as both a solar shade and band pass (BP) filter in the 8-13 μm range (Fig. 16c) [113]. Similarly, Taylor et al. [114] realized selective absorption using a DPRC whose structure consists of two mirrors (VO_2/Al) separated by a lossless spacer. The Fabry-Perot resonance cavity formed when VO_2 becomes metallic (above 345 K) causes wave interference, thereby enhancing its absorption in the mid-IR range (Fig. 16d).

For these types of DPRC, the thickness of the spacer material determines the resonant wavelength of the structure, i.e., the resulting absorption enhancement. Moreover, the intensity and extent of the response can be tailored via the thickness of the surface layer [114]. The simplicity and tunability of these devices make them a promising technology for radiative cooling applications.

4.1.2.2. Multidimensional Photonic Structures:

Multidimensional photonic arrays with tailored spectral properties have been studied for DPRC applications including grating, square, spherical, nano-disk and air hole arrays. These devices absorb radiation primarily as a result of the excitation of surface plasmon polaritons (SPP) [118], which refers to a type of surface wave arising due to collective oscillations of free electrons at the interface between metals and dielectrics [119]. The excitation of these SPPs allows the energy of incident light with different wavelengths to be trapped in different regions inside the structure, enhancing its emissivity. Additionally, coupled incident electromagnetic radiation and localized magnetic resonance in nanostructures give rise to magnetic plasmon

polaritons (MPs). Excitation of these MPs can be used to control light propagation and consequently, a device's radiative properties [120]. The scale and periodicity of such structures are comparable to the wavelength of incident radiation. Therefore, advanced and expensive micro-/nano-fabrication technologies are involved in their production. Hervé et al. [121] proposed lamellar surface grating of SiO_2 on a thin film stack comprising of $Ag/HfO_2/BN/SiC/SiO_2$. Theoretical results supported the device's feasibility for daytime cooling applications, with 55 W/m^2 of daytime cooling power generated under the temperate conditions of Poitiers, France. The cooling power of a DPRC is greatly affected in a humid climate, where the atmosphere is only semi-transparent between 8-13 μm. Wong et al. [122] investigated the use of DPRCs with metallic gratings as 'filters' to facilitate asymmetric forward and backward radiation transmission between 6-15 μm. These windows allow the emission of radiation from the DPRC, while simultaneously reflecting the heavy incoming heat load, due to the atmospheric emissions resulting from the restricted AW. The study showed that when used with a DPRC, a cooling power of 50 W/m^2 could theoretically be restored.

Dielectric resonator (DR) metasurfaces, which can support many resonance modes, have also been researched for DPRC applications. Zou et al. [123] developed and experimentally verified the viability of a radiative cooling metasurface consisting of silver loaded P-doped n-type silicon rectangular DRs placed orthogonally to each other (Fig. 17a). The fabrication process is scalable, easily integrable with existing silicon-based photonics, and cost-effective due to its low material cost. Rephaeli et al. [100] designed a 2-layer lattice photonic structure made of thermally emitting Quartz and SiC with a periodic array of square holes on a stack of 5 MgF_2/TiO_2 bilayers which serves as the broadband solar reflector. The device has multiple emission peaks in the secondary sky window which benefit its radiative cooling performance (Fig. 17b). An array of symmetric conical pillars made of alternating Al and Ge layers was investigated by Hossain et al. [124] (Fig. 17c). In the presence of non-radiative heat gains, the

device's cooling effect persists. Similarly, a 2D tungsten conical antenna array fabricated using laser interference lithography and etching was proposed by Cho et al. [125]. The tungsten cones enhance scattering efficiency: scattering extends the optical length and consequently more light is captured by each cone/antenna, enhancing absorption. A sharp cut off wavelength beyond which emissivity significantly decreases is characteristic of these antenna structures. The cut off wavelength can be tuned as a function of the structure's aspect ratio. Moreover, an alumina coating was found to provide oxidation protection and improve the device's emissive properties by amplifying the antenna effect responsible for selective absorptivity.

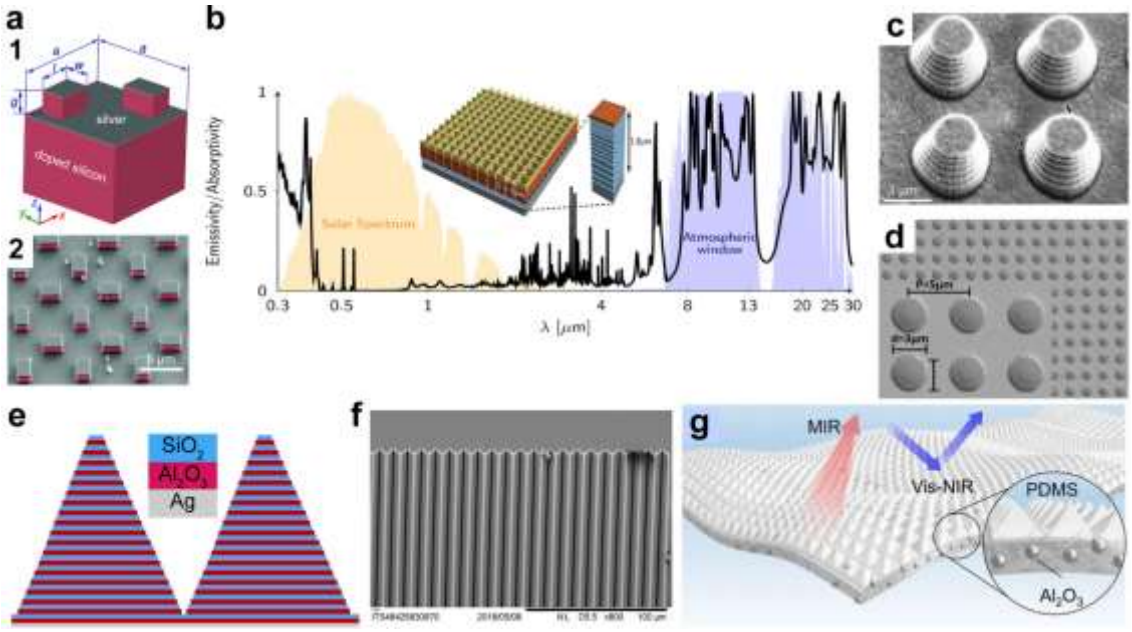

Fig. 17. a) (1) Schematic diagram and (2) SEM image of silver loaded P-doped silicon radiative cooling metasurface (a = 6.9 μm, g = 1.5 μm, l = 2.5 μm and w = 1.55 μm) [123].) Layer composition of quartz-SiC square lattice photonic crystal and associated emissivity spectrum with peaks in secondary atmospheric window [100]. c) SEM image of conical metamaterial (CMM) with alternating Ge and Al [124]. d) SEM image of thermal emitter with gold film (bottom) and GST nanodisk array (top) [126]. e) Photonic architecture of moth eye mimicking PRC with alternating layers of SiO_2 and Al_2O_3. f) SEM image of Saharan

silver ant inspired PDMS triangular prism array PRC [127]. g) Composition schematic showing Al_2O_3 ceramic nanoparticles embedded in PDMS matric with micro-pyramidal compact arrays [128].

Nanoparticle crystals present a cost-effective alternative to previously discussed metamaterials which require complicated fabrication processes that are time-consuming and consume harsh chemicals. These crystals consist of metasurfaces with densely packed nanoparticles in a periodic pattern. The resonance excitation of these structures produces selective emissivity [129]. Furthermore, Jia et al. [130] showed that proper oxidation improves the selective emissivity of such a cubic or hexagonal stack pattern of nanoparticles. For instance, a monolayer of oxidized aluminum nanosphere cores had enhanced absorptivity between 9-11.5 μm. Few DPRCs discussed hitherto fully utilize both transparent windows (8-13 μm, 16-25 μm). A device with high dual band emissivity, i.e., high absorptivity in both these regions could theoretically achieve much higher cooling efficiencies. Qu et al. [126] designed such device consisting of an array of phase-change $Ge_2Sb_2Te_5$: GST nanodisks (Fig. 17d). 2D photonic crystals that incorporate phase-change materials have also been presented in the literature, for instance, the VO_2-based DPRC [131].

Biological systems utilize micro/nano-architectures to counteract hyperthermia via radiative cooling. For instance, moth eyes have hexagonal arrays of subwavelength non-close packed corneal nipples, which generate a graded refractive index and act as an antireflective coating as a result of index matching [132]. Wu et al.'s DPRC replicated this effect using pyramidal nanostructures of alternating SiO_2/Al_2O_3 layers which were capable of suppressing solar absorption and near unity absorption in the AW simultaneously (Fig. 17e) [133]. Similarly, Jeong et al. [127] proposed a radiator inspired by the Saharan silver ant (Fig. 17f), whose triangular hairs facilitate thermoregulation even under extremely strong sunlight by (1)

inducing Mie scattering and (2) index matching. More recently, Zhang et al. [128] produced a flexible photonic film with a micro-pyramidal polymer matrix and random ceramic particles (Fig. 17g) inspired by the Longicorn beetle. Under direct sunlight, sub-ambient temperatures up to 5.1°C were achieved.

The cocoon of the comet moth controls solar reflection and mid-IR absorption to prevent overheating of the pupae inside [134], owing to the voids in cocoon fibers that have similar dimensions to visible/NIR wavelengths and consequently backscatter incident solar radiation. For wavelengths longer than the void dimensions, the scattering effect is diminished, and the radiation is absorbed instead. This concept is adopted in DPRCs with randomly aligned media discussed in the following section.

4.1.3. Randomly Packed Media/Composites

Radiative cooling devices made of particle embedded matrices utilize the scattering phenomenon to selectively reflect incident radiation. Unlike the nanophotonic approach, such hybridized photonics are more amenable to scaling up to meet the large surface area demand of commercial and residential DPRC applications. Harrison and Walton [135] demonstrated the radiative cooling ability of TiO_2 dispersed white paint that achieves temperatures 2°C below ambient. Despite the high emissivity (0.92) of the white paint in the sky window, TiO_2 significantly absorbs UV, which limits its cooling performance. The inclusion of $BaSO_4$ extender in the paint improves its IR selectivity [136]. A further temperature decreases of up to 3.2°C can be obtained with such a paint coating. A double layer coating of acrylic resin embedded with TiO_2 and carbon black particles that can be used for both daytime and nighttime cooling applications was presented by Huang and Ruan [137]. The high index TiO_2 dispersed layer facilitates high reflectivity in the solar spectrum. The carbon black particles, which can be either incorporated in a polymer matrix or sprayed at the bottom of the reflective layer, act

as a blackbody to maximize the emissivity of the coating in the AW. While high-index TiO_2 particles scatter light efficiently, these particles have high intrinsic absorption of UV, which accounts for 5% of solar radiation. Therefore, focus has shifted to optimizing the scattering behaviour of randomly packed low index particles like SiO_2.

Zhai et al. [138] introduced an extremely cost-effective and scalable passive cooling solution with randomized SiO_2 microspheres dispersed in the polymer TPX and backed by a 200 nm silver layer (Fig. 18a). The cooler is extremely emissive across the entire AW due to phonon-enhanced Frohlich resonances of the embedded microspheres. In addition to generating a net cooling power of 93 Wm^{-2} during the day, the cooler can be manufactured on a large scale by roll-to-roll extrusion and web coating systems, which makes large-scale application of radiative cooling possible. Fang et al. [139] found that using the coating on a roof of a building could save up to 113.0-143.9 kWh/m^2 of cooling electricity annually compared to a traditional shingle roof. A recent study by Lin et al. [140] produced an ultradurable DPRC, which is capable of achieving up to 2°C temperature reductions in humid Hong Kong summer without sun shades or convection covers. The device consists of SiO_2 microspheres self-assembled on a SiO_xN_y film on a reflective substrate. Both its performance and fabrication (which involves solution-based processing) make it promising for large area applications in tropical regions. A similar randomly packed SiO_2 microsphere coating was able to achieve 12°C below ambient in sunlight without using a back reflector [141]. By eliminating the need for expensive metals like silver, the coating can be manufactured easily at low cost, and can be applied to any surface as a paint. The study concluded that the fill factor, size and material of the random media could be exploited to produce the required optical response. A porous anodic aluminum oxide (AAO) membrane on aluminum film was demonstrated to reach 2.6°C below ambient on a sunny day in Hangzhou, China [142]. The dilution of air holes in the medium (Fig. 18b) improves impedance matching with the surrounding air, thereby minimizing reflections. The incident

solar radiation, therefore, penetrates the AAO membrane with minimal attenuation, where it is then completely reflected by the ground metal layer. Few radiative cooling technologies fulfill the popularity of and/or the demand for color diversity and tinted facades in contemporary architectures. Red, green and white colored emitters using silica-embedded perovskite nanocrystals in PMMA composite PRCs were successfully devised by Son et al. [143] and presented aesthetically pleasing alternatives to white and metallic PRCs (Fig. 18c). More recently, Zhai et al. synthesized single colour radiative cooling coatings that achieved temperature drop of 2.31°C (and 68 Wm^{-2} cooling power), using low cost oxide materials and solvothermal reaction [144].

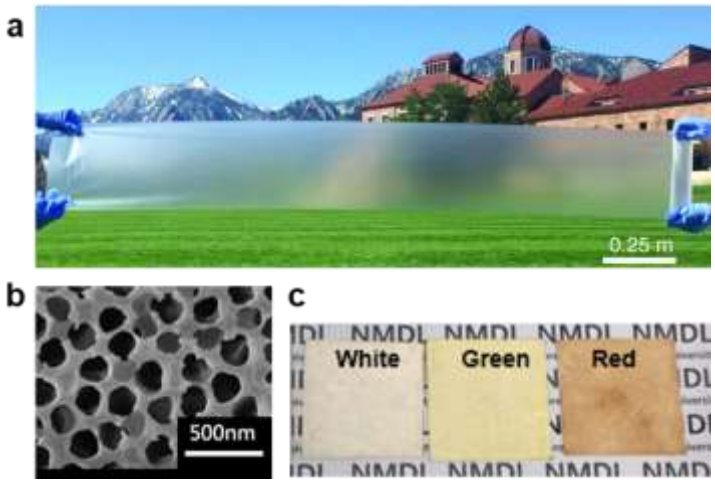

Fig. 18. a) Roll-to-roll fabricated sample of glass polymer hybrid metamaterial produced at a speed of 5m/min (prior to silver coating) [138]. b) Micrograph of top of an AAO sample [142]. c) Silica-embedded perovskite nanocrystals in PMMA in white, green and red [143].

4.2. Comparison of Reviewed Daytime Passive Radiative Coolers

4.2.1. Spectral Properties of Reviewed DPRCs

The details of DPRC included in this review are summarized in Table 3. However, as the field tests were conducted under different conditions such as ambient temperature, cloud coverage

and RH that play significant roles in cooling performance, it is not wise to compare the cooling power and/or the maximum temperature difference achieved by the DPRCs. Alternatively, radiative coolers can be quantitatively compared by defining cooling parameters that characterize the requirements of an ideal DPRC device (unity emissivity in the AW and zero elsewhere to minimize P_{atm}). In this study, following a similar approach to DPRC comparison as [145], the variables, e_{in} and e_{out}, are defined to evaluate the devices' spectras' fit with the ideal DPRC illustrated in Fig. 19a.

$$e_{in} = \frac{\int_{13\ \mu m}^{8\ \mu m} d\lambda I_{BB}(\lambda,T_a)\times e(\lambda)}{\int_{13\ \mu m}^{8\ \mu m} d\lambda\ I_{BB}(\lambda,T_a)} \tag{10}$$

$$e_{out} = \frac{\int_{0\ \mu m}^{\infty\ \mu m} d\lambda I_{BB}(\lambda,T_a)\times e(\lambda) - \int_{13\ \mu m}^{8\ \mu m} d\lambda I_{BB}(\lambda,T_a)\times e(\lambda)}{\int_{0\ \mu m}^{\infty\ \mu m} d\lambda\ I_{BB}(\lambda,T_a) - \int_{13\ \mu m}^{8\ \mu m} d\lambda\ I_{BB}(\lambda,T_a)} \tag{11}$$

$$I_{BB}(\lambda,T_a) = \frac{2\pi hc^2}{\lambda^5} \times \frac{1}{e^{\frac{hc}{\lambda kT}-1}} \tag{12}$$

$$A_{sol} = \frac{\int_{0.3\ \mu m}^{2.5\ \mu m} d\lambda i_{AM1.5}(\lambda)\times e(\lambda)}{\int_{13\ \mu m}^{8\ \mu m} d\lambda\ i_{AM1.5}(\lambda)} \tag{13}$$

Where e_{in} and e_{out} are the emissivities within and outside the atmospheric window respectively, c, h and k are the speed of light, Planck's constant and Boltzmann's constant, respectively and ambient temperature, T_a, is assumed to be 25°C. These values are evaluated using published emissivity spectra, with the Planck's blackbody radiation function, I_{BB} of a body at room temperature (T_a = 298 K) used as an integrating accessory [146]. Similarly, the solar absorptance, A_{sol}, of the coolers were derived using $i_{AM1.5}$, the global solar spectra, as a weighting function.

The e_{in} and e_{out} values are summarized in Table 3 and Fig. 19b (DPRCs are numbered 1-21 with the most recent last). Devices with limited spectral data (less than 20 μm) are not

represented in the graph for fair comparison. It is evident from Fig. 18c that the ideal selective emitter is still elusive. While it appears that unity e_{in} has been achieved in recent years, it has been at the expense of e_{out}, limiting the DPRC's sub-ambient cooling potential due to increased absorption of wavelengths outside 8-13 μm. However, despite this, the field tests suggest that the devices can still achieve substantial sub-ambient temperatures during the day if A_{sol} is sufficiently small. Therefore, suppressing A_{sol} is key to a successful DPRC. This can be realized through the DPRC's inherent absorption characteristics or sunshades/solar covers used externally (discuss in **Section 4.3**).

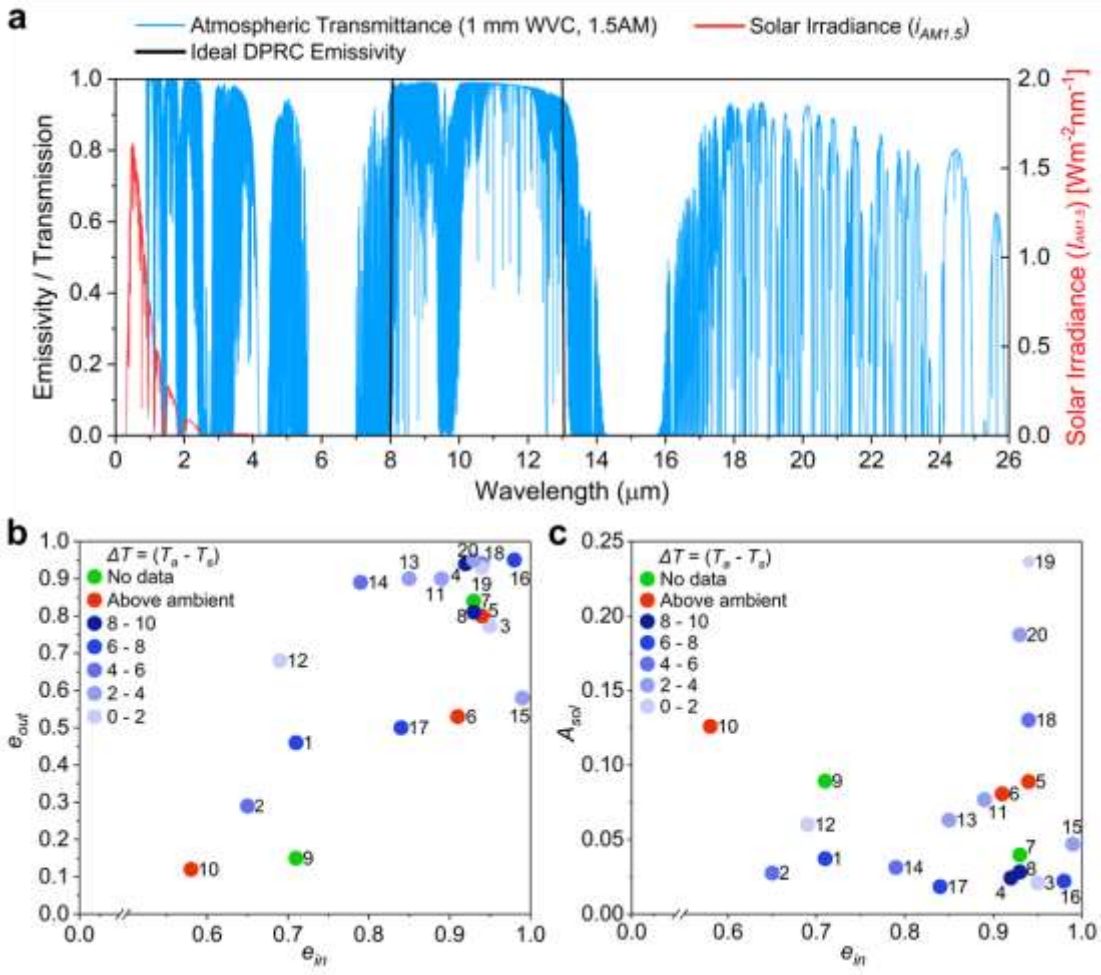

Fig. 19. a) Emissivity spectrum of an ideal DPRC. Atmospheric transmission and solar irradiance for 1.5 AM and 1 mm water vapor column (WVC) are depicted on the left and

right vertical axes, respectively. b) Emissivity within (e_{in}) against emissivity outside (e_{out}) atmospheric window for selected DPRCs. c) Emissivity within atmospheric window plotted against solar absorptance (A_{sol}) for selected DPRCs. Color gradient used to visualize cooling potential (difference in temperature of radiative surface (T_s) and ambient (T_a). DPRCs from literature labeled (in publication order) as follows: (1) Square lattice [100], (2) HfO_2/SiO_2 multilayer [99], (3) Vikuiti enhanced specular reflector on silver [116], (4) PDMS on Ag mirror [101], (5) SiC+TiO_2 NP/Al [115], (6) SiO_2+TiO_2 NP/Al [115], (7) SiO_2 in TPX [138], (8) Moth-eye mimicking structure [133], (9) Lamella grating on stack [121], (10) PMMA/SiO_2/Al [117], (11) Cooling wood [107], (12) $NaZnPO_4$/Al [147], (13) Ultra-white glass plated Ag [147], (14) SiO_2 mirror [148], (15) Porous alumina [142], (16) Saharan ant mimicking polymer surface [127], (17) TiO_2/SiO_2 multilayer [15], (18, 19, 20) Silica-embedded perovskite nanocrystals (white, red, green) [143].

High atmospheric transmittance is also very important in generating high net radiative cooling power, although it is strongly dependent on the geographic location and local climate. Therefore, the design of DPRC should not only consider the sub/above ambient cooling requirement, but also where it may be deployed. Lower RH leads to higher atmospheric transparency, i.e., the AW closes when the precipitable water content increases and emissions in this range can no longer reach outer space. This means that the same DPRC can have different cooling effects in two locations. For instance, Raman et al. [99] achieved cooling up to 20°C in Stanford, California. However, using a similar setup and cooler, Tso et al. [149] could only reach a maximum nighttime temperature difference of 7°C with clear sky and did not observe any daytime cooling effect in Hong Kong with hot and humid weather. Likewise, a DPRC with e_{in} of 0.79 tested in two climates (Beijing: RH ~20% and Hefei: RH ~80%) showed drastically different cooling performances [148]. DPRCs that have shown success in

field tests in humid climates (up to 70% RH) have characteristically high e_{in}: silica embedded perovskite DPRC (0.94), porous alumina DPRC (0.99), P(VdF-HFP)HP DPRC (0.99). Sub-ambient cooling in humid conditions is also possible for lower e_{in} if e_{out} is sufficiently small (e.g. SiO_2/TiO_2 DPRC, e_{in} = 0.84, e_{out} = 0.51). Therefore, a DPRC's suitability for hot and humid climates is conditional on its optimized optical properties both within and outside in the AW.

4.2.2. Cost Analysis on Reviewed DPRCs

Cost and difficulty to scale up economically remain the biggest hurdles for many DPRCs. While 2-D photocrystals for radiative cooling have shown incredible promise, these metamaterials are among the most expensive to mass produce. Such devices often involve costly inorganic raw materials and expensive and complicated precision fabrication methods to achieve the complex architectures. However, existing wafer photolithography facilities can be used to produce some periodic patterned devices at a reasonable cost by roll-to-roll nanoimprint lithography [100, 123]. Nanoparticle-based photocrystals, like the monolayer nanosphere crystal proposed by Jia et al. require less time to fabricate than conventional lithography-based devices [130].

1-D metamaterials which consist of multilayer stacks, require less complex fabrication methods like electron beam evaporation, but are still expensive to produce, especially on a large scale. A performance assessment of the HfO_2/SiO_2 multilayer DPRC conceptualized by Raman et al. [99] found that based on energy savings, the acceptable incremental cost for such a device ranged from \$7.5 - \$18.7/m^2 for a payback period of 15 years [150]. However, the multilayer cooler that was the subject of the study was estimated to cost up to \$70/m^2. Manufacturing costs could be lowered by using a cheaper substitute for HfO_2; for example, using TiO_2 could achieve a 17% price reduction [15]. Regardless, the evaporation deposition process used for

fabrication is still expensive and suited for wafer-based devices and has low yield so the scalability of these DPRCs for rooftop coverage is questionable. Granted, inorganic based multilayer stacks have high corrosion resistance and robust mechanical properties and can be tailored to achieve custom spectral properties through exhaustive modeling using Maxwell equations. However, polymer stacks are cheaper and more practical alternatives.

Polymer-based DPRCs are superior in terms of cost and can be scaled up cost effectively [104, 116, 117]. Moreover, these DPRCs are flexible and therefore integrable with curved surfaces. A study of the energy saving potential of the RadiCold (SiO_2/TPX hybrid) DPRC calculated a maximum allowable incremental cost of \$50-78.9/m^2 for a payback period of 8 years [151]. For a 3-year threshold in another study for the same DPRC, the calculated allowable cost was \$30.0-\$55.2/m^2 [139], which is comparatively higher than inorganic DPRCs. Porous polymers like P(VdF-HFP) used by Mandal et al. for daytime radiative cooling are available commercially or can be produced using large scale methods for very low cost [104]. However, while polymer films that have been optimized to withstand outdoor elements are commercially available, many are still susceptible to yellowing, aging and cracking especially following prolonged exposure to UV and moisture. Therefore, maintenance and replacement costs and service life must be factored in when assessing the economic rationality of such polymer based DPRCs.

Researchers have also turned to natural raw materials which are both cost effective and environmentally friendly options, for daytime radiative cooling [107]. DPRCs typically comprise of a silver back layer that functions as a mirror to achieve high solar reflectance. The elimination of this back reflector or its replacement using cheaper metals such as aluminum reduces material cost [115, 141]. A study by Ao et al. fabricated a specular DPRC using ultrawhite glass plated silver at a cost of \$30/m^2, the precious silver accounting for bulk of the cost [147]. However, the diffuse DPRC surface with zinc phosphate sodium particles on a

cheaper aluminum substrate from the same study cost only $\$8/m^2$ to produce, and yet was able to achieve sub-ambient cooling. Spray coated nanoparticle coatings on aluminum can be produced at a similar price point ($\$7/m^2$) [115].

Further, the high cost involved in daytime radiative cooling installations is not simply limited to the photonic cooler. The expensive enclosures and shading mechanisms incur additional costs. The vacuum ZnSe enclosure discussed in Section 4.1.2 [112], while beneficial, is too expensive for practical application, i.e. low-cost alternatives must be sought. Little has been written about the cost aspect of these accessories. Since a majority of DPRCs involve expensive fabrication techniques and materials, extended payback periods may be inevitable. However, one could reduce the assumed payback period by integrating DPRCs on rooftops with (thermo)photovoltaic modules which can harness the sunlight reflected by the cooling devices. Doing so would allow the accelerated recovery of the initial investment cost while fulfilling net zero building aspirations.

Table 3. Summary of DPRC performance reported in literature and performance indices of selected DPRCs calculated[a)] using published spectra.

PRC Technology	Locale[b), c), d)]	Net Cooling Power[e)] (W/m^2)	ΔT[f)] (°C)	e_{in}[g)]	e_{out}[h)]	A_{sol}[i)]	Ref
$PMMA/SiO_2$	Simulation (h_c=12 W/m^2K)	-	1.3 (daytime);	0.58	0.12	0.13	[117]
	Okayama, Japan (T_a=35°C, 20 m altitude); P	-	-2.8 (daytime, sub-ambient not achieved due to high PWW)				
HfO_2/SiO_2	Stanford, California	40.1 (daytime)	5 (daytime); 19.5 ($h_{cond+conv}$ = 0)	0.65	0.28	0.03	[99]
$NaZnPO_4$/Al	Beijing (T_a = -6-8°C)	-	1.5 (daytime); 7.3 (nocturnal)	0.69	0.66	0.06	[147]
Square Lattice Quartz/SiC/MgF_2/TiO_2/Ag	Simulation (h_c=0 W/m^2K; h_c=12 W/m^2 K)	105 (daytime)	40 (daytime); 7 (daytime)	0.71	0.37	0.04	[100]
Lamellar SiO_2 grating/SiC/BN/HfO_2/Ag	Simulation: Poitiers, France	55 (daytime); 80 (nocturnal)	-	0.71	0.15	0.09	[121]
SiO_2/Ag/SiO_2	Beijing (T_a=2-6°C, RH=10-20%)	-	5.9 (daytime)	0.79	0.94	0.03	[148]
	Hefei (T_a=10-15°C, RH=50-80%)	-	N/A				
Ag-loaded P-doped Si DR/Ag	Simulation (h_c=6.9 W/m^2K)	95.84 (daytime)	7.36 (daytime); 10.29 (nocturnal)	0.82	0.55	0.03[j)] (4-16.5 μm)	[123]
Al/Ge conical pillars	Simulation (h_c=6.9 W/m^2K)	116.6 (nocturnal)	9 (daytime); 12.2 (nocturnal)	0.82	0.28	0.03[j)] (5-16.5 μm)	[124]
SiO_2/TiO_2/Ag_1	Simulation: Istanbul, Turkey	103	-	0.83	0.42	0.02 (0.3-14 μm)	[152]
SiO_2/TiO_2/Ag_2	Hong Kong (January, RH=60-70%)	14.3 (daytime)	7.2 (daytime)	0.84	0.51	0.02	[15]
VO_2/MgF_2/W	Simulation: Stanford, California	~120(daytime)	9 (daytime)	0.84	0.12	0.00 (0.3-15 μm)	[113]
Ultra-white Glass/Ag	Beijing (T_a=-6-8°C)	-	2.5 (daytime); 9.8 (nocturnal)	0.85	0.93	0.06	[147]
Delignified Wood	Cave Creek, Arizona	16 (daytime); 63 (nocturnal)	4 (daytime); 9 (nocturnal)	0.89	0.90	0.08	[107]
TiO_2 and SiO_2 NP/Al	Simulation (Dry air, h_c=4 W/m^2 K)	-	5 (daytime)	0.91	0.60	0.08	[115]
	Shanghai, China (T_a=24-32°C, RH=50-70%)	-	5 (nocturnal)				
PDMS/Silica/Ag	Pasadena, California	127 (daytime)	8.2 (daytime); 8.4 (nocturnal)	0.92	0.93	0.02	[101]
PTFE/Ag	Simulation (h_c=0-10 W/m^2 K; high elevation, clear atmosphere)	171.3 (daytime)	11 (daytime)	0.92	0.89	0.01 (0.3-15 μm)	[103]

SiO_2 in TPX/Ag	Cave Creek, Arizona	93 (daytime)	-	0.93	0.82	0.04	[138]
Moth Eye mimicking (SiO_2/Al_2O_3)	Simulation	122	47 (h_c = 0 W/m^2 K); 10 (h_c = 12 W/m^2 K)	0.93	0.76	0.03	[133]
Silica embedded perovskite	Seoul, South Korea (T_a=-2-12°C;	-	Green 3.6 (daytime); 6.7 (nocturnal)	0.93	0.95	0.19	[143]
NCs/PMMA+ZnO/PET/Ag	RH=20-60%)	-	Red 1.7 (daytime); 6.7 (nocturnal)	0.94	0.93	0.24	
		-	White 4.2 (daytime); 6.3 (nocturnal)	0.94	0.94	0.13	
TiO_2 and SiC NP/Al	Simulation (Dry air, h_c=4 W/m^2 K)	-	5 (daytime)	0.94	0.84	0.09	[115]
	Shanghai, China (T_a=24-32°C, RH=50-70%)	-	3-4 (nocturnal)				
SiO_2 microsphere paint	Albuquerque, New Mexico	-	12 (daytime); 4 (nocturnal)	0.94	0.96	0.03[j)]	[141]
TiO_2/Carbon Black NP in resin	Simulation (h_c=0 W/m^{2}K)	100 (daytime); 180 (nocturnal)	22 (daytime); 45 (nocturnal)	0.94	0.96	0.08	[137]
				(0.3-13 μm)			
	Simulation (h_c=12 W/m^{2}K)	100 (daytime); 180 (nocturnal)	6 (daytime); 11 (nocturnal)	-	-	-	
PET ECDL bilayers (Vikuiti Enhanced Specular Reflector)	Sydney, Australia ($T_{a,peak}$=27°C; No convection shields)	-	2 (daytime); 7 (nocturnal)	0.95	0.77	0.02	[116]
Logicorn Beetle like Micropyramidal polymer + random ceramic particles	Shanghai, China (RH=22.7%)	90.8 (daytime)	5.1 (daytime)	0.97	0.90	0.06	[128]
				(0.3-16 μm)			
Saharan Ant inspired PDMS triangular prism	Simulation	144 (daytime)	-	0.98	0.97	0.02	[127]
	Hong Kong (RH=87%, $T_{a,peak}$=33°C, daytime; $T_{a,peak}$=19ºC, nocturnal)	19.7 (daytime); 14.3 (nocturnal)	6.2 (daytime)				
($P(VdF\text{-}HFP)_{HP}$)	Phoenix, Arizona (No convection cover)	96 (daytime)	6 (daytime)	0.99	0.91	0.04	[104]
	Chattogram, Bangladesh (Fog, haze)	-	3 (daytime)	(0.3-18 μm)			
	New York	83 (daytime)	5 (daytime)				
Porous Alumina	Simulation (RH=70%)	64 (daytime)	-	0.99	0.68	0.05	[142]
	Hangzhou, China (T_a=25-30°C)	-	2.6 (daytime)				
PDMS on Ag reflector	Hong Kong (Clear skies, no wind shield, RH=40-85%)	52.4 (daytime, 760 W/m^2 solar irradiance); 87.4 (nocturnal)	6 (daytime, maximum); 2.4 (48-hour average)	0.94	0.95	0.08	[102]
				(0.25-16 μm)			

Si_3N_4/SiO2/Ag	Simulation (h_c=6.9 W/m^{2}K)	87 (daytime)	-	0.84	0.49	0.03[j)]	[153]
	700 W/m^2 solar irradiance, RH=20%	-	8 (daytime)	(2.5-20 μm)			
Ethylene	Gothernburg, Sweden (T_a=5°C, RH=40%)	22 (daytime)	10 (daytime)	-	-	-	[110]
Ammonia	Gothernburg, Sweden (T_a=8°C, RH=82%)	-	8.5 (daytime)	-	-	-	[109]
	Simulation (h_c=1 W/m^{2}K)	26	15				
Ethylene + Ammonia	h_c=1 W/m^{2}K	85	20	-	-	-	[108]
PVF/Al (TEDLAR)	Naples, Italy (Dirty atmospheric conditions)	-	15 (daytime, diffuse sunlight)	-	-	-	[154]
Si_3N_4/Si/Al	Stanford, California (winter); Vacuum chamber with ZnSe windows and mirror cone shaded from direct sunlight	-	42 (daytime)	-	-	-	[112]
SiO_2/Si_3N_4/Al_2O_3/Ag	Seoul, South Korea	-	8.2 (daytime)	-	-	-	[155]
VO_2/SiO_2 wires/VO_2/SiO_2	Simulation	118 (T_{device}=67°C); 528 (T_{device}=69°C)	-	-	-	-	[131]
TiO_2 white paint	Calgary, Canada (Clear sky, 1.1 km elevation)	-	2 (daytime, direct sunlight); 15 (daytime, indirect sunlight); ~10 (nocturnal)	-	-	-	[135]
TiO_2 white paint with $BaSO_4$	Ljubljana, Slovenia (T_a~15.4°C)	-	~10 (nocturnal)	-	-	-	[136]
Si_2N_2O in urethane resin	(T_a=90°C)	0.132	-	-	-	-	[156]

[a)] Waveband for calculation of performance indices is 0.3-20 μm, unless specified otherwise; [b)] h_c is the heat transfer coefficient that accounts for non-radiative heat exchange; [c)] RH is the relative humidity; [d)] T_a is the ambient temperature; [e)] The net cooling power is the difference between incoming and outgoing radiative fluxes when the cooling process starts, i.e. $T_{surface} = T_a$; [f)] ΔT is the difference in temperatures between the DPRC and ambient; [g), h), i)] e_{in}, e_{out} and A_{sol} are the weighted averages of the emissivity inside and outside the atmospheric window and solar absorptance, respectively, and were calculated using Equations (10-13) unless otherwise specified; [j)] These A_{sol} values are obtained from the literature.

4.3. Radiative Cooling Accessories

4.3.1. Tapered Guides

The emissivity of a radiating surface is a function of the angle at which it is measured. Additionally, atmospheric emissivity is critically dependent on the zenith angle (angle between the sun and the vertical), remaining relatively constant from 0-60° but rapidly approaching unity for larger angles [146]. To maximize the cooling output of DPRC, it is important that thermal radiation is restricted to angles at which the surface emissivity is high, while atmospheric emissivity is sufficiently low. The performance of DPRC is also affected by the sky view factor, which is defined as the ratio between the visible sky and a hemisphere centered at a location [157]. Surrounding architecture plays a key role in determining the sky view factor, ergo cooling performance as it hinders sky access and the cooling output of DPRC is reduced when vicinal to tall buildings. Tapered waveguides have been employed to address these concerns. Chen et al. [112] used a cone mirror with ZnSe windows (Fig. 16b) to block high intensity low angle atmospheric radiation from reaching the selective radiator and facilitate cooling through a 24-hour cycle. Similarly, Zhou et al. [158] utilized a tapered square waveguide (Fig. 20) to simultaneously suppress solar input and control the directionality of the thermal emissions from the radiator. The guide suppresses normal incident solar radiation via a V-shaped shelter at the center of the waveguide. Despite promising results obtained in field tests, modular units consisting of the selective emitter and the three-dimensional waveguide may be challenging to implement in large-scale sky cooling applications.

Fig. 20. Tapered waveguide used as beaming component for PRC [158].

4.3.2. Thermal Insulation (Convection Shields and Isolated Enclosures)

The suppression of parasitic heating is key to maximizing the cooling potential of radiative coolers in sub-ambient cooling applications. Nonradiative heat gain includes convective heat gain (convection from warm air) and conductive heat gain (conduction). Convective thermal resistance is achieved using convection (wind) shields. Ideally, materials for wind shields must be highly transparent across the IR-region (especially in the AW), self-supported (eliminates the need for structural supports) with good outdoor durability. Radiative cooling panels span over large areas in practical applications, and hence low cost and high mechanical strength are also desirable. The design should prevent rainwater pooling on the surface which act as a barrier to outgoing radiation and causes damage due to excess weight exerted on the structure. Moreover, flexible foils under which convective currents are induced due to their sensitivity to wind velocity, are counteractive and should be avoided [159].

Polyethylene (PE) has been a frontrunning candidate for such covers, owing to its low cost and intrinsically high broadband transmittance. PE film is usually installed few centimeters above the radiative coolers where the air is trapped between DPRC and the cooler to suppress convection heat losses. Three-dimensional V-corrugated high-density PE (HDPE) shields were demonstrated to have enhanced infrared transmissivity (up to 73%) compared to flat foils [159]. However, PE is susceptible to aging when exposed to the sun, limiting its service life. Moreover, while thicker films may be utilized for more robust mechanical properties, a trade-off of transparency is inevitable [160]. In response to these challenge, a UV-stabilized porous PE cover was proposed by Gentle et al. [161]. The netting suppresses convective heat gain during nighttime, and the voids in the mesh structure allow heat to escape convectively during the daytime. The materials that have been investigated for wind shields are compared in terms

of relative cost, toxicity and mean transmittance in the atmospheric window in Table 4. The covering material also needs to have high R_{sol} to prevent heating caused by the sun during daytime. PE foils with non-absorbing pigments reflect and scatter sunlight. Alternatively, the pigmented foils absorb increased solar radiation, which is then dissipated through natural convection. By impregnating PE film with UV-resistant pigments, the durability of the cover is also improved. Both HDPE and low-density PE have been studied as substrates for solar shields. The latter has lower RI (1.51) compared to the former (1.53), which enhances the scattering effect when pigmented. However, HDPE has higher transmissivity in the AW. Table 5 summarizes the R_{sol} and transmittance in the atmospheric window, T_{AW} for different solar shields from literature.

Table 4. Properties of materials investigated for wind covers.

	Dimensions	Transmittance (transparence band)	Toxicity	Cost	Environmental Stability	Ref
PE	100 μm	73% (8-14 μm)	No	Low	Poor	[162]
HDPE foil	30 μm	85% (8-13 μm)	No	Low	-	[159]
Corrugated HDPE	4.5 cm	73% (infrared)				
HDPE polymer mesh	150 μm (fiber diameter)	80-90% (3-35 μm)	No	Low	High	[161]
ZnS	4 mm	64% (8-14 μm)	Low	High	High	[163]
ZnSe	7.1 mm	70% (8-14 μm)	Yes (contact)	High	High	[164]
Si	0.6 mm	47% (8-14 μm)	No	High	High	[162]
CdTe/Si	9.7 μm/1 mm	52% (side 1) 68% (side 2) (8-13 μm)	-	Low	High	[165]
CdS/Si	1 mm	80% (8-13 μm)	-	-	-	[165]

Table 5. Optical indices of solar shields for passive radiative cooling (pigmented PE foils unless specified otherwise).

	R_{sol}[a)]	T_{AW}[b)]	Ref
TiO_2/Carbon Black double foil (calculated using spectra)	0.428 (2.4 wt% TiO_2) -	- 0.733(0.5 wt% Carbon Black)	[166]
TiO_2 (vol% 5)	0.763	0.546	[167]
ZnS (vol% 5)	0.540	0.813	[168]
ZnO (vol% 5)	0.429	0.582	[168]
PbS thin film on PE	0.468	0.741	[168]
PbSe thin film on PE	0.274	0.508	[168]
PbS thin film on ZnS:PE	0.331	0.488	[168]
PbS thin film on ZnO:PE	0.286	0.406	[168]

Te thin film on PE	0.123	0.652	[169]

[a] R_{sol} is solar reflectance; [b] T_{AW} is transmission in atmospheric window.

The volume fraction, *f* and the diameter of pigment particles are imperative in optimizing the performance of the shield. When *f* is lower than 1%, the PE molecules absorb UV-radiation and the foil becomes pervious to solar damage. For larger *f*, the foil loses its plastic properties and becomes brittle and difficult to extrude. Andretta et al. [166] prepared double foil covers which were specular (rutile TiO_2) on the face exposed to the sun, and black (carbon black) on the opposite face. This design ensures that solar radiation transmitted through the top-facing surface is not trapped in the region between the cover and the radiator, and is instead absorbed by the lower foil. A 10 x 10 m^2 inverse greenhouse using the cover reached sub-ambient internal temperatures during the day. ZnS-pigmented 400 μm PE cover ($f = 0.15$) achieved cooling of a black emitting surface for more than 19 hours in the day [170]. However, ZnS pigment is not sufficiently stable for outdoor applications over extended periods and ZnO pigment is an alternative with better long-term stability. Coating pigment with an inert capping layer like SiO_2 or Al_2O_3 could extend the foils' longevity. Recently, Leroy et al. [171] developed a convection shield material made by polyethylene aerogel (PEA) with T_{IR} of 79.9%, low thermal conductivity (28 mW/mK) and high R_{sol} of 92.2% and thus the DPRC below this shield is not required to have high R_{sol} (Fig. 21a, b). PEA exhibits high reflectivity, owing to its porous nature and a thermal emitter with this shield obtained temperature reduction of up to 13°C under direct sunlight. The cooling power of 96 W/m^2 recorded was an approximate 22% increase from previous work for an uninsulated emitter. In addition, the conductive heat gain should be eliminated if ultra-large temperature reduction needs to be achieved realistically using DPRCs.

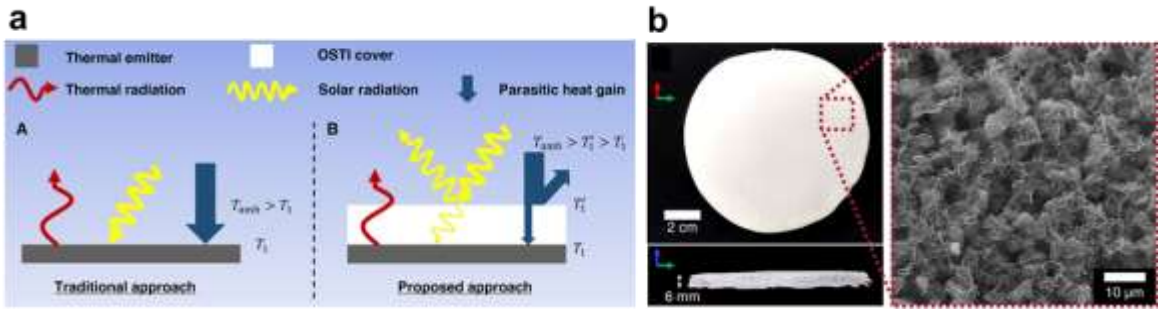

Fig. 21. a) Working principle of optically selective and thermally insulating (OSTI) cover for thermal emitter, and b) SEM image of PEA sample (10-cm-diameter and 6-mm-thick) [171].

Radiative cooling modules are typically placed in well-insulated enclosures made of insulating foam, polystyrene, or polyisocyanurate boards [172]. Alternatively, vacuum chambers are used. A selective surface placed in a chamber evacuated to a pressure of 10^{-6} torr, with 10 concentric reflective radiation shields inside, is capable of reaching temperature reduction of up to 42°C, albeit at the expense of cost and scalability (Fig. 16b) [112]. Fan et al. [173] proposed a multilayer structure with spacing between layers to suppress nonradiative heat input to the DPRC. The top and bottom coolers in the structure provide the middle cooler with low ambient temperature, improving its cooling potential. A 16% improvement from the single layer cooling performance was achieved experimentally with the multi-layer structure.

4.4. Building Integration with DPRC

Radiative cooling application in buildings can be broadly classified as active and passive. Note that in this review, the term “passive” refers to technologies with zero electricity input. A passive approach is exemplified by cool roofs, where the radiator is simply affixed to an object that needs to be cooled such as building roof. Despite the straightforward nature and accessibility of passive systems, they don’t provide the user with the means of controlling the device’s cooling power. This is detrimental during the heating period when unwanted cooling

could drive up energy usage. Moreover, the cooling potential is limited as cool roofs reduce the cooling load exclusively in the space immediately under the roof. Radiative cooling systems that utilize heat transfer fluid permit users to target and deliver cooling as required. Despite the passive nature of the radiative cooling process, such a hydronic cooling mechanism based on the concept is not entirely passive: energy is expended for coolant circulation. Therefore, those systems with fan or pump are described as active systems. They follow one of the two design approaches: (1) closed loops or (2) hybrid systems. Close-looped structures comprise of a heat transfer fluid system used in conjunction with flat plate radiative panels. By integrating with a fluid system, the cooling power generated by the selective radiator is collected and delivered to the building space. Both water- and air-cooled systems have been studied for this purpose. Hybrid configuration is a multiple system combination, in which the DPRC is used with other cooling mechanisms/components like cooling coils, evaporative coolers, cold water reservoirs etc. Recent research aims to address the key challenges for such systems: efficiently harnessing the low cooling energy flux of the radiators and minimizing parasitic losses to the surroundings. While photonic structures and materials for daytime radiative cooling have been extensively studied, little has been written on the practical applications of available daytime cooling technologies in buildings. The following section will discuss different daytime radiatively cooled active building configurations that have been presented in literature.

The performance of DPRC is greatly influenced by ambient conditions and thus its cooling potential is constantly fluctuating/transient. Moreover, the fluid cooled by such cooling systems is only several degrees colder than ambient air, as opposed to typical chilled water used for space conditioning which averages around ~7°C. For this reason, a radiative cooling system cannot meet the cooling demand by itself. Therefore, hydronic radiant distribution systems are integrated with a supplementary cooling system (hybrid configuration), where they provide complementary *in situ* cooling during daytime and utilize thermal storage of cooling flux at

night when the cooling demand is much lower. Wang et al. [150] studied the energy conservation potential of a radiant cooling system, based on a photonic DPRC [99]. The cooled water complements an air-cooled chiller which operates when the passive cooler is unable to meet the cooling setpoint level (Fig. 22a). Excess cooling flux charges the thermal storage tank. The cooling energy is delivered to the indoor space via hydronic radiant floors with water tubes embedded in cement screed. EnergyPlus simulation showed energy savings between 45-68% in four climate zones in the U.S., when the radiant cooling system deployed in 60% of the roof area.

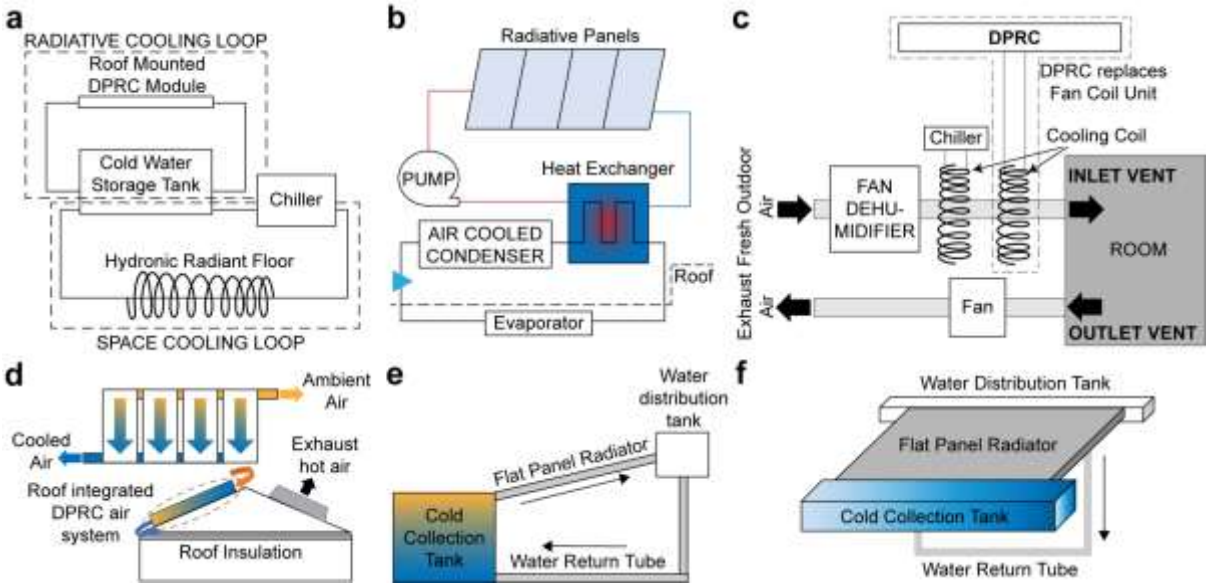

Fig. 22. a) Hydronic radiant cooling system with thermal storage complemented by an air-cooled chiller. b) DPRC system with serially connected panels used to lower the air conditioning refrigerant temperature at the condenser inlet. c) Single loop DPRC system to reduce heat exchange losses by delivering cooling energy directly to air. d) Air cooled DPRC system that circulates cooled ambient air to reduce attic temperature and alleviate cooling load. e) Front and f) cross sectional views of a thermosiphon module consisting of a tilted DPRC panel, cold storage tank and water distribution tank connected via a water return tube. Water cooled by the panel enters the storage tank under the influence of gravity, and warmer

uncooled water at the bottom of the tank is forced to the distribution tank through the return tubing, where it is channeled through the flat plate radiator for cooling in a cyclic process.

The efficiency of a typical air-cooled chiller drops dramatically when the condenser temperature is high. The air around the chiller unit becomes hotter as the device operates and less heat is removed from the cooling fluid. By using DPRC to sub-cool the refrigerant at the condenser inlet, the efficiency of the vapor compression cooling system can be significantly elevated. A water and glycol mixture was used as the working fluid in a cooling system that used the radiative cooling 3M Vikiuiti ESR film (Fig. 22b) [174]. In a two-storey commercial building in Las Vegas, with three parallelly connected radiative panels covering 60% of the roof, 21% of electricity consumption was saved annually.

The systems discussed hitherto utilize two cooling loops dedicated to radiative cooling and space cooling respectively. Jeong et al. [175] undertook a simpler approach with a single loop, where the DPRC replaces the fan coil unit (FCU) chiller (Fig. 22c). Chilled water in the isolated loop removes heat from air flowing through the FCU, improving the system's efficiency as the working fluid delivers its cooling capacity directly to air, instead of undergoing several heat-exchange steps. A near-ideal passive radiative panel is simulated with microchannels for fluid flow on the underside. Under clear sky conditions, the proposed system saved 22% of total energy with a cooler area of 100 m^2. There exists a positive correlation between the supply air temperature and the cooling power of the radiative cooler. Therefore, if the cooler is used to precool the hot air which can then be directed to the chiller for further cooling or encased in well-vacuumed conditions, higher savings can be achieved.

Zhao et al. [172] proposed a radiatively cooled-cold storage cooling (RadiCold) system to cool the condenser in a commercial office building. The cooling system showed cooling electricity consumption improvement between 32-45% in the summer in three US cities. The same lead

author [176] also investigated an air-cooled systems based on RadiCold metafilm (Fig. 22d) to achieve cooler attic temperatures in two-storey residential buildings. The proposed system cools ambient air through a series of parallelly connected radiative panels, which is then mixed with attic air. The radiative panels adopt a baffled design to encourage heat transfer between the working fluid (air) and the metamaterial surface by creating turbulent flow. The performance of the proposed cooling system far surpassed traditional energy saving methods like attic ventilation and cool roofs, with cooling savings between 26.5-76.1%. The results suggested that excessive attic insulation may be forfeited in buildings where radiative air-cooling systems are implemented.

One of the challenges of radiative cooling is the inherent low cooling density of these devices. However, the cooling energy intensity of a radiative cooled system can be scaled up by networking multiple fluid cooling modules and cold storage tanks [177, 178]. Zhang et al. [177] designed a demand pipe network of several thousand RadiCold modules and cold reservoirs that are collectively capable of delivering 4,096 kW_{th}/day. The capacious cold storage system addresses the temporal mismatch between the cooling energy supply and demand. A smaller kW-scale cooling system was proposed by Aili et al. [178], in which 10 RadiCold modules (13.5 m^2) were installed on the roof of a building in a 2 x 5 array. The modules were placed at a tilt angle to both reduce solar irradiance exposure and ease water filling of the cooling panels due to the effect of gravity. With a stratified tank for cold storage, up to 26 kWh/m^2 of cooling energy was generated in summer in Phoenix, Arizona. A low water flow rate was found to favor large temperature drops in the heat transfer fluid, while a high flow rate enhanced system cooling power, i.e., large temperature drops in the cold storage tank rather than the module. Therefore, it was recommended that for such systems, low flow rates be used during the daytime, and higher flow rates at night when cooling flux is used to charge thermal storage.

The electricity used to circulate the working fluid using a pump is of a higher quality than the

space cooling energy derived from the passive cooling system. For this reason, minimizing the electricity used in hybrid cooling systems is also important. Zhao et al. [179] experimentally demonstrated the feasibility of a thermosiphon module (Fig. 22e, f) for passive cold collection and delivery. The temperature difference in the cooling fluid gives rise to natural currents that drives the flow without additional energy input. Since the low flux density of daytime radiative coolers warrants low fluid flow rates, the use of such passive self-driven circulation for the working fluid is feasible. The close looped cycle was demonstrated to work even under low cooling fluxes that simulated cloudy/humid days. The cooling output may be scaled up by using serval thermosiphon modules.

5. Roof & Wall: Reflective Paint

Cool paints that demonstrates radiative cooling capability were mentioned in **Section 4.1.3**, yet their application typically is limited to roof, i.e. a surface that faces the sky (outer space), which serves as heat sink, to achieve satisfactory cooling performance. Additionally, application of radiative cooling paint on wall implies wagering on absorbing heat from terrestrial sources including those generated by human activities, attributed to the fact that radiative cooling paint possesses emissivity which is another critical characteristic of radiative cooling, thereby influencing the overall cooling performance, especially when employed to buildings that are in densely-built or populated cities. Besides, the majority of radiative cooling paints developed so far are whitish that are extreme glare, causing visual discomfort. Thus, reflective (cool) paints hold advantages over radiative cooling paint in reducing heat absorption from outdoor and extensive application area on both roof and exterior wall to reduce solar heat (radiation) absorbed by these envelopes. Herein introduces paints composed of three types of pigments: commercially available reflective pigments, synthetic IR-reflective pigments and thermochromic pigments. As the name suggests, reflectance dominates the behavior of how

reflective cool paints respond to incoming radiation. Reflectance of reflective paint is calculated using Equation (14) [180-183], which is not always the case for DPRCs,

$$R = \frac{\int_{\lambda_1}^{\lambda_2} r(\lambda) i(\lambda) d\lambda}{\int_{\lambda_1}^{\lambda_2} i(\lambda) d\lambda}, \quad (14)$$

where R represents the reflectance of material, λ defines the wavelength, $r(\lambda)$ is the spectral reflectance obtained from the UV-vis-NIR spectrophotometer, and $i(\lambda)$ is the standard solar spectral irradiance from ASTM standards. The waveband for calculations varies in the range of 250 nm $\leq \lambda \leq$ 2500 nm.

Thermal analysis was mainly conducted through three approaches: laboratory, field experiment and energy simulation under various conditions such as substrate types like concrete and aluminum plates, climates, orientation etc. Substrate coated with developed or conventional coating is placed on well-insulated box, which is made of foam or wood, or is simply irradiated without a box under an IR lamp at a distance of around 15-40 cm for about 15-60 min to obtain stabilized temperatures. Temperature can be measured at different locations: the outer/inner surface of (un)coated substrates, heat box and interior (top/center/bottom) of the box (Fig. 23a). Temperature profile of the samples is sometimes recorded to find the optimum temperature reduction. Some studies applied coatings on foam boxes with titled roofs (Fig. 23b) [182, 184, 185]. The optical properties of some coatings were imported into EnergyPlus to conduct energy simulation and the results were compared to reference cases.

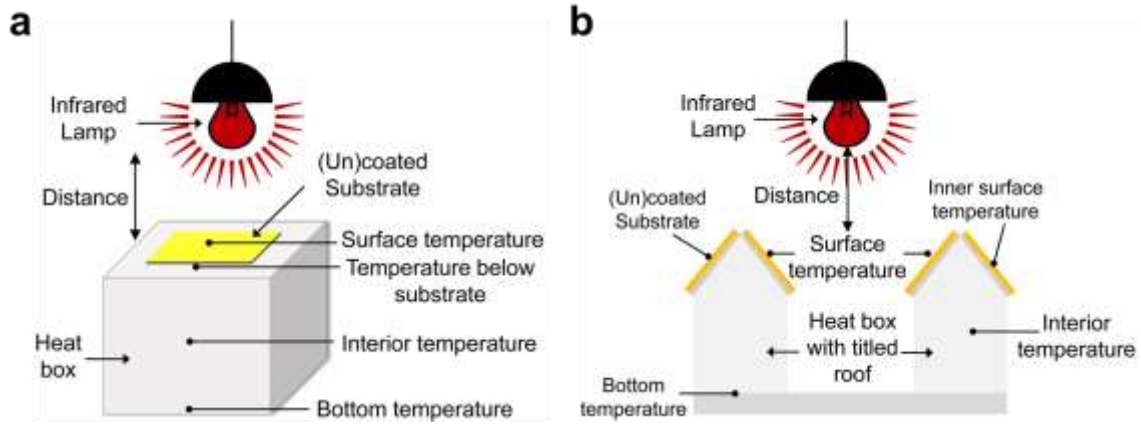

Fig. 23. Schematic diagrams of laboratory (indoor) experiment using heat box with a) flat and b) titled roofs.

5.1 Reflective Paint Materials

Paints are assembled by thoroughly dispersing pigments in binder with paint additives such as antifoaming agents and water etc., ensuring that the paints have preferable viscosity and stability for long-term storage. The well-blended paints will subsequently be daubed on substrates as coatings, as illustrated in Fig. 24a. The reflectance of coatings hinges upon (1) the optical properties of pigment and binder, (2) the size, shape and concentration of pigment particles and (3) the thickness of film [186]. Although the concentration of pigment, viz. relative ratio of pigment to medium, varies for different paints, pigments are responsible for reflectivity/scattering properties of the paints, thereby the cooling effect, as the other ingredients do not or hardly scatter [187].

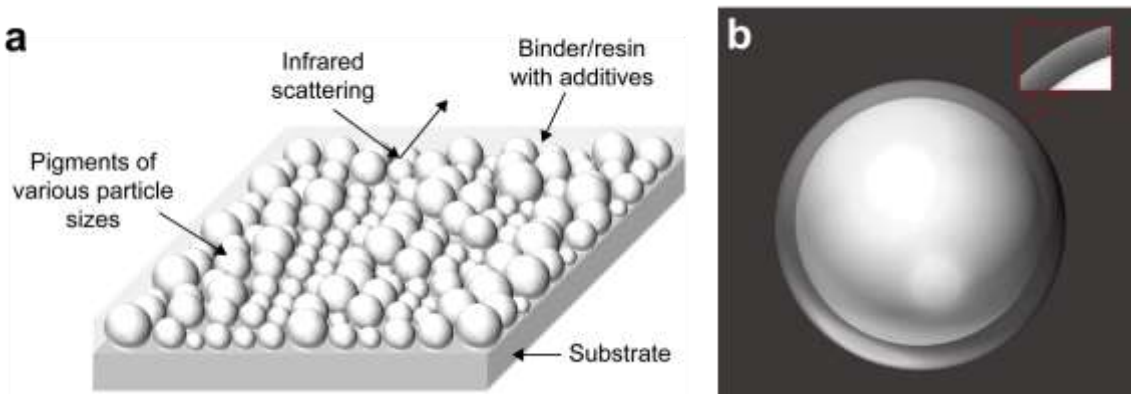

Fig. 24. a) Illustration of a substrate coated with white pigments dispersed in binder. b) Schematic diagram of hollow glass microsphere (HGM).

5.1.1. Retailed IR-reflective Pigment

Reflective cool paint can be fabricated using retailed white pigments without further modification as white color reflects nearly all incident solar radiation [188]. TiO_2 has been extensively employed as white pigment for decades in conventional paints [189-192], owing to its exceptional scattering properties. Many studies have proven that TiO_2 paints possess superior reflectivity in the visible and IR spectrums at around 90% or above [193, 194]. Moreover, hollow glass microspheres (HGMs) with high NIR reflectivity and thermal insulation, owning to their hollow structure (Fig. 24b), are often coated to form composite pigments [195]. Zhou et al. [191] prepared TiO_2 and HGMs coatings, which both exhibited NIR reflectance (R_{NIR}) of approximately 0.87. These two inexpensive particles with outstanding optothermal properties have been broadly utilized to formulate reflective paints/coatings for building walls and roofs [189-192]. Puesan and Mestre [189] coated four substrates with TiO_2/HGM white paint, of which two acted as vertical walls and the other two as roofs. The surface temperature of the substrates reduced by up to 5°C with the cool paint. Likewise, Wang et al. [193] fabricated an reflective cement paste by mixing dispersed TiO_2 emulsion. The cement paste showed R_{NIR} and R_{sol} of 0.867 and 0.67, respectively.

Some studies fabricated reflective paints in colors other than white using retailed IR-reflective pigments without further modification. In fact, the reflectivity of many retailed cool paints is realized by attaining lighter colors with the addition of white/TiO_2 pigment. Jiang et al. [196] prepared gray coatings with different pairs of high NIR-reflective pigments of complementary colors in blue, orange, yellow, violet (Fig. 25a, 1), green and red and TiO_2 rutile, according to the preparation method in a companion paper [197]. The gray coatings with various colors displayed R_{NIR} above 0.80 as disclosed in Fig. 25a, 2, implying the cooling effect of these coatings with wide range of color options. Xue et al. [198], who took a step further, fabricated a solar-reflective orange-gray paint with self-cleaning function. The R_{sol} and R_{NIR} of the orange-gray coating were 0.815 and 0.846, respectively (Fig. 25b). Of particular relevance, Yang et al. [199] synthetized a solar reflective blue-grey coating with yellow-green luminescence. The R_{sol} and R_{NIR} of the coating were 0.808 and 0.853, respectively. The coating could emit constant glow of yellow-green light at night (in the dark) for around 2 hours after being exposed to sun radiation and gradually faded.

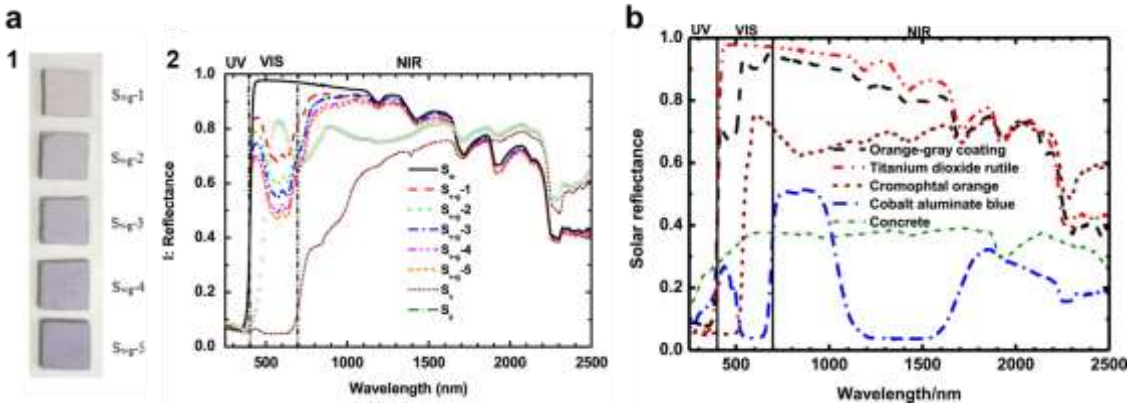

Fig. 25. a) (1) Optical images of the violet-gray coatings with white basecoats, and (2) spectral reflectance curves of white, yellow, violet coatings and cool violet-gray coatings at different colored pigments concentration with white basecoats [196]. b) Spectral reflectance curves of the orange-gray coating over white basecoat [198]. (For interpretation of the

references in colors in this figure, the reader is referred to the web version of this article.)

5.1.2. Synthetic IR-reflective Pigments

Majority of retailed cool paints uses white pigment that endows paints with top-tier IR-reflectance, yet it may cause visual discomfort, and hence synthetic of cool pigment in other colors are sought after. Moreover, although cool paints can be easily formulated with retailed IR-reflective pigments (**Section 5.1.1**), the reflectivity of pigments can be further enhanced by modification in terms of fabrication process and dopant, and the presence of topographical structure. IR-reflective pigments are complex inorganic color pigments, which reflect wavelengths in the IR-region for coolness, along with some visible light selectively, and thus they come in various colors [11, 200, 201]. Many research synthesized IR-reflective pigments (including but not limited to white color) using pigments alternative to TiO_2, for instance, $BaTi_5O_{11}$, bismuth vanadate ($BiVO_4$) [202, 203], $YMnO_3$ [204], $Y_2Ce_2O_7$ [205], to broaden the availability of reflective paints with improved IR-reflectance and customizable color options. For the most part, metal oxides of metals such as cerium, aluminum, titanium and tungsten, serve as dopants to regulate the reflectivity of primary materials and/or as IR-reflective materials alone in many reflective paints. Further, the use of pigments that contain toxic heavy metals like cobalt and lead are rigidly restricted due to adverse environmental effects [190]. These metals are substituted with others in many studies, reducing the concentration of toxic metals to composite more eco-friendly pigments [203, 206-209]. Rare-earth (RE) elements, for instance, terbium (Tb), molybdenum (Mo), and praseodymium (Pr), serve as alternatives to enhance IR-reflectivity and possess low toxicities, while providing color diversities [180, 207]. Pigments can be synthesized by diverse processes, in particular, solid-state, citrate-gel, and sol-gel, which affect the properties of pigments. Chemical and physical properties by means of chemical composition, particle size (distribution) and shape, and stability properties etc. are of

particular significance in selecting the suitable pigments for application [188, 192]. Pigments always undergo calcination by being strongly heated at high temperatures, of about 500-1500°C, where metal ions rearrange, and volatile substances are removed to form new and more stable crystal structures, improving the stability properties of the synthetized pigments and pigmented coatings. Most of the developed pigments included in this review were grounded and endured calcination to obtain milled pigments with uniformly distributed sizes and regular shapes.

Mie's theory and Kubelka-Munk model are two approaches that are applied to analyze how pigments interact with light [186]. Mie's theory is the microscopic approach employed when spherical particles are separated at distances that are large compared to the wavelength. On the other hand, Kubelka-Munk model is the macroscopic approach that describe how light is diffused through the particles by parameterizing the rates at which the particles absorb and backscatter light. Many researches have suggested the theoretical particle size to be greater than half of the wavelength reflected [187, 200]. Thus, for sufficient reflectiveness in the 700-1100 nm waveband, where the energy of solar radiation predominantly concentrates [200, 210], IR-reflective pigments should have average diameter about or larger than 350-550 nm (0.35-0.55 μm) [186, 192, 200] or 0.35-1.25 μm if considering the waveband of 700-2500 nm. Majority of the reviewed synthetic pigments had mean particle (grain) size larger than 0.55 μm, albeit some having smaller sizes, for instance, nano-pigments, which were also found to be highly IR-reflective. This could be attributed to the different fabrication methods used and hence the theoretical size range might not be applicable for each case. Additionally, pigments comprised of (dopant-coated) HGMs had relatively larger sizes as retailed HGMs normally have the size of 2-85 μm [195, 211]. Furthermore, if the topographical surfaces of the pigments were modified at micro-/nanoscale for hydrophobicity, the size tends to be bigger than 0.55 μm.

As chemical and coloristic properties that are affected by the synthetic method used are beyond the scope of this review, the color appearance mentioned is provided by the reference articles and the crystalline structures/composition would not be discussed. The synthetic IR-reflective pigments are categorized according to their colors: (1) white and black, (2) colored (yellow, green and blue), and (3) multi-colored, regardless of chemical composition, synthesis process and physicochemical properties.

5.1.2.1. White and Black colors

Gao et al. [212] synthesized white NIR-reflective coatings with bismuth nitrate pentahydrate ($BiOCl_xBr_{1-x}$) microflower that could be fabricated on various building materials. Each microflower is formed of numerous nanosheets with thickness of around 100 nm stretching out of the center, contributing to 3D hierarchical structure (Fig. 26a). $BiOCl_{0.875}Br_{0.125}$ with chlorine content of 0.875 showed the highest R_{NIR} of 0.935 and reduced the interior temperature of box by 3.9°C, compared to an uncoated box. Lu et al. [213] composited reflective white pigments with R_{NIR} of 94.5%-95.7% and total solar reflectance (TSR) of 95.6%-97.2% by depositing ZnO at different concentrations. As depicted in Fig. 26b, the concentration of Zn^{2+} affects the hydrolysis rate of $ZnCl_2$, forming different amounts of ZnO nuclei crystals, thereby leading to different morphologies: nanosheets (Fig. 26c, 1), nanoplates or nanoparticles (Fig. 26c, 2), on the surface of HGMs. The formation of different morphologies could be ascribed to heterogeneous nucleation that took place in the precursor solutions when ZnO seed nuclei was formed on the HGMs' surfaces. With the HGM/ZnO composite white coating, the outer surface temperature of the heat box decreased by 11.1°C [213]. Moreover, Lv et al. [14] performed an outdoor assessment on a sunny day in Riverside, California in 2018 summer using their self-developed $ZnTiO_3$ pigment with solar absorptance of 0.115. The lowest surface temperatures of $ZnTiO_3$-coated and ZnO-coated aluminum plates were 14.9°C and 10.3°C lower than the

roof temperature (70.1°C). The developed $ZnTiO_3$ coating had improved cooling effect than common white paint. Compared to white coatings, standard black coatings, which are formulated using carbon black pigments, have much lower R_{sol} of approximately 5% [214, 215]. However, Ma et al. [204] developed black Fe-doped orthorhombic $YMnO_3$ black pigments via molten salt synthesis and coatings using yttria sol as binder. The reflectance of the coating with MnO_2/Fe_2O_3 molar ratio of 85:7.5 at 2200 nm was approximately 75%, manifesting high R_{sol} for cooling application as a black paint.

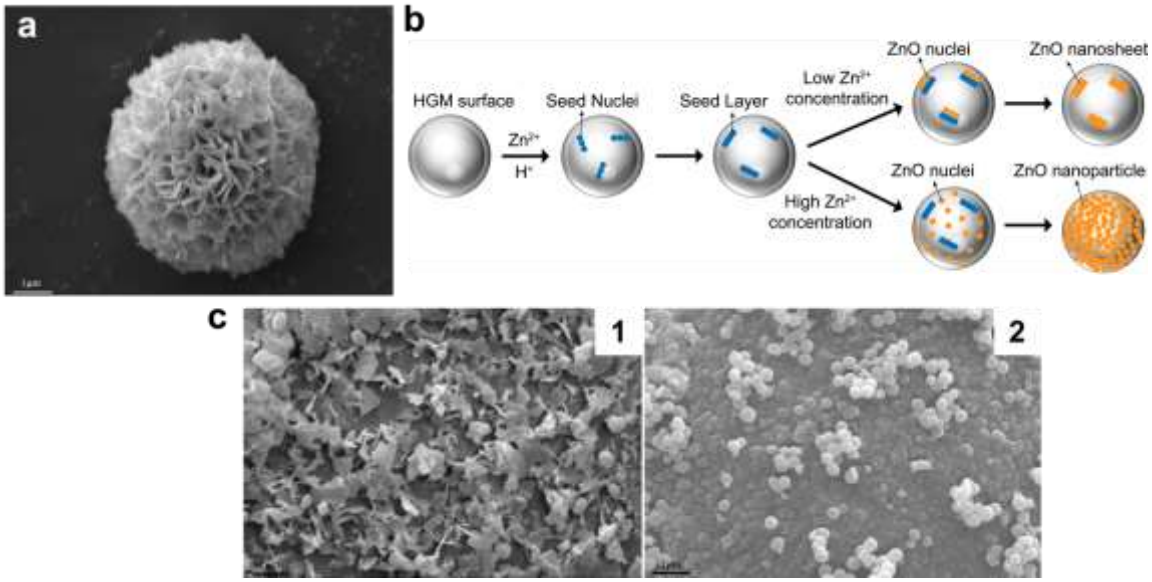

Fig. 26. a) SEM images of $BiOCl_{0.875}Br_{0.125}$ [212]. b) Schematic illustration of the possible formation process for ZnO nanostructures with different morphologies on HGM surfaces. c) SEM images of ZnO film with zinc nitrate concentrations of (1) 0.025 mol/L and (2) 0.05 mol/L [213].

5.1.2.2. Colored (yellow, green and blue)

Raj et al. [216] synthesized terbium (Tb)-doped Sr_2MO_4 pigments, of formula $Sr_2M_{1-x}Tb_xO_4$ (M=Sn or Zr; x=0-0.4), in bright yellow appearance (Fig. 27a). The pigments and the pigmented coating (Tb content=0.4) exhibited R_{NIR} of 89.2%-96.4% and 81.6% (Zr-doped),

respectively. The R_{NIR} and R_{sol} of another yellow NIR-reflective pigment, Ni-doped $BaTi_5O_{11}$ fabricated by Zou and Zhang [217] were up to 97.72% and 94.08%, respectively, with 5 wt% Ni-doping content. The ceramic tiles with the Ni-doped $BaTi_5O_{11}$ coating demonstrated outstanding cooling of 10.3°C compared to PU-coated tiles. Instead of doping, Sameera et al. [218] obtained nanostructured zinc aluminate, $ZnAl_2O_4$, with R_{NIR} of 80%-86% (Fig. 27b) by citrate sol-gel method and subsequent annealing at different temperatures. The concrete with $ZnAl_2O_4$ coating (pigments annealed at 1100°C) demonstrated a slightly higher R_{NIR} of 90% compared to that with TiO_2 coating (87%). Moreover, another cost-effective complex pigment, $BiVO_4$, which is a group of brilliant greenish yellow pigments with higher chroma than iron yellow (one of the common yellow pigments) [192], was used to composite $BiVO_4$-ZnO by Thejus and Nishanth [202]. The R_{NIR} of $BiVO_4$-ZnO was above 90% regardless of $BiVO_4$ content. The pigmented coatings (25 wt% $BiVO_4$) showed R_{sol} of 75.31% and lowered the surface temperature of aluminum sheets by 8.4°C than that with commercial yellow paints [202].

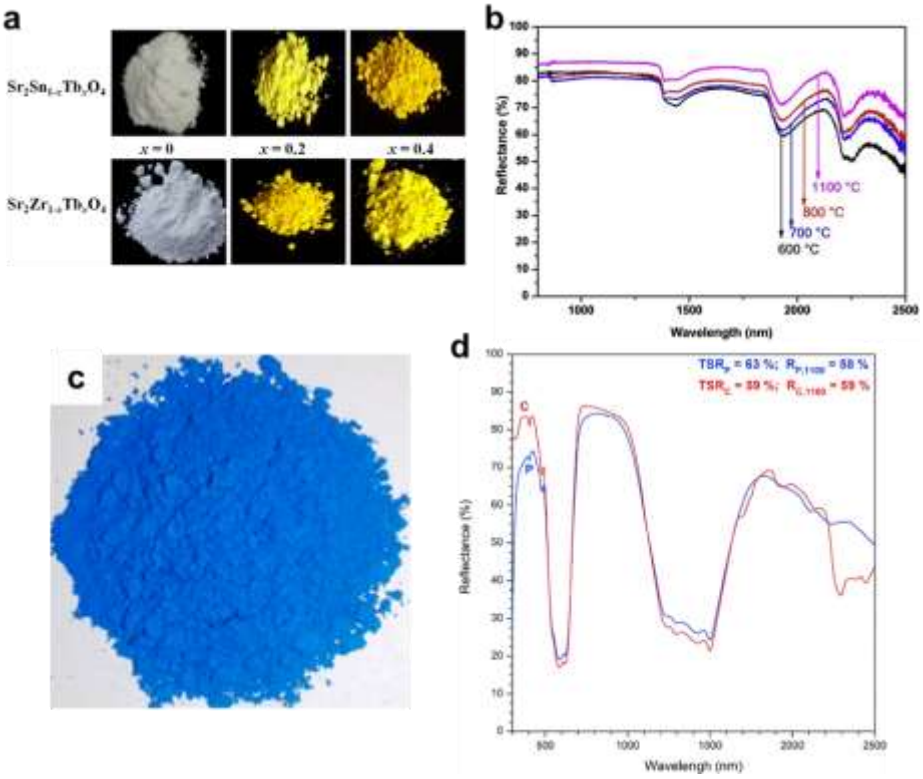

Fig. 27. a) Images of $Sr_2M_{1-x}Tb_xO_4$ (Mn = Sn or Zr; x=0, 0.2 and 0.4) yellow pigments [216]. b) NIR-reflectance spectra of $ZnAl_2O_4$ samples annealed at different temperatures [218]. c) Image of synthesized blue nano-pigments, $Yin_{0.9}Mn_{0.1}O_3$-ZnO calcined at 850°C [219]. d) Diffuse reflectance spectra of pigment (P) and prepared coating (C) [220]. (For interpretation of the references in colors in this figure, the reader is referred to the web version of this article.)

Liang et al. [221] reported that their yellowish-green, Ti-doped Cr_2O_3 pigments with R_{NIR} of 84.04%-91.25% are more reflective than green pigment, pure Cr_2O_3 (50%). Additionally, Jose et al. [222] synthesized green Y_2BaCuO_5 pigments by two different methods: nano-emulsion and solid-state methods. The average R_{NIR} of the pigments synthesized by solid-state was 58%, which is lower than that of pigment fabricated by nano-emulsion method (74%). The same lead author proposed another nano-pigment, $Yin_{0.9}Mn_{0.1}O_3$-ZnO by sol-gel combustion and pigmented coatings with R_{NIR} of 70% and 67%, respectively, and demonstrated intense blue color (Fig. 27c) [219]. Ianoş et al. [220] synthetized Co-doped $ZnAl_2O_4$ blue pigments by combustion synthesis and pigmented coatings that exhibited TSR of 63% and 59%, respectively (Fig. 27d). The surface temperature of the $Zn_{0.9}Co_{0.1}Al_2O_4$-coated sample was 16°C lower and 9°C higher than carbon-black-coated and white TiO_2-coated samples, respectively. Jing et al. [207] composited $Sr_{1-x}RE_xCuSi_4O_{10+\delta}$ pigments (x=0-0.5) with intense blue color by doping three RE elements: Pr, neodymium (Nd), and samarium (Sm). The synthetized pigments showed R_{NIR} of approximate 70% (depending on the dopant and doping content), which is impressively higher than ordinary cobalt blue pigments (29%) [223].

5.1.2.3. Multi-colored

The previous two sections discussed synthetic pigments, whose color diversity due to doping concentration is not obvious to bare eyes. In fact, the dopant and doping content used can induce variation in IR-reflectance and color appearance (visible reflectance) of synthetic pigments/coatings in terms of hues (pure color), tints (hue + white), tones (hue + grey) and shades (hue + black) (Fig. 28a).

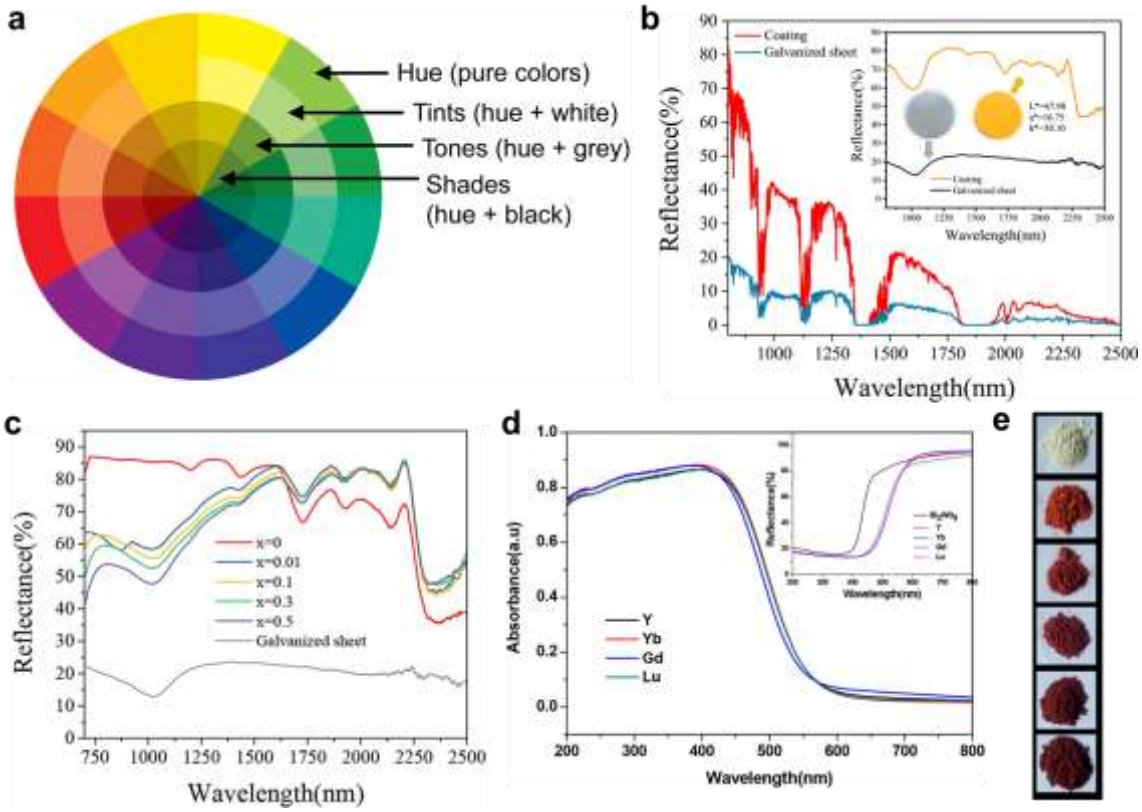

Fig. 28. a) Color wheel. b) NIR solar reflectance spectra of bare galvanized sheet and $La_2Ce_{1.7}W_{0.15}Fe_{0.15}O_{7+\delta}$ pigmented coating (inserted) [224]. c) NIR reflectance spectra of the $La_2Ce_{2-x}Tb_xO_7$ (x = 0-0.5) [180]. d) NIR reflectance spectra of $Bi_{1.7}RE_{0.3}W_{0.7}Mo_{0.3}O_6$ (RE = Y, Yb, Gd, Lu) pigments [225]. e) Photographs of $Y_2Ce_{2-x}Tb_xO_7$ (x = 0, 0.2, 0.4, 0.6, 0.8 and 1.0, from top to bottom) red pigments, respectively [226]. (For interpretation of the references in colors in this figure, the reader is referred to the web version of this article.)

Zhou et al. [227] prepared Fe-doped $La_2W_2O_9$ pigments, of formula, $La_2W_{2-x}Fe_xO_{9-\delta}$ (x=0-0.2) by solution combustion synthesis. The colour varied from white to orange with increasing Fe content. Through the energy simulation conducted, the $La_2W_{1.8}Fe_{0.2}O_{9-\delta}$ coating with R_{NIR} of 86.21% could reduce the average roof temperature by 5.15°C, compared to that of cement roof. Additionally, the energy consumption and electricity cost of the model with $La_2W_{1.8}Fe_{0.2}O_{9-\delta}$-coated exterior wall reduced by 1.07 kWh/m^2 and $7.32/month, respectively, proving its feasibility as reflective paint for building energy saving. Pechini process, which is an alternative approach to the sol-gel method, was used by Chen et al. [224] to synthesize Fe and W co-doped lanthanum cerium oxide pigments, of formula $La_2Ce_{2-x}W_{0.5x}Fe_{0.5x}O_{7+\delta}$ (x=0.1-0.9) with yellow to orange colors. The powders were obtained by subsequent calcination at three different temperatures, resulting in different reflectance, among which R_{NIR} reached 89.55% when calcined at 1150°C. The R_{NIR} of the $La_2Ce_{0.7}W_{0.15}Fe_{0.15}O_{7+\delta}$ (x=0.3, calcined at 1150°C) coating was approximately 71.01%, as shown in Fig. 28b. Similarly, Bae et al. [228] obtained orange perovskite pigments, $Sr_4Mr_2(Cu_{1-x}Zn_x)O_9$ (x=0-1) with high R_{NIR} of 83.03% after calcination at 1000°C. The color of the pigments tends to brown as the doping content increases to 1. Elakkiya et al. [229] reported three pigments: Ce-doped gahnite, Fe-doped gahnite, and Ce- and Fe-doped gahnite of formulas: $ZnAl_{2-x}Ce_xO_4$ (x=0-0.04), $ZnAl_{2-y}Fe_yO_4$ (y=0-0.5) and $ZnAl_{2-x-y}Ce_xFe_yO_4$ (x=0-0.04, y=0-0.5), respectively, by citrate sol-gel method. The colors of the pigments ranged from mild yellow to brown. The Ce-doped gahnite and Ce- and Fe-doped gahnite demonstrated high R_{NIR} of 86% and 80%, respectively.

Moreover, the Pr/Tb-doped $La_2Ce_2O_7$ pigments and coatings, which were prepared by Huang et al. [180] via sol-gel method, revealed R_{NIR} and R_{sol} of above 95% and 65%, respectively. The pigmented coatings significantly increased the reflectance of bare substrates, as illustrated in Fig. 28c, (R_{NIR}: 20.11%, R_{sol}: 19.18%), providing cooling effect. The color varied from light yellow to dark orange with increasing dopant content. Additionally, Huang et al. [225]

synthetized $Bi_{1.7}RE_{0.3}W_{0.7}Mo_{0.3}O_6$ pigments, where four RE elements: yttrium (Y), ytterbium (Yb), gadolinium (Gd), and lutetium (Lu) were chosen as dopants. All pigments displayed outstanding R_{NIR} of above 95% and the substrates with $Bi_{1.7}Lu_{0.3}W_{0.7}Mo_{0.3}O_6$ pigmented coatings reflected about 80% of NIR-radiation (Fig. 28d). The color changed from faint yellow to brilliant yellow-orange with the addition of dopant. Similarly, Schildhammer et al. [230] composited NIR-reflective $RE_6Mo_2O_{15}$ (RE = Tb, Dy, Ho, Er) pigments with varied colors (depending on dopant). Among these, Alexandrite effect, which introduces the change of visual color of materials due to different illuminant sources, was discovered on Er-/Ho-doped pigments, whose colors were orange/yellow depending on the light source. These pigments could provide aesthetic and unique appearance, while reducing heat penetration into buildings through walls.

Besides, Raj et al. [226] reported Tb-doped yttrium cerate, of formula $Y_2Ce_{2-x}Tb_xO_7$ (x=0-1) pigments and coatings with R_{NIR} of 55.1%-86.9% and 70.1% (x=0.2, concrete slab with TiO_2 basecoat), respectively. The color differed from white to red-brown with raising Tb content (Fig. 28e). Yang et al. [231] prepared (1) Fe-doped (FN) and (2) Fe and N doped (FNM) $MgTiO_3$ pigments, by sol-gel method and ammonolysis, respectively and achieved R_{NIR} of 53.51-88.58%. The authors also discovered that the surface temperature of substrates and interior temperature coated with FNM coating (x=0.3) decreased by 2.4°C and 2°C, respectively. Gao et al. [181] coated $BiOCl_{1-x}I_x$ (x=0-1) on surfaces of HGMs by chemical liquid deposition method and the color ranged from white to red with increasing iodine content. The HGM/$BiOCl_{1-x}I_x$ composited pigments exhibited incredible R_{NIR} of 92.6%-94.7%. The surface/interior temperature of the heat box reduced by up to 8°C with HGM/$BiOCl_{0.75}I_{0.25}$ compared to uncoated surface, which could be attributed to HGM/$BiOCl_{0.75}I_{0.25}$ having the highest R_{NIR}. Chen et al. [232] fabricated Fe-/Tb-doped Bi_3YO_6 pigments, of formula $Bi_{3-x}Fe_xYO_6$ (x=0-0.8) and $Bi_3Y_{1-x}Tb_xO_{6+\delta}$ (x=0-0.5) and coatings with (1) no dopant, (2) Fe

content of 0.4 and (3) Tb content of 0.05. The colors of pigments varied from light-yellow to deep red with increasing Fe content and from yellow to dark yellow with increasing Tb content. The R_{NIR} of Fe-doped and Tb-doped pigments were 53.87%-99.58% and 88.64%-99.87%, respectively. The surface temperatures of substrates coated with $Bi_{2.6}Fe_{0.4}YO_6$ and Bi_3YO_6 coating were 5°C or 20°C lower than those with conventional yellow coating (iron oxide), respectively.

Besides yellow and red hues, purple and blue colors are favorable to meet aesthetic needs. Thejus et al. [223] prepared Co-doped $LiZnPO_4$ pigments, of formula $LiZn_{1-x}Co_xPO_4$ (x=0.1-0.8) with colors varying from purple to violet with increasing Co content (Fig. 29a) and $LiZn_{0.9}Co_{0.1}PO_4$ coatings. The pigments demonstrated R_{NIR} of 29.58%-68.04%, which is much higher than that of conventional cobalt blue pigments (29%). Furthermore, Thejus et al. [233] synthesized Co-doped $NaZnPO_4$ pigments, of formula $NaZn_{1-x}Co_xPO_4$ (x=0-0.2). The color changed from blue to navy blue with increasing Co content. The R_{NIR} of the pigments and $NaZn_{0.9}Co_{0.1}PO_4$ coating ranged from 52%-87% and above 60%, respectively, on different substrates (Fig. 29b). The interior and surface temperature of foam box and substrates coated with $NaZn_{0.9}Co_{0.1}PO_4$ coating decreased by ~4-4.5°C (Fig. 29c).

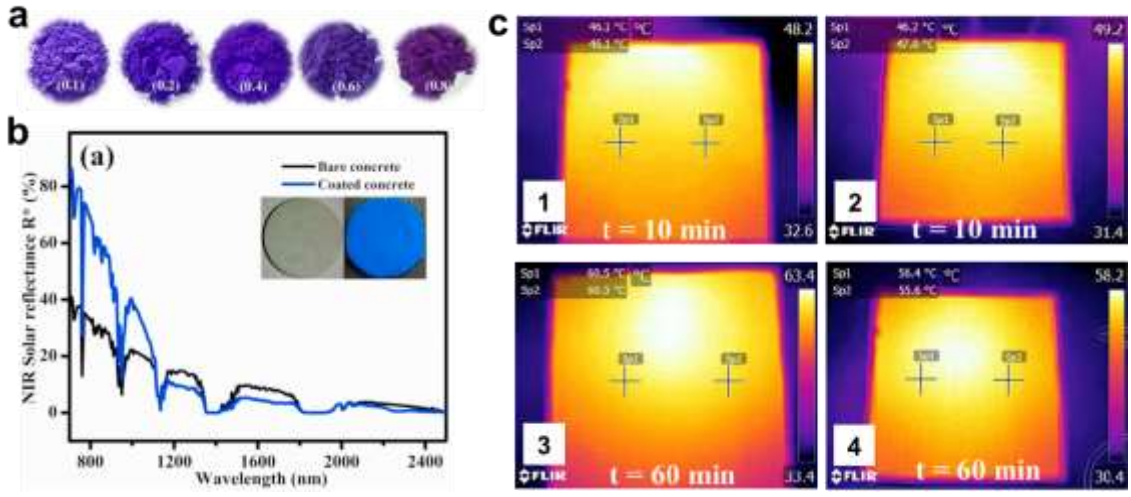

Fig. 29. a) Photos of $LiZn_{1-x}Co_xPO_4$ (x=0-0.8) pigments [223]. b) NIR solar reflectance

spectra of bare concrete and concrete coated with $NaZn_{0.9}Co_{0.1}PO_4$ coating (images of substrates inserted); c) Thermal images of (1, 3) $CoAl_2O_4$ coating and (2, 4) $NaZn_{0.9}Co_{0.1}PO_4$ coating after 10 and 60 mins of IR-lamp exposure [233]. (For interpretation of the references in colors in this figure, the reader is referred to the web version of this article.)

Thermal analyses of the reviewed paints with synthetic IR-reflective pigments were generally examined by laboratory (indoor) experiment as introduced in the beginning of Section 5, while several researches carried out field tests and simulation analysis, as demonstrated in Fig. 30. Although the reference used for comparison varies in different researches, uncoated substrates and conventional color-match paints were normally utilized as reference. In some cases, white TiO_2 and carbon-black paints were used as baselines to obtain a general picture of the cooling performance of the developed reflective paints. For instance, no. 8 and 9 in Fig. 30 show two temperature differences of the same substrate's surface that is coated with cool blue reflective paint that was 16°C lower (the former) and 9°C (the latter) higher than carbo-black-coated and white TiO_2-coated samples, respectively. Overall, the reviewed paints with synthetic IR-reflective pigments performed average cooling effect of ~10°C with several that exceeds 10°C, demonstrating their potential as cool building façade to reduce solar heat gain.

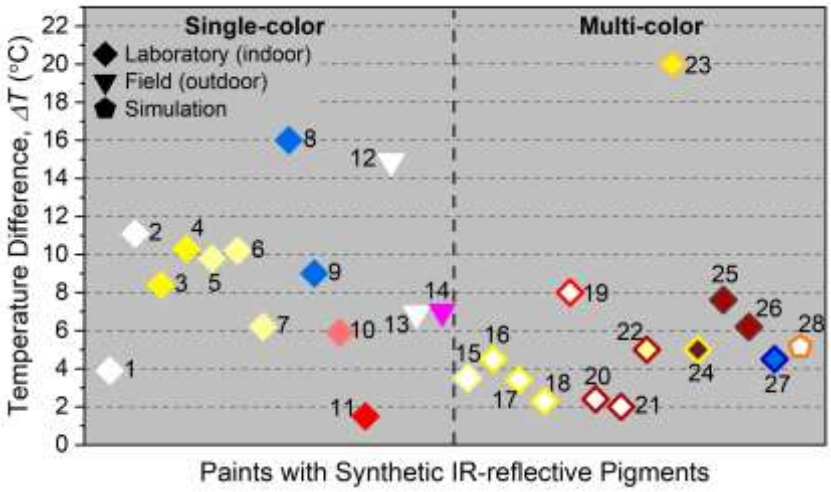

Fig. 30. Temperature difference of substrates' surfaces coated with synthetic IR-reflective pigments or interior air temperature of heat box, compared with references. For multi-color pigments, the fill and border colors represent the color of pigment when the dopant content is lowest and highest, respectively. Paints with synthetic IR-reflective pigments from literature labeled (in no particular order) as follows: (1) [212], (2) [213], (3) [202], (4) [217], (5) [210], (6, 7) [234], (8, 9) [220], (10) [210], (11) [235], (12) [14], (13) [236], (14) [237], (15) [205], (16) [185], (17, 18) [238], (19) [181], (20, 21) [231], (22, 23) [232], (24) [182], (25, 26) [184], (27) [233], and (28) [227]. (For interpretation of the references in colors in this figure, the reader is referred to the web version of this article.)

5.1.3. Thermochromic Pigments

Thermochromic pigment (TP) is colored to maintain thermal comfort by absorbing incoming radiation when the ambient temperature is below T_c (in winter) and becomes colorless (in summer), as shown in Fig. 31, to reduce thermal transfer by reflecting incident radiation at temperatures above T_c. This allows thermochromic coating (TC) to possess thermal management for both cooling and heating periods, thereby further enhancing its energy saving potential throughout the year.

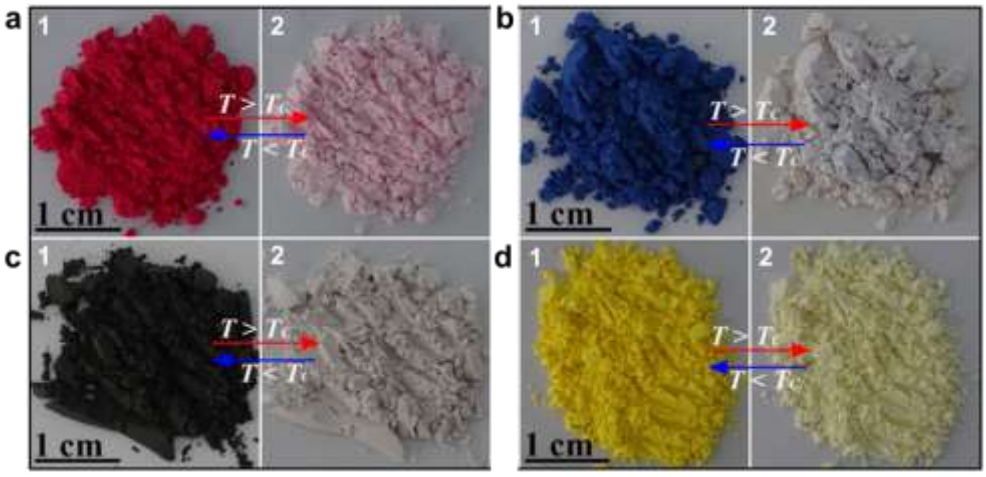

Fig. 31. Photographs of four TPs at different temperatures: a) red; b) blue; c) black; d) yellow

in (1) colored state (at 10°C) and (2) colorless state (at 37°C), respectively [239]. The T_c of these TPs was in the range of 28-31°C. (For interpretation of the references in colors in this figure, the reader is referred to the web version of this article.)

Zhang and Zhai [240] conducted spectral and thermal analyses of TCs in five colors with two different concentrations of TiO_2 and TPs. The R_{sol} of these coatings in colored and colorless phases varied from 0.40-0.70 and 0.54-0.82, respectively. Under three different weather conditions: warm, cool and nocturnal, in April 2018 in Shanghai, China, as shown in Fig. 32a, the TCs (in five colors) revealed cooler surface temperatures., compared to conventional paints. Of particular relevance, Yuxuan et al. [241] simulated the energy usage of a 2-story office building with TCs-applied exterior walls and roof in cities with different climate zones in China using EnergyPlus (Fig. 32b, 1). From the simulation, the TCs managed to reduce the annual energy consumption by 4.28-5.02 kWh/m^2 with respect to common coating (Fig. 32b, 2).

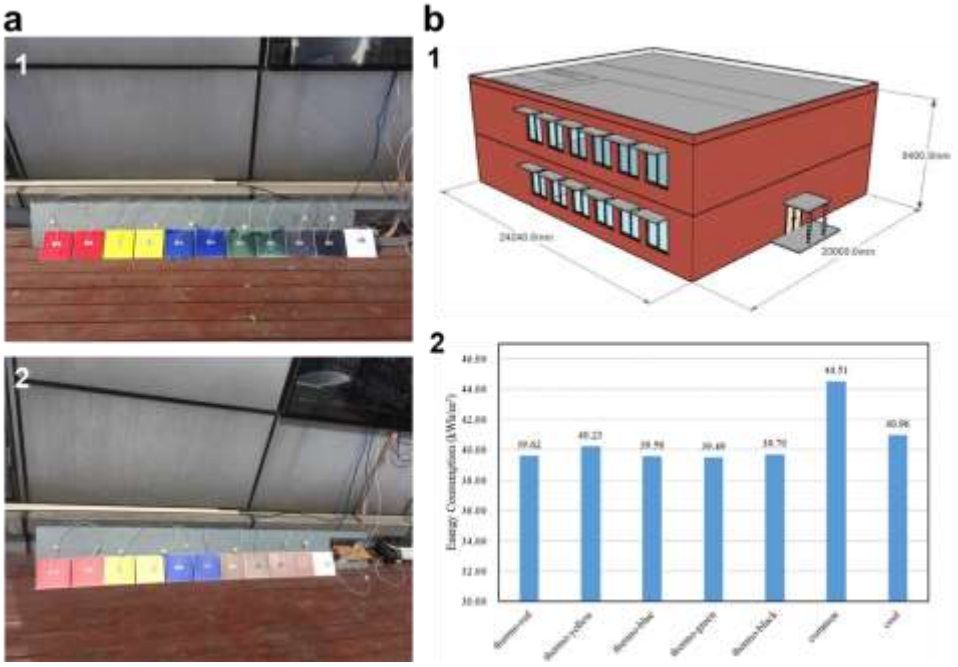

Fig. 32. a) Field investigation on temperature reduction of thermochromic coatings in (1) colored and (2) colorless phases [240]. b) (1) Office building model for EnergyPlus

simulation and (2) total energy consumption per square meter of the building with different coatings [241]. (For interpretation of the references in colors in this figure, the reader is referred to the web version of this article.)

Moreover, Berardi et al. [242] formulated TCs using four TPs (at three different concentrations) in red (from two different companies), black and magenta colors with high concentration of TiO_2 and different T_c. The R_{sol} in the colored and colorless states was 60%-75% and 80%-86%, respectively, showing excellent solar reflectivity. The cooling effect of these four TCs was assessed by EnergyPlus simulation using an office model in Toronto, Canada relative to common coatings. With TCs, the peak temperature reduced by about 25°C on the roof and 15°C-20°C on the facades, depending on the orientation of the wall. Further, Liu et al. [243] simulated the performance of buildings in four cities of China using EnergyPlus. As illustrated in Fig. 33a, the total energy performance of buildings with the TCs (in four colors) was less than those with cement coating. Cheng et al. [239] reported that the total energy consumption of buildings with facades coated with their developed TP/PDMS coatings (in four colors) were close to the buildings with TiO_2/PDMS coatings (Fig. 33b). This implies the cooling potential of TCs is comparable to conventional white cool paints to achieve energy savings.

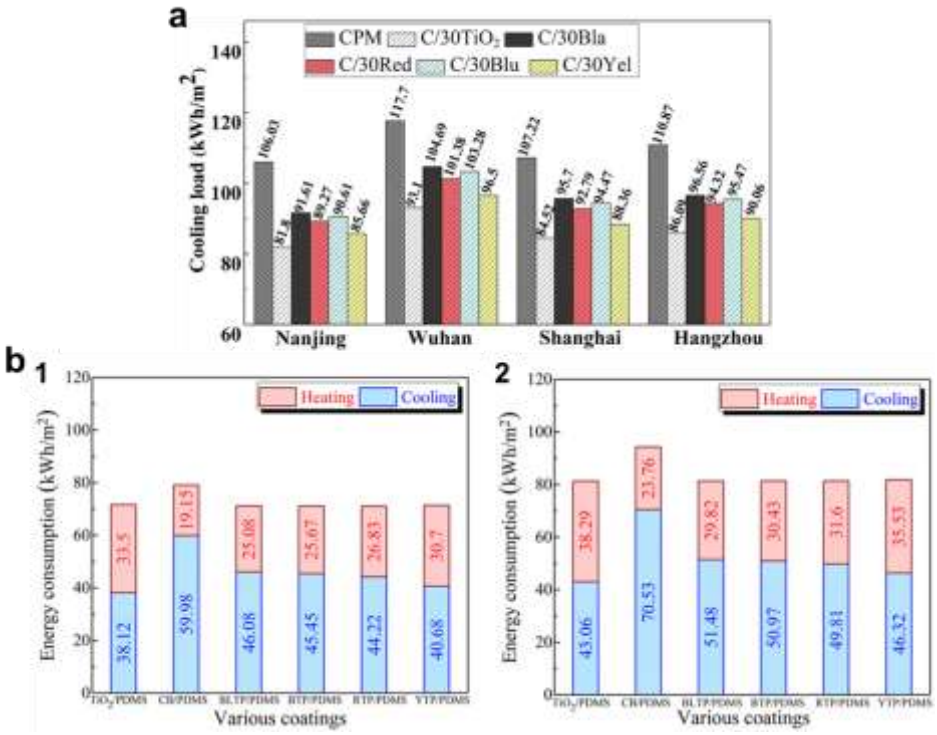

Fig. 33. a) Cooling load of building with various types of coatings in four cities in China [243]. CPM: Portland cement gray paint, C/30TiO_2: TiO_2 white coating, C/30Bla/Red/Blu/Yel: TC with 3g of black/red/blue/yellow TPs. b) Energy consumption of building model with different coatings in (1) Shanghai and (2) Wuhan, China [239]. CB/PDMS: carbon black/PDMS coating, BLTP/BTP/RTP/YTP/PDMS: PDMS coatings with TPs in blue/black/red/yellow.

5.2. Comparison of Reviewed Reflective Paints/Pigments

5.2.1. Spectral Properties of Reviewed Reflective Paints/Pigments

Thermochromic pigments and TiO_2 are representatives of commercially available pigments that provides paints with cooling potential. For thermochromic pigments, which undergo discoloration due to temperature variation, the reflectance also changes between colored and colorless states, depending on the ambient/surface temperature (as shown in Fig. 34a). The variation of average solar reflectance ranges from 0.7% to 77.7%. Pigments with darker color

like green, blue and black revealed much higher variation in reflectance than that of lighter color pigments (e.g., yellow) and could reach as high as approximately 77%, as demonstrated in Fig. 31 and 34a. This could be attributed to the diversity in the reversible molecular structure of the pigments and the degree of changes in reflectance due to temperature variation. This unique property allows thermochromic paints to fulfill aesthetics needs, while offering energy saving in buildings.

Synthetic pigments have demonstrated extraordinary NIR-/solar-reflectance of approximately 80% or above (varied depending on pigments), as illustrated in Fig. 34b, which renders the paints with cooling application in various colors. They are found to be more IR-reflective compared with conventional color-matched pigments, suggesting their feasibility in reducing incident solar heat gain. In particular, pigments in white and yellow hues are outstandingly more reflective than other hues (see inserted of Fig. 34b). In many cases, the introduction of TiO_2, which acts as a reflectance enhancement medium, guarantees the reflectivity of synthetized pigments/paints. Moreover, the selection of dopant and the dopant concentration play key roles in multiple factors, such as the structural formation, crystallite size, morphology, particle size etc., thereby affecting the spectral properties. In this paper, for multi-colored synthetic pigment, whose color changes by changing the concentration of the same dopant, while using the same parent material, the variation of NIR-/solar-reflectance of the pigments can range from less than 10% to approximately 40% or above, as depicted in Fig. 34c. This could be ascribed to chemical substitution between the parent material and the dopant. For the most part, increasing dopant concentration reduces the IR-reflectance. Thus, the dopant and dopant concentration for synthesizing reflective pigment need to be carefully considered. Table 6 summarizes the recent research on IR-reflective pigments/paints with various properties in detail.

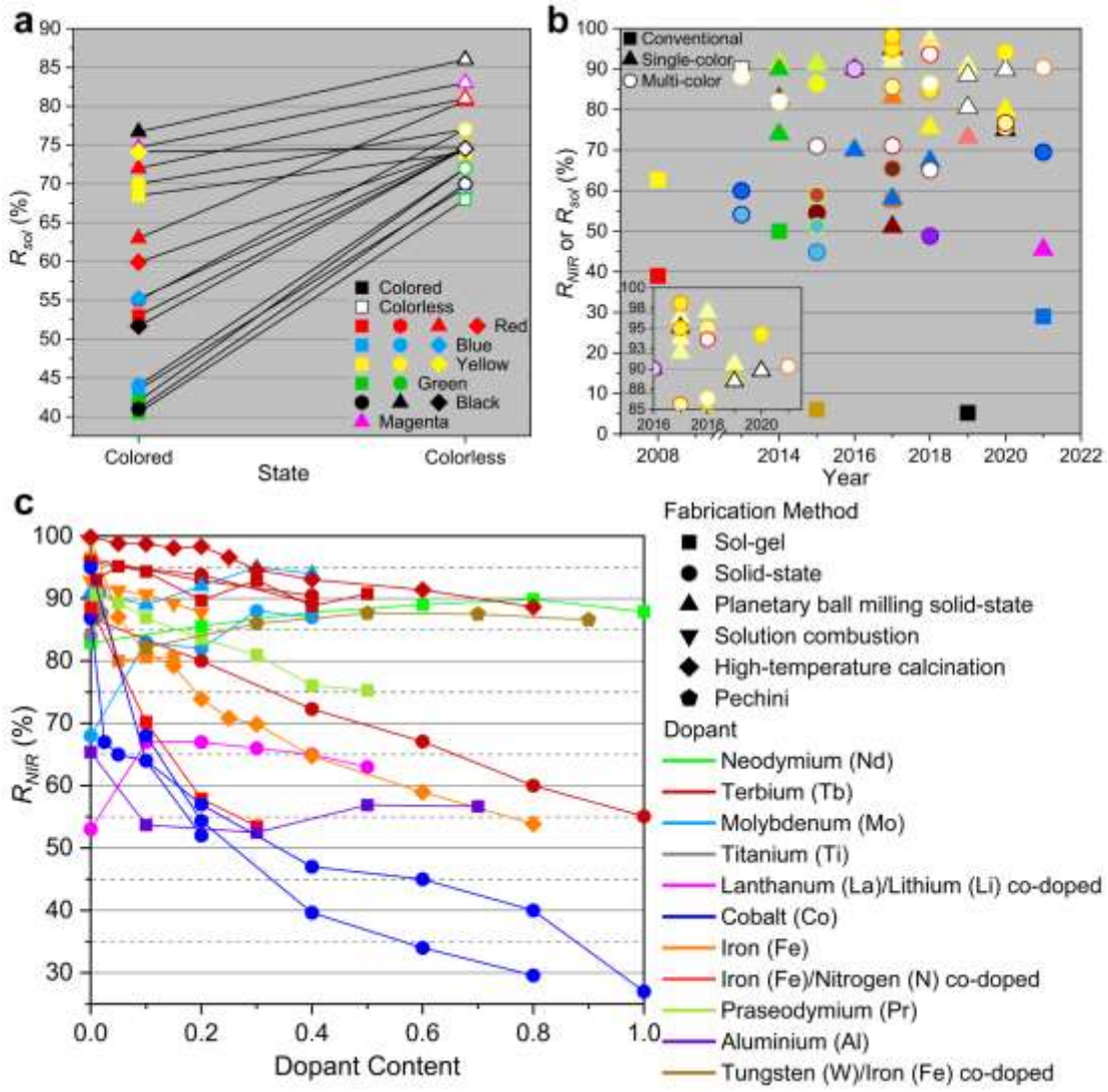

Fig. 34. a) Average solar-reflectance of thermochromic paints reviewed in this paper. Thermochromic paints from literature (in no particular order) are labelled as follows: Square: [240], circle: [241], triangle: [242], and diamond: [243]. b) Average NIR-reflectance or solar-reflectance of pigments against the year of publication. Square: conventional pigment, triangle: single-color, synthetic pigment in single-color and dot: multi-color synthetic pigment. For multi-color pigment (dot), the fill color and the border color represent the color of pigment when the dopant content is lowest and highest, respectively. c) Variation of NIR-reflectance with respect to dopant used and the content of dopant. (For interpretation of the references in colors in this figure, the reader is referred to the web version of this article.)

Apart from the dopant concentration, the effect of concentration/mass fractions of reflective pigments (including synthetic and thermochromic pigments) in coating was extensively explored in many studies. For instance, the average solar reflectance of the PDMS/hollow glass bead (HGB) reflective film proposed by Wang et al. [236] increases with the amount of HGBs, reaching 0.96 with 40-50 wt% of HGBs (Fig. 35a). However, for thermochromic pigments, the enhancement of its concentration was discovered to increase the color saturation of coatings, thereby reducing the NIR-reflectance and overall solar reflectance, while increasing the visible reflectance, as depicted in Fig. 35b, c.

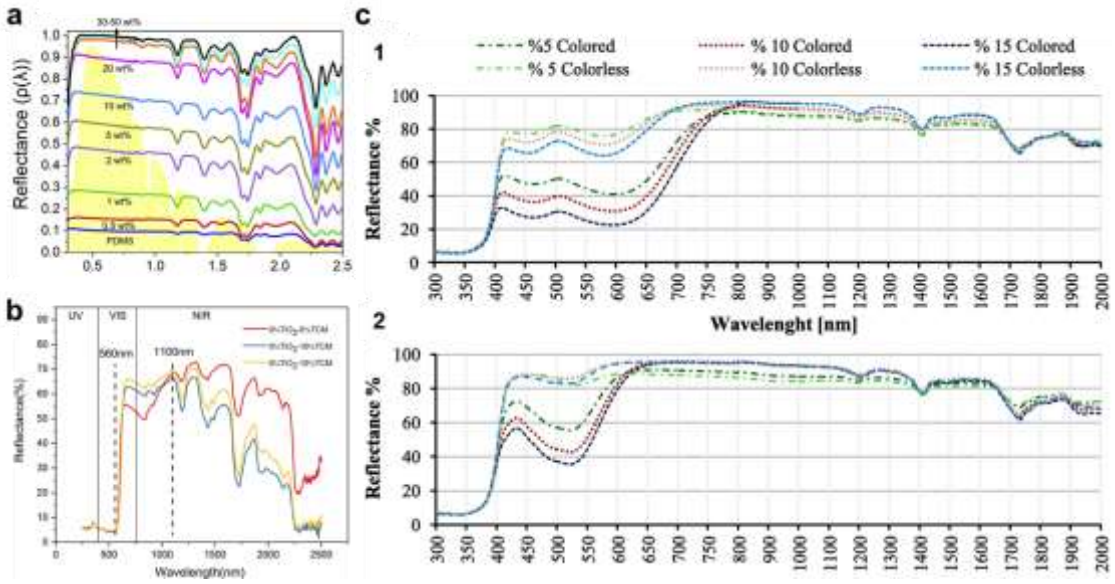

Fig. 35. a) Spectral reflectance of the PDMS/HGB coating films with different HGB mass fractions [236]. b) The reflectance spectra of coatings with different amount of TP in colored phase [240]. c) Total solar reflectance spectrum of thermochromic coatings with different TP contents (5%, 10% and 15%) in (1) black and (2) red color [242].

Table 6. Summary of reflectivity and cooling effect of IR-reflective pigments and coatings.

Color[a)]	Fabrication process[b)]; binder system (coating)	Pigment/Pigmented Coating	R_{NIR} [c), d)]	Thermal Analysis[e)]	Ref
Retailed white	-	TiO_2	87-90%	Lab: surface temperature of coating reduced by about 16.2°C.	[211]
Cool white	Low-temperature liquid-phase; Polystyrene resin and butyl acetate	FAS-modified $BiOCl_xBr_{1-x}$ (x=0-0.875)	86-93.5%	Lab: interior temperature of heat box decreased by 3.9°C with $BiOCl_{0.875}Br_{0.125}$ coating relative to uncoated heat box.	[212]
	-	$ZnTiO_3$	0.115 (solar absorptance)	Field: 1 hour of exposure (sunny day), 2018 summer in Riverside, CA, US. The surface temperature of $ZnTiO_3$ paint was 14.9°C lower than the roof surface temperature (70.1°C).	[14]
	Citrate sol-gel; PU binder	Nanostructured $ZnAl_2O_4$	76-85%, 90% (coating)	-	[218]
	Sol-gel; Acrylic resin	HGM/ZnO composite (with different ZnO morphologies)	94.5-95.7%	Lab: outer surface temperature of the heat box decreased by 11.1°C.	[213]
	Magnetic stirring	Polymer/HGB coating films (polymers: (1) PDMS, (2) WPU, (3) W-Si, (4) WPA)	Solar[f)]: 0.93-0.96	Field: under clear sky from Nov 2020 to Jul 2021 in three cities of China. The polymer/HGB coatings showed sub-ambient cooling of ~7.1°C under direct sunlight. The PDMS/HGB coating film showed decreases in temperature by ~6.9°C.	[236]
Retailed yellow	-	IR-reflective	58.0-67.4%	-	[200]
Cool yellow	Citrate-gel; acrylic binder	$BiVO_4$-ZnO	85.45-92.43%; 75.31% (coating)	Lab: temperature below 25 wt% $BiVO_4$-ZnO coated Al roof was 8.4°C lower than that of commercial yellow paint coated roof.	[202]
	Mixing slurry-sintering; silicone resin	HGM@TiNiY	75.6% (coating)	-	[244]
	Solid-state; PU paint	Ni-doped $BaTi_5O_{11}$	62.32-97.72%	Lab: Ni-doped $BaTi_5O_{11}$ coatings are about 10.3°C cooler than PU-coated tiles.	[217]
	Low-temperature sol-gel calcination; alkyd resin	$GdCe_{1-x}O_{3.5+\gamma}$	~91%	-	[245]
Cool light yellow	In-situ deposited co-precipitation; alkyd resin	HGMs@ZnS_xSe_{1-x}	90.61%	Lab: surface temperature reduction of 9.6±0.2°C with HGMs@ZnS_xSe_{1-x} coating.	[210]
	Hydrothermal; acrylic resin	$Bi_4Ti_3O_{12}$	95-99%	Lab: the temperature difference between the front and back of two plates were 10.2°C (BTO-coated) and 6.2°C (TiO_2-coated).	[234]
	Solid-state; PU binder	$Sr_2M_{1-x}Tb_xO_4$ [M = Sn or Zr]	89.20-96.40%; 48.2-81.6% (Tb=0.4, coating)	-	[216]

	Solid-state (SSR) / Planetary ball milling solid-state (PBM); Acrylic-acralyn binder	$[(LiLaZn)_{x/3}Bi_{1-x}][Mo_xV_{1-x}]O_4$	89-95% (PBM);70-88% (x=0.3, coating)	-	[208]
	Solid-state	$Yb_6Mo_2O_{15}$	93.7%	-	[230]
Retailed brown	-	Iron brown	6% (TSR)	-	[182]
	-	IR-reflective	39% (solar)	-	[200]
Cool red brown	Low-temperature sol-gel	$Ce_2Pr_{0.2}Fe_xO_{4.3+y}$	82.7% (0.2 mol% Fe)	-	[246]
Cool dark brown	Solid-state	$Tb_6Mo_2O_{15}$	51.1%	-	[230]
Retailed blue	-	$CoAl_2O_4$	29%	-	[233]
Cool blue	Solution combustion; water-based acrylic copolymer emulsion	$Zn_{0.9}Co_{0.1}Al_2O_4$	58% (1100 nm); 59% (coating at 1100 nm)	Lab: surface temperature of $Zn_{0.9}Co_{0.1}Al_2O_4$ coated sample was 16°C lower and 9°C higher than carbon-black-coated and white TiO_2-coated samples, respectively.	[220]
	Sol-gel; acrylic and acrylic-acralyn emulsion	$YIn_{0.9}Mn_{0.1}O_3$-ZnO	70%; 67% (coating)	-	[219]
	Sol-gel	$Sr_{1-x}RE_xCuSi_4O_{10+\delta}$	62.64-72.0%	-	[207]
Retailed orange	-	Fe_2O_3-FeO(OH)	57.53%	-	[228]
Cool orange	Mixing and subsequent calcination	$Sr_4Mr_2(Cu_{0.5}Zn_{0.5})O_9$	83.03%	-	[228]
Retailed green	-	pure Cr_2O_3	50%	-	[221, 222]
Cool yellow-green	Solid-state	$Cr_{2-x}Ti_xO_{3+\delta}$	84.04-91.25%	-	[221]
Cool green	Solid-state (SS)/Nano-emulsion (NE); acrylic-acralyn emulsion	Y_2BaCuO_5	58% (SS), 74% (NE); 46-49% (coating)	-	[222]
	Solid-state	$BaCr_2(P_2O_7)_2$	90% (1100 nm)	-	[247]
Retailed black	-	standard carbon black	5.2%	-	[194]
Cool black	Molten salt synthesis; yttria sol	$YFe_xMn_{1-x}O_3$	~75% (coating, 2200 nm)	-	[204]
Retailed red	-	IR-reflective	39.0%	-	[200]
Cool light red	In-situ deposited co-precipitation; alkyd resin	HGMs@Cu-/In-co-doped ZnS_xSe_{1-x} (HGM@ZCI)	73.13%	Lab: surface temperature reduction of 5.7 ± 0.2°C with HGM@ZCI coatings.	[210]
Cool red	Polymeric sol-gel; siloxane	$Y_{2-x}Tb_xZr_{2-y}Fe_yO_{7-\delta}$	90%;70% (coating)	Lab: interior temperature of box with coated (x=0.25) samples was 0.6-1.5°C lower than that of silaxone-coated samples.	[235]
Magenta	Solid-state; acrylic binder	$LiMg_{1-x}Co_xPO_4$	27-64%; 53% (solar, coated	Lab: the interior air and surface temperature of foam box with	[237]

			concrete)	$LiMg_{0.8}Co_{0.2}PO_4$-coated Al sheets reduced by about 7°C, compare to substrates coated with $CoAl_2O_4$.	
Cool multi-colored					
Ivory white to light yellow	Sol-gel; alkyd resin	$Y_2Ce_{2-x}Fe_xO_{7+\delta}$	80.0-96.5%;65.3-90.8% (coating, solar)	Lab: the reduction of indoor ambient temperature of foam box with coating (x=0.1) reached 3.5°C.	[205]
White to brilliant yellow	Acrylamide gel; alkyd resin	$La_2Mo_{2-x}Fe_xO_9$	71-93%; 61-75% (x=0.03 coating)	Lab: the indoor air temperature of boxes coated with synthetic pigments was 4.5°C lower than reference.	[185]
White to bright yellow	Mixing of ingredients and calcination; alkyd resin	$BiVO_4$ coated mica-titanium oxide	77.3-95.4%	Lab: the maximum inner surface temperature of coatings and interior air temperature of foam box were 3.4°C and 2.3°C lower with 30 wt% $BiVO_4$ coated mica-titanium oxide coating, compared to conventional coating.	[238]
White to orange	Solution combustion; alkyd resin	$La_2W_{2-x}Fe_xO_{9-\delta}$ (x=0-0.2)	87.75-92.87%; 86.21% ($La_2W_{1.8}Fe_{0.2}O_{9-\delta}$ coating)	Simulation: model in Nanchang, China during June to August. The average temperature of $La_2W_{1.8}Fe_{0.2}O_{9-\delta}$-coated roof was 5.15°C lower than the cement roof. The energy consumption and electricity cost of the building with $La_2W_{1.8}Fe_{0.2}O_{9-\delta}$-coated exterior wall were reduced by 1.07 kWh/m^2 and $7.32/month, respectively.	[227]
Ivory white to reddish brown	Solid-state; PU binder	$Y_2Ce_{2-x}Tb_xO_7$	55.1-86.9%;68.7-93.3% (coating)	-	[226]
White to red	Chemical liquid deposition; PS/butyl acetate solution	HGM/$BiOCl_{1-x}I_x$ composite	92.6-94.7%	Lab: interior temperature of heat box reduced by 8°C with coated samples.	[181]
White to dark red	Sol-gel (FM), Ammonolysis (FNM); alkyd resin	Fe co-doped $MgTiO_3$ (FN), Fe/N co-doped $MgTiO_3$ (FNM)	53.51-88.58%; 44.94-74.93% (coating)	Lab: reduction of temperature by 2.4°C (surface of plates) and 2°C (interior temperature of boxes), compared with conventional paints	[231]
White to brown	Magnetic stirring of ingredients and combustion; water-based acrylic paint	$LaAl_{1-x}Fe_xO_3$	42.7-87.5% (solar); 35.8-85.3% (coating, solar)	Lab: maximum temperature of samples recorded were 51-58°C using thermal imaging.	[248]
Light yellow to deep red	High-temperature calcination; alkyd resin	$Bi_{3-x}Fe_xYO_6$	53.87%-99.58%	Lab: the temperature of substrate with $Bi_{2.6}Fe_{0.4}YO_6$ coating was 5°C lower than that of conventional yellow coating.	[232]
Yellow to dark yellow	High-temperature calcination; alkyd resin	$Bi_3Y_{1-x}Tb_xO_{6+\delta}$	88.64%-99.87%	Lab: the temperature of Bi_3YO_6 coating was 20°C lower than conventional yellow paint.	[232]
Faint yellow to yellow-orange	Solid-state; alkyd resin	$Bi_{1.7}RE_{0.3}W_{0.7}Mo_{0.3}O_6$ (RE)	>95%; 79.73% ($Bi_{1.7}Lu_{0.3}W_{0.7}Mo_{0.3}O_6$ coating)	-	[225]
Light yellow to	Sol-gel; alkyd resin	$La_2Ce_{2-x}M_xO_7$ [M = Pr or Tb]	75.3-95.95%; 60.77-81.05%	-	[180]

dark orange			(coating)		
Mild yellow to brown	Citrate sol-gel	Ce-, Fe- and Ce-/Fe-doped gahnite	65-86%	-	[229]
Brown to yellow	Sol-gel; alkyd resin	$LaFe_{1-x}Al_xO_3$	52.5-65.4%; 38.7-45.8% (coating)	Lab: with developed coating, the interior air temperature of the foam box decreased by about 5°C, compared to that with standard paint of the same color.	[182]
Brown to orange	Precipitation and sol-gel; alkyd resin	$BiFe_{1-x}Al_xO_3$/mica-titania	57.3-73.6%; 47.8-57.7% (coating)	-	[209]
Yellow to orange	Pechini reoute; alkyd resin	$La_2Ce_{2-x}W_{0.5x}Fe_{0.5x}O_{7+\delta}$	79.87-89.55%; ~71.01% (x=0.3 coating)	-	[224]
Brick red to dark brown	Sol-gel; alkyd	$Zn_{1-x}Mg_xFe_2O_4$	51-58%	Lab: maximum reduction of the surface temperature of coating and interior temperature of boxes were 7.6°C and 6.2°C, respectively.	[184]
Sky blue to intense blue	Solid-state; acrylic-acralyn binder	$Sr_{1-x}La_xCu_{1-y}Li_ySi_4O_{10}$	53-67%; 67% (coating)	-	[249]
Blue to navy blue	Solid-state; acrylic emulsion	$NaZn_{1-x}Co_xPO_4$	52-87%; 61.33%, 62.05% (coating)	Lab: interior temperature of boxes and surface temperature of coated substrates reduced by ~4-4.5°C.	[233]
Blue to dark blue	Solid-state	$Y[In_{1-x}Mn_x]O_3$	~90%	-	[250]
Blue-green to yellow-green	Pechini-type sol-gel; acrylic resin + TiO_2	$Co_{1-x}Zn_xCr_2O_4$	43%-59.5%; 50.6% (coating)	-	[206]
Blue-green to blue	Pechini-type sol-gel; acrylic resin + TiO_2	$CoCr_{2-y}Al_yO_4$	43%-46.7%; 51.9% (coating)	-	[206]
Blue-green to dark blue	Modified citrate; acryl-based	$YFe_xMn_{1-x}O_3$	47.6-60.6%; 20.4-28.4% (coatings)	-	[251]
Yellow-green to green	Solid-state	$Y[In_{1-2x}Cu_xTi_x]O_3$	~90%	-	[250]
Yellow-orange to orange	Solid-state	$Y[In_{1-x}Fe_x]O_3$	~90%	-	[250]
Yellow to yellow-green	Sol-gel	$Y_{6-x}Nd_xMoO_{12}$	82.9-89.9%	-	[252]
Light purple to violet	Solid-state	$Y[In_{1-x-2y}Mn_xTi_yZn_y]O_3$	~90%	-	[250]
Purple to violet	Solid-state; acrylic binder	$LiZn_{1-x}Co_xPO_4$	29.58-68.04%; 50.98-53.34% (coating)	-	[223]
Color-changing (orange/yellow)	Solid-state	$Er_6Mo_2O_{15}$	95.0%	-	[230]
	Solid-state	$Ho_6Mo_2O_{15}$	98.1%	-	[230]
Thermochromic IR-reflective					

Red, blue, yellow, green, black	Mechanical stirring	Retailed thermochromic pigmented coatings (T_c = 31°C)	Solar: 0.40-0.70 (colored), 0.64-0.77 (colorless)	Field experiment: conducted in April 2018 in Shanghai, China under 1) warm, 2) cool and 3) nocturnal weather conditions. The maximum temperature differences of TCM were 1) warm: 0.46-2.63°C (red, yellow and blue).	[240]
Red, yellow, blue, green, black	Mechanical stirring	Retailed thermochromic pigmented coatings with TiO_2 (T_c = 31°C)	Solar: 0.41-0.70 (colored), 0.70-0.77 (colorless)	Simulation: a 2-story office building in Shanghai, China. Coatings were applied on walls and roof. Annual energy consumption with TC was reduced by 4.28-5.02 kWh/m^2 compared to conventional coatings.	[241]
Red, black, magenta	Mechanical mixing	Retailed thermochromic pigmented coatings (T_c = 25/31°C)	Solar: 60-78% (colored). 80-87% (colorless)	Simulation: an office building and its surrounding area in downtown Toronto (Ontario, Canada) modelled. With thermochromic paints, temperature reduction of and 15°C-20°C on facades.	[242]
Black red, blue, yellow	Mechanical stirring	Thermochromic coatings with PMHS (T_c = 30°C)	NIR: 0.777-0.798 (colored), 0.8-0.81 (colorless)	Lab: coatings the surface temperatures of coatings varied between 22.6 to 63.4°C, depending on the ambient temperature. Simulation: in four cities of China, the total energy consumption of the thermochromic coating is lower than cement coating.	[243]
Black, green, violet, red, pink, orange, yellow	Mechanical stirring	PDMS/HGB/TP coatings (T_c = 18, 22, 25, 28°C)	Solar (T_c = 25°C): 87.9-92.1% (blue, colored), 94.7-95.7% (blue, colorless); 89.14-90.7% (pink, colored), 92.1-93.1% (pink, colorless)	Field: under clear sky from Nov 2020 to Jul 2021 in Shanghai, China and Xuzhou, China. The PDMS/HGB/CM coating films showed decreases in temperature by ~6.9°C and ~4.5°C, respectively.	[236]
Blue, black, red, yellow	Mechanical stirring	TP/PDMS coatings (T_c = 28-31°C)	Solar: 0.6937-0.7038 (colored), 0.4896-0.7087 (colorless) IR: 0.3970-0.4035 (colored), 0.3918-0.4114 (colorless)	Field: under sunlight from 8 am to 5 pm, in summer and winter in Changzhou, China. The surface temperatures of the TP/PDMS coatings were 0.9°C lower than CB/PDMS coating and 6.2°C higher than TiO2/PDMS coating. Simulation: using TP/PDMS coating, the annual total energy consumption in North China reduced by 13.74% compared with traditional white cool coating.	[239]

[a)] Color given by reference articles; [b)] Fabrication/synthetic process of synthetic pigments and pigmented coatings; [c)] Reflectance of pigment is given, unless specified otherwise for coatings; [d)] NIR reflectance, R_{NIR} at λ: 700/750/780-2500 nm, unless specified otherwise; [e)] Type of thermal analysis: laboratory (lab), field and simulation; [f)] Solar refers to the solar reflectance at waveband of 250/280-2500 nm.

5.2.2. Cost Analysis on Reviewed Reflective Paints/Pigments

As mentioned in the beginning of Section 5.1, the major materials of wall paints are pigments and binder. Most of the reviewed reflective paints were formulated by dispersing IR-reflective pigments in conventional binders, for instance, acrylic and alkyd resins, which have been used in traditional wall paints. This allows reflective paints to employ formulation that is similar to conventional paints. Thus, for cool paints, which require IR-reflective pigments that are more expensive as compared to conventional pigments, the production cost of IR-pigments is the greatest contributor to the overall cost. Apart from the cost of raw materials, the production cost is also dedicated to the synthetic method and its energy consumption for the heat treatment [11]. Regardless of the pigment colour, the majority of the reviewed synthetic pigments was obtained through solid-state and sol-gel methods (Table 6), which have been broadly utilized for decades. As disclosed in Table 7, the operating conditions, in terms of temperature and time duration, of heat treatment vary depending on the synthesis method used. In general, among various synthesis methods, solid-state method requires the longest duration (2-48 hours) at much higher temperatures (500-1500°C). Higher temperature and longer treatment duration induce higher energy consumption, thereby escalating the production cost. In some cases, multiple treatments were conducted at different treatment temperatures and duration [223, 232, 250], which further increase the cost. In addition, pigments developed by Zhang et al. were even treated with the presence of nitrogen gas [210].

Table 7. Typical conditions of heat treatment used for synthetizing the reviewed pigments.

Fabrication Process	Temperature (°C)	Time Duration
Solid-state	500 to 1500	2 to 48 hours
(Citrate) Sol-gel	300 to 900	30 minutes to 8 hours
Precipitation and sintering/hydrothermal	600-800	40 minutes to 3 hours

5.3. Mechanical and Stability Properties

In addition to optical properties, mechanical strength, stabilities towards chemical, heat, UV-light and weather are essential for outdoor coatings to withstand uncontrollable and inevitable environmental conditions. Poor exterior durability can lead to embrittlement, discoloration, poor adhesion etc. and consequently deteriorates the reflectivity, shortening the lifespan of the coatings. Inorganic pigments have been sought-after as one of the most stable colorants, attributing to their eminent weatherabilities, especially thermal and chemical stabilities [192]. Majority of the composite pigments endure high-temperature calcination in their synthetic processes, e.g., solid-state and possess stable crystalline structures. Hence, the synthetic pigments/coatings inherit stabilities against high-temperature and chemicals (acid/alkalis) from the primary pigments. Besides pigments, binders/resins, which are the film-forming component, are formulators that extensively govern the mechanical properties of coatings, while the inclusion of small amounts of additives modifies some properties of coatings. Alkyd resins are inexpensive oil-based binders, which have been widely used for industrial coatings due to their properties like air-drying, baking cure and good durability [253, 254]. Additionally, acrylic emulsion is another versatile resin for both indoor and outdoor coatings, owing to its excellent properties of strength and resistance to weathering, abrasion and chemicals etc. [253] Other binders like polyurethane and polystyrene also provide mechanical resistance properties for outdoor applications. The pigments, which were blended in their respective resins, were dried in air, whilst several were dried at ~90-150°C after being deposited on substrates [224-226]. Shi et al. [255] developed acrylic-based TiO_2/HGM coatings that remained highly reflective after testing on dirt, scrub, weather resistance and washing with soap solution. Several authors reported their pigments/coatings to be UV-resistant [181, 193, 228, 238]. The variation of colors and reflectance of the synthetized pigments/coatings before and after stability testing was negligible or acceptable according to standards.

Furthermore, the durability of outdoor coatings can be significantly improved with self-cleaning function, i.e. (super)hydrophobicity, by being cleaned easily with rainfall/human cleaning, preventing soil/dust contamination. The wettability of a surface directly relates to the surface free energy and is classified as hydrophilic (water-liking) and hydrophobic (water-hating), which have high and low surface energy, respectively. The water contact angle (WCA) of a surface defines whether the surface is hydrophilic (WCA < 90°) or hydrophobic (WCA ≥ 90°; ≥ 150° for superhydrophobic) [256]. (Super)hydrophobicity can be achieved via chemical modification using low surface energy materials. For instance, Gao et al. [181] modified the surface of HGM/$BiOCl_{1-x}I_x$ pigment with fluorinated alkyl silane (FAS) by undergoing fluoridation, where $BiOCl_{1-x}I_x$ were bonded with fluorinated alkyl chains, and the coating became hydrophobic (Fig. 36a). Regardless of the iodine content, the coatings showed WCA larger than 150° (Fig. 36b) and remained superhydrophobic after the UV-radiation test. Likewise, the same lead author reported another FAS-modified coating of microflower $BiOCl_xBr_{1-x}$ pigments with WCA above 150° on various substrates (Fig. 36c) [212]. The 3D hierarchical structure of the surface texture also promoted superhydrophobicity of these two coatings.

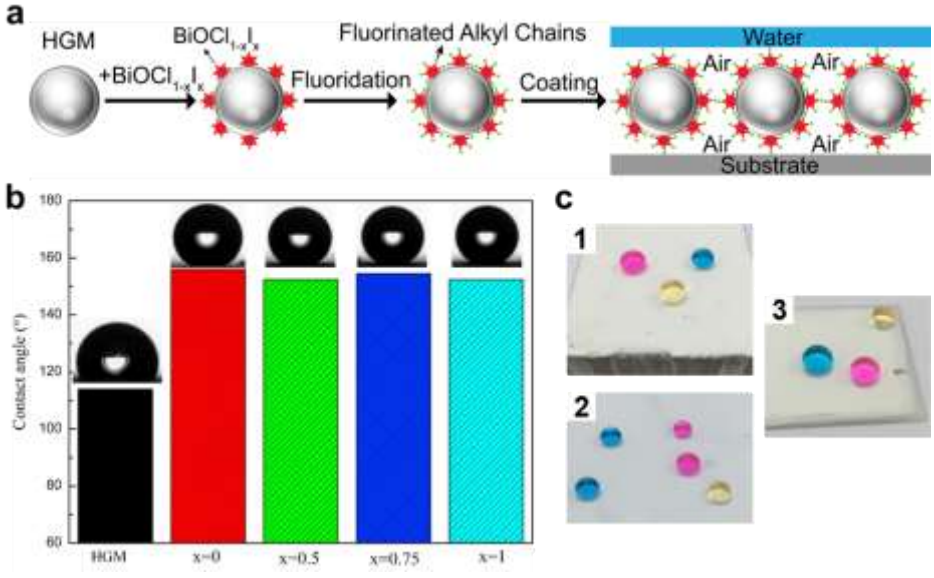

Fig. 36. a) Illustration of fabricating superhydrophobic HGM/$BiOCl_{1-x}I_x$ coating. b) Contact angle and photos of water droplet on HGM/$BiOCl_{1-x}I_x$ coating surface [181]. c) Images of colored water droplet on $BiOCl_xBr_{1-x}$ coated surfaces of different substrates: (1) concrete, (2) aluminum sheet and (3) glass [212].

Room temperature vulcanized silicone rubber (RTV) and polymethylhydrosiloxane (PMHS) are another two low surface energy reagents that were used by Wang et al. [193] and Liu et al. [243], respectively, to develop their thermochromic coatings with self-cleaning function. These coatings exhibited WCA of above 150° and SA of less than 10°, which allow water droplets to remove the dirt on coating surface and naturally fall, as demonstrated by Fig. 37a and b. Recently, Cheng et al. [239] proposed thermochromic coatings with mechanical robustness and self-cleaning property (Fig. 37c). The coatings could retain their superhydrophobicity after temperature and UV irradiation testings, proving their durability as a paint for exterior walls.

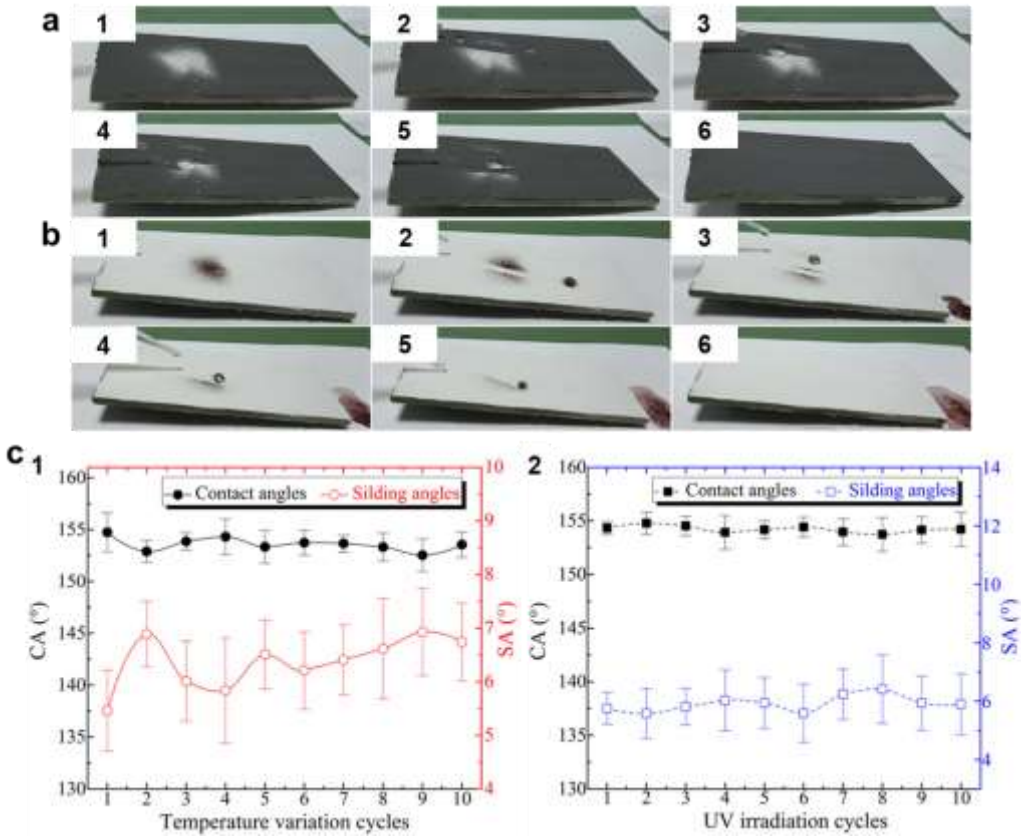

Fig. 37. Self-cleaning behavior of black thermochromic paint in a) colored state ($T < T_c$) and b) colorless state ($T > T_c$) [243]. c) The surface contact angle (CA) and slide angle (SA) of coating in the (1) temperature variation cycles and (2) UV irradiation cycles [239].

Moreover, the topographic texture of surface with micro- and nano-scale roughness creates air pockets between hydrophobic pillars that hold water in spherical shape, preventing water droplet from spreading over the surface [256]. Xue et al. [198], as a representative who modified the surface texture to obtain hydrophobicity, roughened the surface of the orange-gray coatings using emery paper with different grit number. After surface roughening, micro-/nano-scale particles were formed and exposed on surface of the coating, as depicted in Fig. 38a, and consequently provided grooves to trap air, resulting in hydrophobicity. The coatings were reported to have WCA of >150° and exhibited resistance to chemicals and weathering. The reflectivity and self-cleaning properties could be restored by surface roughening using emery paper with the appropriate grit number (Fig. 38b).

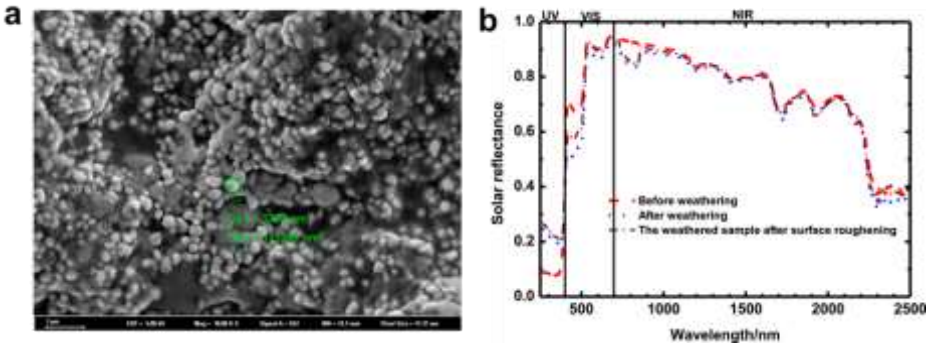

Fig. 38. a) SEM images of surface topologies of coating surface grounded using 180-grit emery paper with high magnifications. Da and Db are the particle diameter and particle area, respectively; b) Comparison of spectral reflectance curves of orange-gray coatings in their initial, weathered and surface roughened states [198].

6. Conclusions and Perspectives

This paper comprehensively reviewed the spectral properties and cooling performance of building technologies, which can passively reduce solar heat gain in three aspects: (1) window, (2) roof and (3) wall, for trimming building electricity consumption and carbon emission in cooling, on the premise of providing pleasant indoor thermal comfort. According to the thermal analyses, the performance of the reviewed passive cooling technologies notably depends on the geographical climates. They are recommended to be utilized in hot/mixed climates, where cooling demand dominates, such that the heating penalty does not offset the overall savings if heating energy increases with the application of these technologies. Fig. 39 depicts the response of the three discussed passive building technologies, in terms of transmission, absorption and reflection, towards solar radiation (0.25-2.5 μm) and thermal radiation (above 2.5 μm).

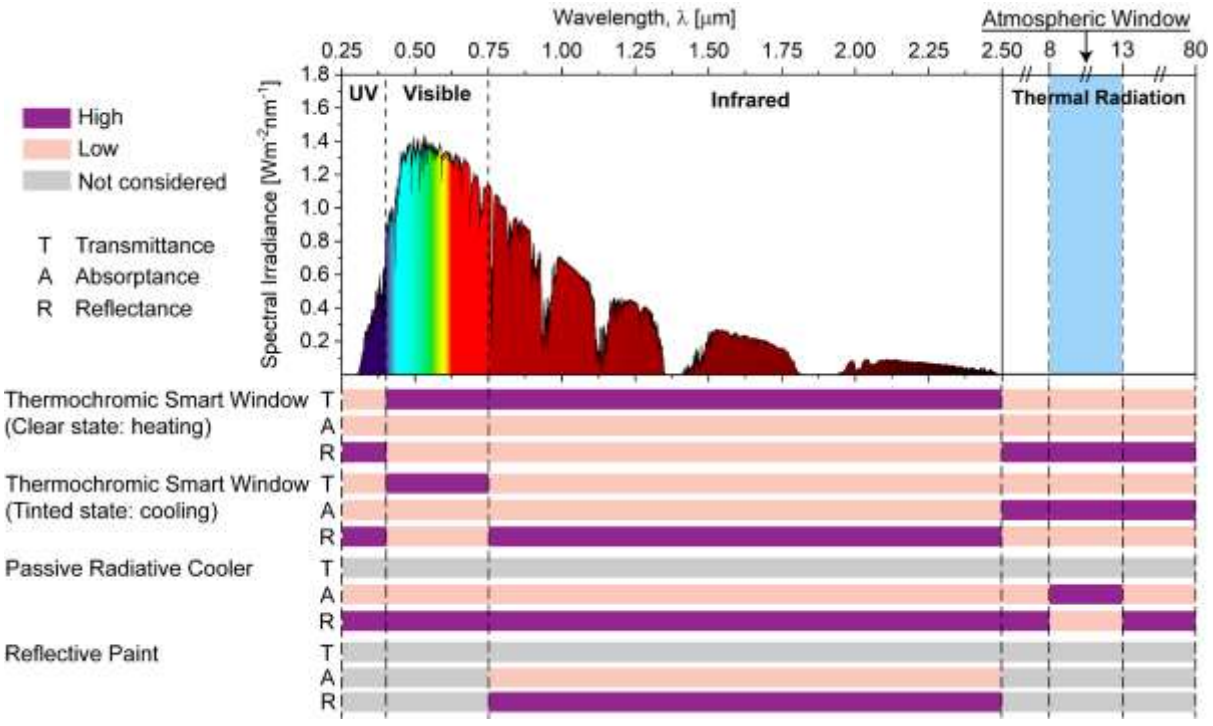

Fig. 39. The ideal spectral properties of (1) thermochromic smart window in clear and tinted states, (2) passive radiative cooler and (3) reflective paint in different wavebands (μm). Purple: high, pink: low and gray: not considered. T: transmittance, A: absorptance and R:

reflectance. (For interpretation of the references in colors in this figure, the reader is referred to the web version of this article.)

(1) For Window: different TCWs have been proposed these years. However, several things need to be fulfilled for each kind of TCWs to prove its energy efficiency.

(a) Most studies concentrate on light transmission (T_{lum}, ΔT_{sol}) of smart windows and transition temperature T_c, yet the heating and cooling of a building are much more complicated. There are many more parameters that should be taken into account to achieve better energy saving performance such as optical properties (T_{lum}, T_{sol}, ΔT_{sol}, reflectance, emissivity), thermal properties (thermal conductivity and thermal capacity) and transition properties (T_c, transition width, and the spectral properties under a range of temperatures).

(b) The design of ideal transition temperature should be based on zone heat balance, instead of ambient air temperature. The switching is a function of incident solar irradiance and outdoor air temperature as solar radiation influences glass temperature and thus effectively lowers the critical switching temperature.

(c) To expand the thermochromism wavelength to the whole solar spectrum, visible thermochromic materials such as hydrogel and perovskite smart windows are usually combined with VO_2. In these cases, the thermochromic phenomenon is triggered by the phase-transition of VO_2 and other thermochromic materials. The ΔT_{sol} for single-thermally driven VO_2 smart coatings ranges from 5 to 20%. The double-thermally driven coatings show largely enhanced ΔT_{sol} of up to 35% [58]. However, this is only the case when two thermochromic materials have similar T_c, if not, a more dedicated model needs to be developed to simulate the transition performance of such windows.

(d) Further, apart from cooling and heating, the lighting energy and fan energy shall also be taken into considerations. TCWs are expected to have negative effect on the lighting load

as the decreased T_{lum} of the hot state gives rise to the need for compensatory interior lighting. Fan energy is the energy for the ventilation system to move the cold/hot air to the vents through the duct system. Since the quantity of cold/hot air changes when TCWs adopt, the fan energy change accordingly.

(2) For Roof: DPRC has proven to be a viable solution for building cooling. Research has made strides in recent years, with many promising results demonstrated both theoretically and experimentally.

(a) The performance parameters defined in this study show that porous alumina [142] exhibits the best fit with the requirements of an ideal DPRC (e_{in}: 0.99, e_{out}: 0.68, A_{sol}: 0.05). Incidentally, these surface anodized aluminum foil coolers have massive potential for future commercialization as they are simple and low cost to fabricate in large scale.

(b) While the focus has shifted away from gases, the authors feel that these materials are underutilized as DPRCs. Since working fluid such as water is not needed in gas-based devices, the properties of gas can be used to design a passive circulation system, i.e., one that is temperature/density driven, further reducing costs.

(c) In addition to energy savings, DPRC application in buildings would also help achieve urban cooling. Studies have shown that lowering outdoor air temperatures may result in fewer occurrences of heat-related mortalities, especially during heatwaves. Despite this, high UV-reflectance can trigger the increased formation of smog (ozone). Therefore, the high solar reflectance of newly developed DPRCs for cool roofs must not extend to the UV-region.

(d) As the specular reflection of some DPRCs can cause glare and (D)PRCs are installed horizontally on the roof, modification is needed to minimize visual discomfort and improve aesthetic appeal.

(e) The operation of DPRCs does not include mechanical/moving parts, resulting in extended service lives and zero noise pollution. However, there is little known about the effect of aging and soiling on DPRCs and their weatherability. For instance, although the DPRC [101], which demonstrated the highest observed net cooling power (127 W/m^2) of all the discussed cooling devices, was developed by PDMS that is a cheap material, the longevity of the polymer under extreme weather conditions is questionable.

(f) It must be acknowledged that there may be hesitancy to embrace the technology due to high fabrication costs and complicated installation and integration with traditional refrigeration systems in buildings, especially given the novelty of the concept.

(3) For wall and roof:

(a) Many researches have endowed reflective paints with high IR-reflectivity and adequate cooling effect as substantiated through spectral and thermal analyzes, while fulfilling aesthetic requirements.

(b) Although the thermal analyses were conducted under different experimental conditions (e.g., substrate and temperature-measuring equipment), the developed reflective paints demonstrated lower temperatures compared with that of respective color-matched conventional coatings or bare substrates, substantiating that they are promising candidates for building cooling application.

(c) Apart from roof and wall surfaces, the reflective paints can also be exploited on façade elements, for instance, external fins, overhangs and external louvres/shutters to enhance the application surface area.

(d) Furthermore, vast majority of the aforesaid pigments/paints is endowed with weatherability, in terms of thermal, chemical and UV-radiation stabilities, which is essential to confront unforeseen environmental events, such as dust gathering, UV irradiation,

temperature/humidity variation, that causes attenuation of reflectivity of the paints. Some pigments/paints are equipped with self-cleaning/anti-fouling properties via chemical modification using low surface energy materials and/or by creating hierarchical micro-/ nanostructures on surface to prevent water/dust contamination. Many studies reported reflective paints with (super)hydrophobicity (WCA of ≥ 90°-150°) that are attributed to the individual or combined effect of physical and chemical modifications. The synergic effect of reflecting solar radiation and outstanding exterior durability can mitigate the effect of thermal stresses on paints and building materials, thereby enhancing their longevity, while absorbing less insolation.

(e) However, the effectiveness of energy saving by applying reflective paints on actual buildings is limited and unclear. Factors such as paint-coated surface area, duration of day, intensity of solar radiation etc. can greatly affect the energy-saving performance.

The implementation of passive energy-efficient technologies on building façades can dampen the growing demand of air-conditioning, on the premise of providing indoor thermal comfort for building occupants. The mitigation of building cooling energy can drive global energy improvement and thus take a step closer to achieving carbon neutrality. Future investigation of thermochromic smart windows, daytime passive radiative coolers and reflective paints shall include:

(1) Their long-term characteristics, in terms of weatherability, resistance against aging and soiling, is highly desired to prove that they have similar or better durability as compared to traditional building façade to promote these technologies for practical adoption.

(2) Effect of buildings types and operating forms: these two features are critical as they significantly impact the heat exchange among appliances and users in both indoor and outdoor environment, thereby affecting the building cooling demand. For example, office

buildings mainly operate from 8 am to 7 pm during weekdays, while hospitals operate 24-hour in order to provide emergency services for sudden illness and long-term care. Hence, the energy-/cost-saving potentials of these passive technologies in different building types shall be explored.

(3) Effect of application surface area: architectural characteristics are designed in coordination with building types, which influence the available application surface area. For instance, buildings with floor-to-ceiling windows have high WWR, which implies extensive surface area for utilizing thermochromic smart windows as window walls, while the application of reflective paints will be limited. As buildings nowadays come in diverse architectural characteristics, in the aspects of WWR and façade elements etc., the applicable type of passive cooling technologies will vary for different buildings depending on their façade features and the surface area that are available for application.

(4) The scale of adopting these technologies and their impact: many researches reported to date mainly concentrate on utilizing these technologies individually and at single-building scale. Investigation on hybrid system that comprises multiple passive building energy-saving technologies has aroused much attention, whilst the effect of their implementation at multi-building to city scale and the impact on buildings' microclimate are scarce.

(5) Further, exploration of manufacturing methods for mass production and cost-effectiveness are of urgent need and significant importance for large-scale implementation of the technologies to promote green buildings. Especially, among these three technologies, DPRC has notably higher manufacturing costs and complicated installation.

Acknowledgment

Y.H.C contributed to the writing the "Roof & Wall: Reflective Paint" section, drafting and revising the manuscript; Y.Z. wrote the "Window: Thermochromic Smart Window" section;

T.T. conducted the writing of the “Roof: Daytime Radiative Cooling” section; S.C.F and K.C.C. reviewed and edited the manuscript; C.Y.T., K.M.Y., M.P.W., B.L.H., S.H.Y., H.H.Q. commented on the manuscript; C.Y.H.C supervised the work. All authors reviewed and provided feedback on the manuscript. This work was supported by the Collaborative Research Fund (CRF) (project no. C6022-16G) granted by the Research Grants Council of the Hong Kong Special Administrative Region, China.

Conflict of Interest

The authors declare no conflict of interest.

References

[1] Architect, A. Lecturer Edward Allen, E. Allen. How buildings work: the natural order of architecture. Oxford University Press2005.
[2] Electrical and Mechanical Services Department. Hong Kong Energy End-use Data 2021. Hong Kong, 2021.
[3] U.Y.A. Tettey, A. Dodoo, L. Gustavsson. Effects of different insulation materials on primary energy and CO2 emission of a multi-storey residential building. Energy Build. 82 (2014) 369-77.
[4] Z. Fang, N. Li, B. Li, G. Luo, Y. Huang. The effect of building envelope insulation on cooling energy consumption in summer. Energy Build. 77 (2014) 197-205.
[5] M.A. William, M.J. Suárez-López, S. Soutullo, A.A. Hanafy. Building envelopes toward energy-efficient buildings: A balanced multi-approach decision making. International Journal of Energy Research. 45 (2021) 21096-113.
[6] L. Troup, R. Phillips, M.J. Eckelman, D. Fannon. Effect of window-to-wall ratio on measured energy consumption in US office buildings. Energy Build. 203 (2019) 109434.
[7] C. Marino, A. Nucara, M. Pietrafesa. Does window-to-wall ratio have a significant effect on the energy consumption of buildings? A parametric analysis in Italian climate conditions. Journal of Building Engineering. 13 (2017) 169-83.
[8] Solar and Infrared Radiation Measurements. CRC Press, Boca Raton, 2017.
[9] M. Santamouris, J. Feng. Recent progress in daytime radiative cooling: is it the air conditioner of the future? Buildings. 8 (2018) 168.
[10] X. Yu, J. Chan, C. Chen. Review of radiative cooling materials: Performance evaluation and design approaches. Nano Energy. 88 (2021) 106259.
[11] A. Rosati, M. Fedel, S. Rossi. NIR reflective pigments for cool roof applications: A comprehensive review. J Cleaner Prod. (2021) 127826.
[12] X. Lu, P. Xu, H. Wang, T. Yang, J. Hou. Cooling potential and applications prospects of passive radiative cooling in buildings: The current state-of-the-art. Renewable Sustainable Energy Rev. 65 (2016) 1079-97.
[13] J. Chen, L. Lu. Development of radiative cooling and its integration with buildings: A comprehensive review. Sol Energy. 212 (2020) 125-51.
[14] J. Lv, M. Tang, R. Quan, Z. Chai. Synthesis of solar heat-reflective ZnTiO3 pigments with novel roof cooling effect. Ceram Int. 45 (2019) 15768-71.
[15] S.Y. Jeong, C.Y. Tso, J. Ha, Y.M. Wong, C.Y. Chao, B. Huang, et al. Field investigation of a photonic multi-layered TiO2 passive radiative cooler in sub-tropical climate. Renewable Energy. 146 (2020) 44-55.
[16] C. Lin, J. Hur, C.Y. Chao, G. Liu, S. Yao, W. Li, et al. All-weather thermochromic windows for synchronous solar and thermal radiation regulation. Sci Adv. 8 (2022) eabn7359.
[17] D.B. Crawley, L.K. Lawrie, F.C. Winkelmann, W.F. Buhl, Y.J. Huang, C.O. Pedersen, et al. EnergyPlus: creating a new-generation building energy simulation program. Energy Build. 33 (2001) 319-31.
[18] M. Arıcı, H. Karabay. Determination of optimum thickness of double-glazed windows for the climatic regions of Turkey. Energy Build. 42 (2010) 1773-8.
[19] S. Selkowitz, O. Aschehoug, E.S. Lee. Advanced Interactive Facades-Critical Elements for Future GreenBuildings? Ernest Orlando Lawrence Berkeley NationalLaboratory, Berkeley, CA (US)2003.
[20] P.R. Somani, S. Radhakrishnan. Electrochromic materials and devices: present and future. Mater Chem Phys. 77 (2003) 117-33.
[21] J.N. Yao, K. Hashimoto, A. Fujishima. Photochromism induced in an electrolytically pretreated Mo03 thin film by visible light. Nature. 355 (1992) 624-6.

[22] S. Liu, C.Y. Tso, H.H. Lee, Y.W. Du, K.M. Yu, S.-P. Feng, et al. Self-densified optically transparent VO2 thermochromic wood film for smart windows. ACS Appl Mater Interfaces. 13 (2021) 22495-504.
[23] Y. Ke, C. Zhou, Y. Zhou, S. Wang, S.H. Chan, Y. Long. Emerging Thermal-Responsive Materials and Integrated Techniques Targeting the Energy-Efficient Smart Window Application. Adv Funct Mater. (2018) 1800113.
[24] S. Babulanam, T. Eriksson, G. Niklasson, C. Granqvist. Thermochromic VO2 films for energy-efficient windows. Sol Energy Mater. 16 (1987) 347-63.
[25] M.B.C. Aries, J.A. Veitch, G.R. Newsham. Windows, view, and office characteristics predict physical and psychological discomfort. J Environ Psychol. 30 (2010) 533-41.
[26] I. Konstantzos, A. Tzempelikos, Y.-C. Chan. Experimental and simulation analysis of daylight glare probability in offices with dynamic window shades. Build Environ. 87 (2015) 244-54.
[27] C.G. Granqvist. Transparent conductors as solar energy materials: A panoramic review. Sol Energy Mater Sol Cells. 91 (2007) 1529-98.
[28] F. Morin. Oxides which show a metal-to-insulator transition at the Neel temperature. Phys Rev Lett. 3 (1959) 34.
[29] N.R. Mlyuka, G.A. Niklasson, C.G. Granqvist. Thermochromic multilayer films of VO2 and TiO2 with enhanced transmittance. Sol Energy Mater Sol Cells. 93 (2009) 1685-7.
[30] S. Wang, M. Liu, L. Kong, Y. Long, X. Jiang, A. Yu. Recent progress in VO2 smart coatings: Strategies to improve the thermochromic properties. Prog Mater Sci. 81 (2016) 1-54.
[31] A. Cavalleri, C. Tóth, C.W. Siders, J. Squier, F. Ráksi, P. Forget, et al. Femtosecond structural dynamics in VO 2 during an ultrafast solid-solid phase transition. Phys Rev Lett. 87 (2001) 237401.
[32] S.-Y. Li, G.A. Niklasson, C.-G. Granqvist. Nanothermochromics: calculations for VO 2 nanoparticles in dielectric hosts show much improved luminous transmittance and solar energy transmittance modulation. J Appl Phys. 108 (2010) 063525.
[33] C. Granqvist. Spectrally selective coatings for energy efficiency and solar applications. Phys Scr. 32 (1985) 401.
[34] P. Jin, S. Tanemura. Relationship between transition temperature and x in V1-xWxO2 films deposited by dual-target magnetron sputtering. Jpn J Appl Phys. 34 (1995) 2459.
[35] C.B. Greenberg. Undoped and doped VO2 films grown from VO (OC3H7) 3. Thin Solid Films. 110 (1983) 73-82.
[36] M. Fukuma, S. Zembutsu, S. Miyazawa. Preparation of VO 2 thin film and its direct optical bit recording characteristics. Appl Opt. 22 (1983) 265-8.
[37] C.M. Lampert, C.-G. Granqvist. Large-area chromogenics: materials and devices for transmittance control. SPIE1990.
[38] M. Sobhan, R. Kivaisi, B. Stjerna, C. Granqvist. Thermochromism of sputter deposited WxV1− xO2 films. Sol Energy Mater Sol Cells. 44 (1996) 451-5.
[39] M. Kong, K. Egbo, C.P. Liu, M.K. Hossain, C.Y. Tso, C.Y.H. Chao, et al. Rapid thermal annealing assisted facile solution method for tungsten-doped vanadium dioxide thin films on glass substrate. J Alloys Compd. (2020) 155053.
[40] N. Wang, M. Duchamp, R.E. Dunin-Borkowski, S. Liu, X. Zeng, X. Cao, et al. Terbium-doped VO2 thin films: reduced phase transition temperature and largely enhanced luminous transmittance. Langmuir. 32 (2016) 759-64.
[41] S.-Y. Li, G.A. Niklasson, C.G. Granqvist. Thermochromic undoped and Mg-doped VO2 thin films and nanoparticles: Optical properties and performance limits for energy efficient windows. J Appl Phys. 115 (2014) 053513.
[42] N. Mlyuka, G. Niklasson, C.-G. Granqvist. Mg doping of thermochromic VO 2 films enhances the optical transmittance and decreases the metal-insulator transition temperature.

Appl Phys Lett. 95 (2009) 171909.
[43] N. Wang, S. Liu, X. Zeng, S. Magdassi, Y. Long. Mg/W-codoped vanadium dioxide thin films with enhanced visible transmittance and low phase transition temperature. J Mater Chem C. 3 (2015) 6771-7.
[44] P. Jin, G. Xu, M. Tazawa, K. Yoshimura. A VO2-based multifunctional window with highly improved luminous transmittance. Jpn J Appl Phys. 41 (2002) L278.
[45] P. Jin, G. Xu, M. Tazawa, K. Yoshimura. Design, formation and characterization of a novel multifunctional window with VO 2 and TiO 2 coatings. Appl Phys A. 77 (2003) 455-9.
[46] G. Xu, P. Jin, M. Tazawa, K. Yoshimura. Optimization of antireflection coating for VO2-based energy efficient window. Sol Energy Mater Sol Cells. 83 (2004) 29-37.
[47] S. Liu, C.Y. Tso, H.H. Lee, Y. Zhang, K.M. Yu, C.Y. Chao. Bio-inspired TiO2 nano-cone antireflection layer for the optical performance improvement of VO2 thermochromic smart windows. Scientific reports. 10 (2020) 1-14.
[48] C. Liu, I. Balin, S. Magdassi, I. Abdulhalim, Y. Long. Vanadium dioxide nanogrid films for high transparency smart architectural window applications. Opt Express. 23 (2015) A124-A32.
[49] Q. Lu, C. Liu, N. Wang, S. Magdassi, D. Mandler, Y. Long. Periodic micro-patterned VO 2 thermochromic films by mesh printing. J Mater Chem C. 4 (2016) 8385-91.
[50] L. Kang, Y. Gao, H. Luo, Z. Chen, J. Du, Z. Zhang. Nanoporous thermochromic VO2 films with low optical constants, enhanced luminous transmittance and thermochromic properties. ACS Appl Mater Interfaces. 3 (2011) 135-8.
[51] L. Kang, Y. Gao, Z. Zhang, J. Du, C. Cao, Z. Chen, et al. Effects of annealing parameters on optical properties of thermochromic VO2 films prepared in aqueous solution. J Phys Chem C. 114 (2010) 1901-11.
[52] X. Cao, N. Wang, J.Y. Law, S.C.J. Loo, S. Magdassi, Y. Long. Nanoporous thermochromic VO2 (M) thin films: controlled porosity, largely enhanced luminous transmittance and solar modulating ability. Langmuir. 30 (2014) 1710-5.
[53] A. Taylor, I. Parkin, N. Noor, C. Tummeltshammer, M.S. Brown, I. Papakonstantinou. A bioinspired solution for spectrally selective thermochromic VO 2 coated intelligent glazing. Opt Express. 21 (2013) A750-A64.
[54] X. Qian, N. Wang, Y. Li, J. Zhang, Z. Xu, Y. Long. Bioinspired multifunctional vanadium dioxide: improved thermochromism and hydrophobicity. Langmuir. 30 (2014) 10766-71.
[55] C. Zhou, D. Li, Y. Tan, Y. Ke, S. Wang, Y. Zhou, et al. 3D Printed Smart Windows for Adaptive Solar Modulations. Adv Opt Mater. 8 (2020) 2000013.
[56] W. Zeng, N. Chen, W. Xie. Research progress on the preparation methods for VO 2 nanoparticles and their application in smart windows. CrystEngComm. 22 (2020) 851-69.
[57] S.-Y. Li, G.A. Niklasson, C.-G. Granqvist. Nanothermochromics with VO2-based core-shell structures: Calculated luminous and solar optical properties. J Appl Phys. 109 (2011) 113515.
[58] T. Chang, X. Cao, Y. Long, H. Luo, P. Jin. How to properly evaluate and compare the thermochromic performance of VO 2-based smart coatings. J Mater Chem A. 7 (2019) 24164-72.
[59] Y. Gao, S. Wang, H. Luo, L. Dai, C. Cao, Y. Liu, et al. Enhanced chemical stability of VO 2 nanoparticles by the formation of SiO 2/VO 2 core/shell structures and the application to transparent and flexible VO 2-based composite foils with excellent thermochromic properties for solar heat control. Energy Environ Sci. 5 (2012) 6104-10.
[60] Y. Chen, X. Zeng, J. Zhu, R. Li, H. Yao, X. Cao, et al. High performance and enhanced durability of thermochromic films using VO2@ ZnO core–shell nanoparticles. ACS Appl Mater Interfaces. 9 (2017) 27784-91.
[61] G.B. Smith. Green nanotechnology: solutions for sustainability and energy in the built

environment. CRC Press2019.
[62] S. Wang, T. Jiang, Y. Meng, R. Yang, G. Tan, Y. Long. Scalable thermochromic smart windows with passive radiative cooling regulation. Science. 374 (2021) 1501-4.
[63] H. Watanabe. Intelligent window using a hydrogel layer for energy efficiency. Sol Energy Mater Sol Cells. 54 (1998) 203-11.
[64] Y. Zhou, Y. Cai, X. Hu, Y. Long. Temperature-responsive hydrogel with ultra-large solar modulation and high luminous transmission for “smart window” applications. J Mater Chem A. 2 (2014) 13550-5.
[65] T.-G. La, X. Li, A. Kumar, Y. Fu, S. Yang, H.-J. Chung. Highly Flexible, Multipixelated Thermosensitive Smart Windows Made of Tough Hydrogels. ACS Appl Mater Interfaces. 9 (2017) 33100-6.
[66] Y.-S. Yang, Y. Zhou, F.B.Y. Chiang, Y. Long. Temperature-responsive hydroxypropylcellulose based thermochromic material and its smart window application. RSC Adv. 6 (2016) 61449-53.
[67] X.-H. Li, C. Liu, S.-P. Feng, N.X. Fang. Broadband Light Management with Thermochromic Hydrogel Microparticles for Smart Windows. Joule. 3 (2019) 290-302.
[68] Y. Zhou, Y. Cai, X. Hu, Y. Long. VO 2/hydrogel hybrid nanothermochromic material with ultra-high solar modulation and luminous transmission. J Mater Chem A. 3 (2015) 1121-6.
[69] H.Y. Lee, Y. Cai, S. Bi, Y.N. Liang, Y. Song, X.M. Hu. A dual-responsive nanocomposite toward climate-adaptable solar modulation for energy-saving smart windows. ACS Appl Mater Interfaces. 9 (2017) 6054-63.
[70] M. Wu, Y. Shi, R. Li, P. Wang. Spectrally selective smart window with high near-infrared light shielding and controllable visible light transmittance. ACS Appl Mater Interfaces. 10 (2018) 39819-27.
[71] Y. Zhou, S. Wang, J. Peng, Y. Tan, C. Li, F.Y.C. Boey, et al. Liquid Thermo-Responsive Smart Window Derived from Hydrogel. Joule. (2020).
[72] H. Du, R. Wickramasinghe, X. Qian. Effects of Salt on the Lower Critical Solution Temperature of Poly (N-Isopropylacrylamide). J Phys Chem B. 114 (2010) 16594-604.
[73] C. Nakamura, T. Yamamoto, K. Manabe, T. Nakamura, Y. Einaga, S. Shiratori. Thermoresponsive, Freezing-Resistant Smart Windows with Adjustable Transition Temperature Made from Hydroxypropyl Cellulose and Glycerol. Ind Eng Chem Res. 58 (2019) 6424-8.
[74] F.B. Chiang. Temperature-responsive hydroxypropylcellulose based thermochromic material and its smart window application. RSC Adv. 6 (2016) 61449-53.
[75] Y.-S. Yang, Y. Zhou, F.B.Y. Chiang, Y. Long. Tungsten doped VO 2/microgels hybrid thermochromic material and its smart window application. RSC Adv. 7 (2017) 7758-62.
[76] G.E. Eperon, V.M. Burlakov, A. Goriely, H.J. Snaith. Neutral color semitransparent microstructured perovskite solar cells. ACS Nano. 8 (2014) 591-8.
[77] Q. Xue, R. Xia, C.J. Brabec, H.-L.J.E. Yip, E. Science. Recent Advances in Semi-Transparent Polymer and Perovskite Solar Cells for Power Generating Window Applications. 11 (2018) 10.1039.C8EE00154E.
[78] D. Liu, C. Yang, R.R. Lunt. Halide Perovskites for Selective Ultraviolet-Harvesting Transparent Photovoltaics. Joule. 2 (2018) 1827-37.
[79] M. De Bastiani, M.I. Saidaminov, I. Dursun, L. Sinatra, W. Peng, U. Buttner, et al. Thermochromic perovskite inks for reversible smart window applications. Chem Mater. 29 (2017) 3367-70.
[80] Y. Zhang, C. Tso, J.S. Iñigo, S. Liu, H. Miyazaki, C.Y. Chao, et al. Perovskite thermochromic smart window: Advanced optical properties and low transition temperature. Appl Energy. 254 (2019) 113690.
[81] S. Liu, Y.W. Du, C.Y. Tso, H.H. Lee, R. Cheng, S.-P. Feng, et al. Organic Hybrid

Perovskite (MAPbI3−xClx) for Thermochromic Smart Window with Strong Optical Regulation Ability, Low Transition Temperature, and Narrow Hysteresis Width. Adv Funct Mater. 31 (2021) 2010426.
[82] A. Halder, D. Choudhury, S. Ghosh, A.S. Subbiah, S.K. Sarkar. Exploring Thermochromic Behavior of Hydrated Hybrid Perovskites in Solar Cells. J Phys Chem Lett. 6 (2015) 3180-4.
[83] B.A. Rosales, L.E. Mundt, L.T. Schelhas, L.M. Wheeler. Reversible Methanolation of Metal Halide Perovskites. Journal of the American Chemical Society. (2022).
[84] Y. Zhang, T. Tennakoon, Y.H. Chan, K.C. Chan, S.C. Fu, C.Y. Tso, et al. Energy consumption modelling of a passive hybrid system for office buildings in different climates. Energy. 239 (2022) 121914.
[85] L.M. Wheeler, D.T. Moore, R. Ihly, N.J. Stanton, E.M. Miller, R.C. Tenent, et al. Switchable photovoltaic windows enabled by reversible photothermal complex dissociation from methylammonium lead iodide. Nat Commun. 8 (2017) 1722.
[86] J. Lin, M. Lai, L. Dou, C.S. Kley, H. Chen, F. Peng, et al. Thermochromic halide perovskite solar cells. Nat Mater. 17 (2018) 261-7.
[87] X. Wei, L. Yu, X. Jin, D. Wang, G.Z. Chen. Solar-thermochromism of Pseudocrystalline Nanodroplets of Ionic Liquid–NiII Complexes Immobilized inside Translucent Microporous PVDF Films. Adv Mater. 21 (2009) 776-80.
[88] J. Zhu, A. Huang, H. Ma, Y. Ma, K. Tong, S. Ji, et al. Composite film of vanadium dioxide nanoparticles and ionic liquid–nickel–chlorine complexes with excellent visible thermochromic performance. ACS Appl Mater Interfaces. 8 (2016) 29742-8.
[89] Y. Chen, J. Zhu, H. Ma, L. Chen, R. Li, P. Jin. VO2/Nickel-bromine-ionic liquid composite film for thermochromic application. Sol Energy Mater Sol Cells. 196 (2019) 124-30.
[90] H.Y. Lee, Y. Cai, S. Velioglu, C. Mu, C.J. Chang, Y.L. Chen, et al. Thermochromic Ionogel: A New Class of Stimuli Responsive Materials with Super Cyclic Stability for Solar Modulation. Chem Mater. 29 (2017) 6947-55.
[91] X. Liang, M. Chen, Q. Wang, S. Guo, L. Zhang, H. Yang. Active and passive modulation of solar light transmittance in a hybrid thermochromic soft-matter system for energy-saving smart window applications. J Mater Chem C. 6 (2018) 7054-62.
[92] X. Liang, C. Guo, M. Chen, S. Guo, L. Zhang, F. Li, et al. A roll-to-roll process for multi-responsive soft-matter composite films containing Cs x WO 3 nanorods for energy-efficient smart window applications. Nanoscale Horiz. 2 (2017) 319-25.
[93] S.-M. Guo, X. Liang, C.-H. Zhang, M. Chen, C. Shen, L.-Y. Zhang, et al. Preparation of a thermally light-transmittance-controllable film from a coexistent system of polymer-dispersed and polymer-stabilized liquid crystals. ACS Appl Mater Interfaces. 9 (2017) 2942-7.
[94] C. Granqvist. Window coatings for the future. Thin Solid Films. 193 (1990) 730-41.
[95] C. Liu, S. Wang, Y. Zhou, H. Yang, Q. Lu, D. Mandler, et al. Index-tunable anti-reflection coatings: Maximizing solar modulation ability for vanadium dioxide-based smart thermochromic glazing. J Alloys Compd. 731 (2018) 1197-207.
[96] L. Zhang, H. Xia, F. Xia, Y. Du, Y. Wu, Y. Gao. Energy-Saving Smart Windows with HPC/PAA Hybrid Hydrogels as Thermochromic Materials. ACS Applied Energy Materials. 4 (2021) 9783-91.
[97] M. Mahdavinejad, K. Javanrudi. Assessment of ancient fridges: A sustainable method to storage ice in hot-arid climates. Asian Culture and History. 4 (2012) 133.
[98] F. Arago. Oeuvres complètes de François Arago. Gide et J. baudry1862.
[99] A.P. Raman, M. Abou Anoma, L. Zhu, E. Rephaeli, S. Fan. Passive radiative cooling below ambient air temperature under direct sunlight. Nature. 515 (2014) 540-4.
[100] E. Rephaeli, A. Raman, S. Fan. Ultrabroadband photonic structures to achieve high-performance daytime radiative cooling. Nano Lett. 13 (2013) 1457-61.
[101] J.-l. Kou, Z. Jurado, Z. Chen, S. Fan, A.J. Minnich. Daytime radiative cooling using near-

black infrared emitters. ACS Photonics. 4 (2017) 626-30.
[102] K. Lin, L. Chao, T.C. Ho, C. Lin, S. Chen, Y. Du, et al. A Flexible and Scalable Solution for Daytime Passive Radiative Cooling Using Polymer Sheets. Energy Build. (2021) 111400.
[103] P. Yang, C. Chen, Z.M. Zhang. A dual-layer structure with record-high solar reflectance for daytime radiative cooling. Sol Energy. 169 (2018) 316-24.
[104] J. Mandal, Y. Fu, A.C. Overvig, M. Jia, K. Sun, N.N. Shi, et al. Hierarchically porous polymer coatings for highly efficient passive daytime radiative cooling. Science. 362 (2018) 315-9.
[105] J. Mandal, M. Jia, A. Overvig, Y. Fu, E. Che, N. Yu, et al. Porous polymers with switchable optical transmittance for optical and thermal regulation. Joule. 3 (2019) 3088-99.
[106] T. Wang, Y. Wu, L. Shi, X. Hu, M. Chen, L. Wu. A structural polymer for highly efficient all-day passive radiative cooling. Nat Commun. 12 (2021) 1-11.
[107] T. Li, Y. Zhai, S. He, W. Gan, Z. Wei, M. Heidarinejad, et al. A radiative cooling structural material. Science. 364 (2019) 760-3.
[108] E.M. Lushiku, C.-G. Granqvist. Radiative cooling with selectively infrared-emitting gases. Appl Opt. 23 (1984) 1835-43.
[109] E. Lushiku, A. Hjortsberg, C. Granqvist. Radiative cooling with selectively infrared-emitting ammonia gas. J Appl Phys. 53 (1982) 5526-30.
[110] A. Hjortsberg, C. Granqvist. Radiative cooling with selectively emitting ethylene gas. Appl Phys Lett. 39 (1981) 507-9.
[111] F.K. Khosroshahi, H. Ertürk, M.P. Mengüç. Optimization of spectrally selective Si/SiO2 based filters for thermophotovoltaic devices. J Quant Spectrosc Radiat Transfer. 197 (2017) 123-31.
[112] Z. Chen, L. Zhu, A. Raman, S. Fan. Radiative cooling to deep sub-freezing temperatures through a 24-h day–night cycle. Nat Commun. 7 (2016) 1-5.
[113] M. Ono, K. Chen, W. Li, S. Fan. Self-adaptive radiative cooling based on phase change materials. Opt Express. 26 (2018) A777-A87.
[114] S. Taylor, Y. Yang, L. Wang. Vanadium dioxide based Fabry-Perot emitter for dynamic radiative cooling applications. J Quant Spectrosc Radiat Transfer. 197 (2017) 76-83.
[115] H. Bao, C. Yan, B. Wang, X. Fang, C. Zhao, X. Ruan. Double-layer nanoparticle-based coatings for efficient terrestrial radiative cooling. Sol Energy Mater Sol Cells. 168 (2017) 78-84.
[116] A.R. Gentle, G.B. Smith. A subambient open roof surface under the Mid-Summer sun. Advanced Science. 2 (2015) 1500119.
[117] T. Suichi, A. Ishikawa, Y. Hayashi, K. Tsuruta. Performance limit of daytime radiative cooling in warm humid environment. AIP Adv. 8 (2018) 055124.
[118] Y. Cui, Y. He, Y. Jin, F. Ding, L. Yang, Y. Ye, et al. Plasmonic and metamaterial structures as electromagnetic absorbers. Laser Photonics Rev. 8 (2014) 495-520.
[119] J.A. Schuller, E.S. Barnard, W. Cai, Y.C. Jun, J.S. White, M.L. Brongersma. Plasmonics for extreme light concentration and manipulation. Nat Mater. 9 (2010) 193-204.
[120] L. Wang, Z. Zhang. Measurement of coherent thermal emission due to magnetic polaritons in subwavelength microstructures. J Heat Transfer. 135 (2013) 091505.
[121] A. Hervé, J. Drévillon, Y. Ezzahri, K. Joulain. Radiative cooling by tailoring surfaces with microstructures: Association of a grating and a multi-layer structure. J Quant Spectrosc Radiat Transfer. 221 (2018) 155-63.
[122] R.Y. Wong, C.Y. Tso, C.Y. Chao, B. Huang, M.P. Wan. Ultra-broadband asymmetric transmission metallic gratings for subtropical passive daytime radiative cooling. Sol Energy Mater Sol Cells. 186 (2018) 330-9.
[123] C. Zou, G. Ren, M.M. Hossain, S. Nirantar, W. Withayachumnankul, T. Ahmed, et al. Metal-Loaded dielectric resonator metasurfaces for radiative cooling. Adv Opt Mater. 5 (2017)

1700460.
[124] M.M. Hossain, B. Jia, M. Gu. A metamaterial emitter for highly efficient radiative cooling. Adv Opt Mater. 3 (2015) 1047-51.
[125] J.-W. Cho, T.-I. Lee, D.-S. Kim, K.-H. Park, Y.-S. Kim, S.-K. Kim. Visible to near-infrared thermal radiation from nanostructured tungsten anntennas. J Opt. 20 (2018) 09LT1.
[126] Y. Qu, L. Cai, H. Luo, J. Lu, M. Qiu, Q. Li. Tunable dual-band thermal emitter consisting of single-sized phase-changing GST nanodisks. Opt Express. 26 (2018) 4279-87.
[127] S. Jeong, C.Y. Tso, Y.M. Wong, C.Y. Chao, B. Huang. Daytime passive radiative cooling by ultra emissive bio-inspired polymeric surface. Sol Energy Mater Sol Cells. 206 (2020) 110296.
[128] H. Zhang, K.C. Ly, X. Liu, Z. Chen, M. Yan, Z. Wu, et al. Biologically inspired flexible photonic films for efficient passive radiative cooling. Proc Natl Acad Sci. 117 (2020) 14657-66.
[129] H. Wang, K. O'Dea, L. Wang. Selective absorption of visible light in film-coupled nanoparticles by exciting magnetic resonance. Opt Lett. 39 (2014) 1457-60.
[130] Z.-X. Jia, Y. Shuai, M. Li, Y. Guo, H.-p. Tan. Enhancement radiative cooling performance of nanoparticle crystal via oxidation. J Quant Spectrosc Radiat Transfer. 207 (2018) 23-31.
[131] S.-R. Wu, K.-L. Lai, C.-M. Wang. Passive temperature control based on a phase change metasurface. Scientific reports. 8 (2018) 1-6.
[132] W.L. Min, B. Jiang, P. Jiang. Bioinspired self-cleaning antireflection coatings. Adv Mater. 20 (2008) 3914-8.
[133] D. Wu, C. Liu, Z. Xu, Y. Liu, Z. Yu, L. Yu, et al. The design of ultra-broadband selective near-perfect absorber based on photonic structures to achieve near-ideal daytime radiative cooling. Mater Des. 139 (2018) 104-11.
[134] N.N. Shi, C.-C. Tsai, C. Craig, N. Yu. Nano-structured wild moth cocoon fibers as radiative cooling and waveguiding optical materials. CLEO: Science and Innovations. Optical Society of America2017. p. STh4I. 2.
[135] A. Harrison, M. Walton. Radiative cooling of TiO2 white paint. Sol Energy. 20 (1978) 185-8.
[136] B. Orel, M.K. Gunde, A. Krainer. Radiative cooling efficiency of white pigmented paints. Sol Energy. 50 (1993) 477-82.
[137] Z. Huang, X. Ruan. Nanoparticle embedded double-layer coating for daytime radiative cooling. Int J Heat Mass Transfer. 104 (2017) 890-6.
[138] Y. Zhai, Y. Ma, S.N. David, D. Zhao, R. Lou, G. Tan, et al. Scalable-manufactured randomized glass-polymer hybrid metamaterial for daytime radiative cooling. Science. 355 (2017) 1062-6.
[139] H. Fang, D. Zhao, J. Yuan, A. Aili, X. Yin, R. Yang, et al. Performance evaluation of a metamaterial-based new cool roof using improved Roof Thermal Transfer Value model. Appl Energy. 248 (2019) 589-99.
[140] C. Lin, Y. Li, C. Chi, Y.S. Kwon, J. Huang, Z. Wu, et al. A Solution-processed Inorganic Emitter with High Spectral Selectivity for Efficient Subambient Radiative Cooling in Hot Humid Climates. Adv Mater. (2022) 2109350.
[141] S. Atiganyanun, J.B. Plumley, S.J. Han, K. Hsu, J. Cytrynbaum, T.L. Peng, et al. Effective radiative cooling by paint-format microsphere-based photonic random media. ACS Photonics. 5 (2018) 1181-7.
[142] Y. Fu, J. Yang, Y. Su, W. Du, Y. Ma. Daytime passive radiative cooler using porous alumina. Sol Energy Mater Sol Cells. 191 (2019) 50-4.
[143] S. Son, S. Jeon, D. Chae, S.Y. Lee, Y. Liu, H. Lim, et al. Colored emitters with silica-embedded perovskite nanocrystals for efficient daytime radiative cooling. Nano Energy. 79 (2021) 105461.

[144] H. Zhai, D. Fan, Q. Li. Scalable and paint-format colored coatings for passive radiative cooling. Sol Energy Mater Sol Cells. 245 (2022) 111853.
[145] X. Sun, Y. Sun, Z. Zhou, M.A. Alam, P. Bermel. Radiative sky cooling: fundamental physics, materials, structures, and applications. Nanophotonics. 6 (2017) 997-1015.
[146] C. Granqvist, A. Hjortsberg. Radiative cooling to low temperatures: General considerations and application to selectively emitting SiO films. J Appl Phys. 52 (1981) 4205-20.
[147] X. Ao, M. Hu, B. Zhao, N. Chen, G. Pei, C. Zou. Preliminary experimental study of a specular and a diffuse surface for daytime radiative cooling. Sol Energy Mater Sol Cells. 191 (2019) 290-6.
[148] B. Zhao, M. Hu, X. Ao, G. Pei. Performance evaluation of daytime radiative cooling under different clear sky conditions. Appl Therm Eng. 155 (2019) 660-6.
[149] C.Y. Tso, K.C. Chan, C.Y. Chao. A field investigation of passive radiative cooling under Hong Kong's climate. Renewable Energy. 106 (2017) 52-61.
[150] W. Wang, N. Fernandez, S. Katipamula, K. Alvine. Performance assessment of a photonic radiative cooling system for office buildings. Renewable Energy. 118 (2018) 265-77.
[151] K. Zhang, D. Zhao, X. Yin, R. Yang, G. Tan. Energy saving and economic analysis of a new hybrid radiative cooling system for single-family houses in the USA. Appl Energy. 224 (2018) 371-81.
[152] M.A. Kecebas, M.P. Menguc, A. Kosar, K. Sendur. Passive radiative cooling design with broadband optical thin-film filters. J Quant Spectrosc Radiat Transfer. 198 (2017) 179-86.
[153] H. Ma, K. Yao, S. Dou, M. Xiao, M. Dai, L. Wang, et al. Multilayered SiO2/Si3N4 photonic emitter to achieve high-performance all-day radiative cooling. Sol Energy Mater Sol Cells. 212 (2020) 110584.
[154] S. Catalanotti, V. Cuomo, G. Piro, D. Ruggi, V. Silvestrini, G. Troise. The radiative cooling of selective surfaces. Sol Energy. 17 (1975) 83-9.
[155] D. Chae, M. Kim, P.-H. Jung, S. Son, J. Seo, Y. Liu, et al. Spectrally selective inorganic-based multilayer emitter for daytime radiative cooling. ACS Appl Mater Interfaces. 12 (2020) 8073-81.
[156] H. Miyazaki, K. Oe, M. Tsuruta. Fabrication of radiative cooling coatings and composite films using Si2N2O nano-particles with wide range temperatures. Open Ceramics. 4 (2020) 100039.
[157] R. Yang, X. Yin. Passive cooling in an urban setting. Nat Sustain. 2 (2019) 663-4.
[158] L. Zhou, H. Song, J. Liang, M. Singer, M. Zhou, E. Stegenburgs, et al. A polydimethylsiloxane-coated metal structure for all-day radiative cooling. Nat Sustain. 2 (2019) 718-24.
[159] N. Nilsson, T. Eriksson, C. Granqvist. Infrared-transparent convection shields for radiative cooling: Initial results on corrugated polyethylene foils. Sol Energy Mater. 12 (1985) 327-33.
[160] A.H.H. Ali, H. Saito, I. Taha, K. Kishinami, I. Ismail. Effect of aging, thickness and color on both the radiative properties of polyethylene films and performance of the nocturnal cooling unit. Energy Convers Manage. 39 (1998) 87-93.
[161] A. Gentle, K. Dybdal, G. Smith. Polymeric mesh for durable infra-red transparent convection shields: Applications in cool roofs and sky cooling. Sol Energy Mater Sol Cells. 115 (2013) 79-85.
[162] S.N. Bathgate, S.G. Bosi. A robust convection cover material for selective radiative cooling applications. Sol Energy Mater Sol Cells. 95 (2011) 2778-85.
[163] S.G. Bosi, S.N. Bathgate, D.R. Mills. At last! A durable convection cover for atmospheric window radiative cooling applications. Energy Procedia. 57 (2014) 1997-2004.
[164] D.C. Harris. Materials for infrared windows and domes: properties and performance.

SPIE press1999.
[165] M. Benlattar, E. Oualim, M. Harmouchi, A. Mouhsen, A. Belafhal. Radiative properties of cadmium telluride thin film as radiative cooling materials. Opt Commun. 256 (2005) 10-5.
[166] A. Andretta, B. Bartoli, B. Coluzzi, V. Cuomo. Selective surfaces for natural cooling devices. J Phys Colloques. 42 (1981) C1-423-C1-30.
[167] Y. Mastai, Y. Diamant, S. Aruna, A. Zaban. TiO2 nanocrystalline pigmented polyethylene foils for radiative cooling applications: synthesis and characterization. Langmuir. 17 (2001) 7118-23.
[168] K. Dobson, G. Hodes, Y. Mastai. Thin semiconductor films for radiative cooling applications. Sol Energy Mater Sol Cells. 80 (2003) 283-96.
[169] T. Engelhard, E. Jones, I. Viney, Y. Mastai, G. Hodes. Deposition of tellurium films by decomposition of electrochemically-generated H2Te: application to radiative cooling devices. Thin Solid Films. 370 (2000) 101-5.
[170] T.M. Nilsson, G.A. Niklasson. Radiative cooling during the day: simulations and experiments on pigmented polyethylene cover foils. Sol Energy Mater Sol Cells. 37 (1995) 93-118.
[171] A. Leroy, B. Bhatia, C.C. Kelsall, A. Castillejo-Cuberos, M. Di Capua H, L. Zhao, et al. High-performance subambient radiative cooling enabled by optically selective and thermally insulating polyethylene aerogel. Sci Adv. 5 (2019) eaat9480.
[172] D. Zhao, A. Aili, Y. Zhai, J. Lu, D. Kidd, G. Tan, et al. Subambient cooling of water: Toward real-world applications of daytime radiative cooling. Joule. 3 (2019) 111-23.
[173] X. Fan, K. Shi, Z. Xia. Using multi-layer structure to improve the radiative cooling performance. J Quant Spectrosc Radiat Transfer. 251 (2020) 107052.
[174] E.A. Goldstein, A.P. Raman, S. Fan. Sub-ambient non-evaporative fluid cooling with the sky. Nat Energy. 2 (2017) 1-7.
[175] S.Y. Jeong, C.Y. Tso, M. Zouagui, Y.M. Wong, C.Y. Chao. A numerical study of daytime passive radiative coolers for space cooling in buildings. Build Simul. Springer2018. pp. 1011-28.
[176] D. Zhao, A. Aili, X. Yin, G. Tan, R. Yang. Roof-integrated radiative air-cooling system to achieve cooler attic for building energy saving. Energy Build. 203 (2019) 109453.
[177] K. Zhang, D. Zhao, Y. Zhai, X. Yin, R. Yang, G. Tan. Modelling study of the low-pump-power demand constructal T-shaped pipe network for a large scale radiative cooled-cold storage system. Appl Therm Eng. 127 (2017) 1564-73.
[178] A. Aili, D. Zhao, J. Lu, Y. Zhai, X. Yin, G. Tan, et al. A kW-scale, 24-hour continuously operational, radiative sky cooling system: experimental demonstration and predictive modeling. Energy Convers Manage. 186 (2019) 586-96.
[179] D. Zhao, C.E. Martini, S. Jiang, Y. Ma, Y. Zhai, G. Tan, et al. Development of a single-phase thermosiphon for cold collection and storage of radiative cooling. Appl Energy. 205 (2017) 1260-9.
[180] B. Huang, Y. Xiao, C. Huang, J. Chen, X. Sun. Environment-friendly pigments based on praseodymium and terbium doped La2Ce2O7 with high near-infrared reflectance: synthesis and characterization. Dyes Pigm. 147 (2017) 225-33.
[181] Q. Gao, X. Wu, Y. Fan, Q. Meng. Novel near infrared reflective pigments based on hollow glass microsphere/BiOCl1-xIx composites: Optical property and superhydrophobicity. Sol Energy Mater Sol Cells. 180 (2018) 138-47.
[182] L. Liu, A. Han, M. Ye, M. Zhao. Synthesis and characterization of Al3+ doped LaFeO3 compounds: a novel inorganic pigments with high near-infrared reflectance. Sol Energy Mater Sol Cells. 132 (2015) 377-84.
[183] R. Levinson, H. Akbari, P. Berdahl. Measuring solar reflectance—Part I: Defining a metric that accurately predicts solar heat gain. Solar Energy. 84 (2010) 1717-44.

[184] L. Liu, A. Han, M. Ye, W. Feng. The evaluation of thermal performance of cool coatings colored with high near-infrared reflective nano-brown inorganic pigments: Magnesium doped ZnFe2O4 compounds. Sol Energy. 113 (2015) 48-56.
[185] A. Han, M. Ye, L. Liu, W. Feng, M. Zhao. Estimating thermal performance of cool coatings colored with high near-infrared reflective inorganic pigments: Iron doped La2Mo2O7 compounds. Energy Build. 84 (2014) 698-703.
[186] R. Levinson, P. Berdahl, H. Akbari. Solar spectral optical properties of pigments—Part I: model for deriving scattering and absorption coefficients from transmittance and reflectance measurements. Sol Energy Mater Sol Cells. 89 (2005) 319-49.
[187] Y.-F. Lim. Novel materials and concepts for regulating infra-red radiation: radiative cooling and cool paint. Energy Saving Coating Materials. Elsevier2020. pp. 113-31.
[188] Z.W. Wicks, F.N. Jones, S.P. Pappas, D.A. Wicks. Organic Coatings: Science and Technology. Wiley2007.
[189] C.-W.P. Puesan, J.-L.Z. Mestre. Technical evaluation of an improved paint coating with NIR pigments designed to reduce thermal discomfort caused by incident solar radiation: application in the Caribbean area. Energy Procedia. 115 (2017) 463-79.
[190] S. Jose, D. Joshy, S.B. Narendranath, P. Periyat. Recent advances in infrared reflective inorganic pigments. Sol Energy Mater Sol Cells. 194 (2019) 7-27.
[191] A. Zhou, Z. Yu, C.L. Chow, D. Lau. Enhanced solar spectral reflectance of thermal coatings through inorganic additives. Energy Build. 138 (2017) 641-7.
[192] G. Buxbaum. Industrial inorganic pigments. John Wiley & Sons2008.
[193] F. Wang, T. Xie, J. Ou, M. Xue, W. Li. Cement based superhydrophobic coating with excellent robustness and solar reflective ability. J Alloys Compd. 823 (2020) 153702.
[194] C. Zhu, W. Lin, L. Chen, J. Lv, J. Zhang, J. Feng. Deep color, heat-reflective, superhydrophobic and anti-soiling coatings with waterborne silicone emulsion. Sol Energy Mater Sol Cells. 199 (2019) 129-35.
[195] B. Li, J. Yuan, Z. An, J. Zhang. Effect of microstructure and physical parameters of hollow glass microsphere on insulation performance. Mater Lett. 65 (2011) 1992-4.
[196] L. Jiang, X. Xue, J. Qu, J. Qin, J. Song, Y. Shi, et al. The methods for creating energy efficient cool gray building coatings—Part II: Preparation from pigments of complementary colors and titanium dioxide rutile. Sol Energy Mater Sol Cells. 130 (2014) 410-9.
[197] X. Xue, J. Qin, J. Song, J. Qu, Y. Shi, W. Zhang, et al. The methods for creating energy efficient cool gray building coatings—Part I: Preparation from white and black pigments. Sol Energy Mater Sol Cells. 130 (2014) 587-98.
[198] X. Xue, Z. Yang, Y. Li, P. Sun, Y. Feng, Z. He, et al. Superhydrophobic self-cleaning solar reflective orange-gray paint coating. Sol Energy Mater Sol Cells. 174 (2018) 292-9.
[199] Z. Yang, X. Xue, J.-g. Dai, Y. Li, J. Qin, Y. Feng, et al. Study of a super-non-wetting self-cleaning solar reflective blue-grey paint coating with luminescence. Sol Energy Mater Sol Cells. 176 (2018) 69-80.
[200] V.C. Malshe, A.K. Bendiganavale. Infrared reflective inorganic pigments. Recent Pat Chem Eng. 1 (2008) 67-79.
[201] E. Coser, V.F. Moritz, A. Krenzinger, C.A. Ferreira. Development of paints with infrared radiation reflective properties. Polímeros. 25 (2015) 305-10.
[202] P. Thejus, K. Nishanth. Rational approach to synthesis low-cost BiVO4–ZnO complex inorganic pigment for energy efficient buildings. Sol Energy Mater Sol Cells. 200 (2019) 109999.
[203] S.D. Dolić, D.J. Jovanović, D. Štrbac, L.Đ. Far, M.D. Dramićanin. Improved coloristic properties and high NIR reflectance of environment-friendly yellow pigments based on bismuth vanadate. Ceram Int. 44 (2018) 22731-7.
[204] Y. Ma, Y. Chen, Z. Wang, H. Liu, Y. Li, X. Wang, et al. Controllable near-infrared

reflectivity and infrared emissivity with substitutional iron-doped orthorhombic YMnO3 coatings. Sol Energy. 206 (2020) 778-86.
[205] M. Zhao, A. Han, M. Ye, T. Wu. Preparation and characterization of Fe3+ doped Y2Ce2O7 pigments with high near-infrared reflectance. Sol Energy. 97 (2013) 350-5.
[206] H. Hedayati, A.S. Alvani, H. Sameie, R. Salimi, S. Moosakhani, F. Tabatabaee, et al. Synthesis and characterization of Co1− xZnxCr2− yAlyO4 as a near-infrared reflective color tunable nano-pigment. Dyes Pigm. 113 (2015) 588-95.
[207] J. Jing, Y. Zhang, J. Sun, X. Zhao, D. Gao, Y. Zhang. A comparative study on different RE-doped (RE= Pr, Nd, Sm) SrCuSi4O10 blue pigments with high near-infrared reflectance. Dyes Pigm. 150 (2018) 9-15.
[208] T. Aju Thara, P.P. Rao, S. Divya, A.K. Raj, T. Sreena. Enhanced near infrared reflectance with brilliant yellow hues in scheelite type solid solutions,(LiLaZn) 1/3MoO4–BiVO4 for energy saving products. ACS Sustainable Chem Eng. 5 (2017) 5118-26.
[209] L. Yuan, A. Han, M. Ye, X. Chen, C. Ding, L. Yao. Synthesis and characterization of novel nontoxic BiFe1− xAlxO3/mica-titania pigments with high NIR reflectance. Ceram Int. 43 (2017) 16488-94.
[210] T. Zhang, Y. Wang, Z. Pan. Preparation of hollow glass microspheres@ ZnSxSe1− x or copper-/indium-co-doped ZnSxSe1− x composite color pigments with enhanced near-infrared reflectance. Sol Energy. 184 (2019) 570-83.
[211] Z. Song, W. Zhang, Y. Shi, J. Song, J. Qu, J. Qin, et al. Optical properties across the solar spectrum and indoor thermal performance of cool white coatings for building energy efficiency. Energy Build. 63 (2013) 49-58.
[212] Q. Gao, X. Wu, R. Zhu. Antifouling energy-efficient coatings based on BiOClxBr1− x microflowers: NIR reflective property and superhydrophobicity. Constr Build Mater. 257 (2020) 119569.
[213] D. Lu, Q. Gao, X. Wu, Y. Fan. ZnO nanostructures decorated hollow glass microspheres as near infrared reflective pigment. Ceram Int. 43 (2017) 9164-70.
[214] E. Cozza, M. Alloisio, A. Comite, G. Di Tanna, S. Vicini. NIR-reflecting properties of new paints for energy-efficient buildings. Sol Energy. 116 (2015) 108-16.
[215] K. Dornelles, R. Caram, E. Sichieri. Natural weathering of cool coatings and its effect on solar reflectance of roof surfaces. Energy Procedia. 78 (2015) 1587-92.
[216] A.K. Raj, P.P. Rao, S. Divya, T. Ajuthara. Terbium doped Sr2MO4 [M= Sn and Zr] yellow pigments with high infrared reflectance for energy saving applications. Powder Technol. 311 (2017) 52-8.
[217] J. Zou, P. Zhang. Ni-doped BaTi5O11: New brilliant yellow pigment with high NIR reflectance as solar reflective fillers. Ceram Int. 46 (2020) 3490-7.
[218] S. Sameera, V. Vidyadharan, S. Sasidharan, K. Gopchandran. Nanostructured zinc aluminates: A promising material for cool roof coating. J Sci: Adv Mater Devices. 4 (2019) 524-30.
[219] S. Jose, A. Jayaprakash, S. Laha, S. Natarajan, K. Nishanth, M. Reddy. YIn0. 9Mn0. 1O3–ZnO nano-pigment exhibiting intense blue color with impressive solar reflectance. Dyes Pigm. 124 (2016) 120-9.
[220] R. Ianoş, E. Muntean, C. Păcurariu, R. Lazău, C. Bandas, G. Delinescu. Combustion synthesis of a blue Co-doped zinc aluminate near-infrared reflective pigment. Dyes Pigm. 142 (2017) 24-31.
[221] S.-t. Liang, H.-l. Zhang, M.-t. Luo, H.-x. Liu, Y.-l. Bai, H.-b. Xu, et al. Preparation of Cr2O3-based pigments with high NIR reflectance via thermal decomposition of CrOOH. Trans Nonferrous Met Soc China. 25 (2015) 2646-7.
[222] S. Jose, A. Prakash, S. Laha, S. Natarajan, M.L. Reddy. Green colored nano-pigments derived from Y2BaCuO5: NIR reflective coatings. Dyes Pigm. 107 (2014) 118-26.

[223] P. Thejus, B. Koley, K. Nishanth. An intense purple chromophore based on Co2+ in distorted tetrahedral coordination. Dyes Pigm. 158 (2018) 267-76.
[224] J. Chen, Y. Xiao, B. Huang, X. Sun. Sustainable cool pigments based on iron and tungsten co-doped lanthanum cerium oxide with high NIR reflectance for energy saving. Dyes Pigm. 154 (2018) 1-7.
[225] B. Huang, Y. Xiao, H. Zhou, J. Chen, X. Sun. Synthesis and characterization of yellow pigments of Bi1. 7RE0. 3W0. 7Mo0. 3O6 (RE= Y, Yb, Gd, Lu) with high NIR reflectance. ACS Sustainable Chem Eng. 6 (2018) 10735-41.
[226] A.K. Raj, P.P. Rao, S. Sameera, S. Divya. Pigments based on terbium-doped yttrium cerate with high NIR reflectance for cool roof and surface coating applications. Dyes Pigm. 122 (2015) 116-25.
[227] W. Zhou, Y. Liu, Q. Sun, J. Ye, L. Chen, J. Wang, et al. High Near-Infrared Reflectance Orange Pigments of Fe-Doped La2W2O9: Preparation, Characterization, and Energy Consumption Simulation. ACS Sustainable Chem Eng. 9 (2021) 12385-93.
[228] B. Bae, N. Takeuchi, S. Tamura, N. Imanaka. Environmentally friendly orange pigments based on hexagonal perovskite-type compounds and their high NIR reflectivity. Dyes Pigm. 147 (2017) 523-8.
[229] V. Elakkiya, S. Sumathi. Ce and Fe doped gahnite: Cost effective solar reflective pigment for cool coating applications. J Alloys Compd. 820 (2020) 153174.
[230] D. Schildhammer, G. Fuhrmann, L. Petschnig, H. Schottenberger, H. Huppertz. Synthesis and optical properties of new highly NIR reflective inorganic pigments RE6Mo2O15 (RE= Tb, Dy, Ho, Er). Dyes Pigm. 140 (2017) 22-8.
[231] R. Yang, A. Han, M. Ye, X. Chen, L. Yuan. Synthesis, characterization and thermal performance of Fe/N co-doped MgTiO3 as a novel high near-infrared reflective pigment. Sol Energy Mater Sol Cells. 160 (2017) 307-18.
[232] J. Chen, W. Xie, X. Guo, B. Huang, Y. Xiao, X. Sun. Near infrared reflective pigments based on Bi3YO6 for heat insulation. Ceram Int. 46 (2020) 24575-84.
[233] P. Thejus, K. Krishnapriya, K. Nishanth. A cost-effective intense blue colour inorganic pigment for multifunctional cool roof and anticorrosive coatings. Sol Energy Mater Sol Cells. 219 (2021) 110778.
[234] P. Meenakshi, M. Selvaraj. Bismuth titanate as an infrared reflective pigment for cool roof coating. Sol Energy Mater Sol Cells. 174 (2018) 530-7.
[235] M. Jovaní, A. Sanz, H. Beltrán-Mir, E. Cordoncillo. New red-shade environmental-friendly multifunctional pigment based on Tb and Fe doped Y2Zr2O7 for ceramic applications and cool roof coatings. Dyes Pigm. 133 (2016) 33-40.
[236] T. Wang, Y. Zhang, M. Chen, M. Gu, L. Wu. Scalable and waterborne titanium-dioxide-free thermochromic coatings for self-adaptive passive radiative cooling and heating. Cell Reports Physical Science. 3 (2022) 100782.
[237] P. Thejus, K. Krishnapriya, K. Nishanth. NIR reflective, anticorrosive magenta pigment for energy saving sustainable building coatings. Sol Energy. 222 (2021) 103-14.
[238] L. Yuan, A. Han, M. Ye, X. Chen, C. Ding, L. Yao. Preparation, characterization and thermal performance evaluation of coating colored with NIR reflective pigments: BiVO4 coated mica-titanium oxide. Sol Energy. 163 (2018) 453-60.
[239] H. Cheng, F. Wang, H. Liu, J. Ou, W. Li, R. Xue. Fabrication and properties of thermochromic superhydrophobic coatings. Adv Eng Mater. 24 (2022) 2100647.
[240] Y. Zhang, X. Zhai. Preparation and testing of thermochromic coatings for buildings. Sol Energy. 191 (2019) 540-8.
[241] Z. Yuxuan, Z. Yunyun, Y. Jianrong, Z. Xiaoqiang. Energy saving performance of thermochromic coatings with different colors for buildings. Energy Build. 215 (2020) 109920.
[242] U. Berardi, M. Garai, T. Morselli. Preparation and assessment of the potential energy

savings of thermochromic and cool coatings considering inter-building effects. Sol Energy. 209 (2020) 493-504.
[243] H. Liu, T. Jiang, F. Wang, J. Ou, W. Li. Thermochromic superhydrophobic coatings for building energy conservation. Energy Build. 251 (2021) 111374.
[244] G. Zeng, J. Yang, R. Hong, Z. Li, Y. Chen, F. Li, et al. Preparation and thermal reflectivity of nickel antimony titanium yellow rutile coated hollow glass microspheres composite pigment. Ceram Int. 44 (2018) 8788-94.
[245] S.P. Radhika, K.J. Sreeram, B. Unni Nair. Mo-doped cerium gadolinium oxide as environmentally sustainable yellow pigments. ACS Sustainable Chem Eng. 2 (2014) 1251-6.
[246] S. Radhika, K.J. Sreeram, B.U. Nair. Effective synthesis route for red-brown pigments based on Ce–Pr–Fe–O and their potential application for near infrared reflective surface coating. J Chem Sci. 126 (2014) 65-73.
[247] Z. Tao, W. Zhang, Y. Huang, D. Wei, H.J. Seo. A novel pyrophosphate BaCr2 (P2O7) 2 as green pigment with high NIR solar reflectance and durable chemical stability. Solid State Sci. 34 (2014) 78-84.
[248] R. Ianoş, E. Muntean, R. Lazău, R. Băbuță, E.-A. Moacă, C. Păcurariu, et al. One-step synthesis of near-infrared reflective brown pigments based on iron-doped lanthanum aluminate, LaAl1-xFexO3. Dyes Pigm. 152 (2018) 105-11.
[249] S. Jose, M.L. Reddy. Lanthanum–strontium copper silicates as intense blue inorganic pigments with high near-infrared reflectance. Dyes Pigm. 98 (2013) 540-6.
[250] J. Li, S. Lorger, J.K. Stalick, A.W. Sleight, M. Subramanian. From serendipity to rational design: tuning the blue trigonal bipyramidal Mn3+ chromophore to violet and purple through application of chemical pressure. Inorg Chem. 55 (2016) 9798-804.
[251] A. Han, M. Ye, M. Zhao, J. Liao, T. Wu. Crystal structure, chromatic and near-infrared reflective properties of iron doped YMnO3 compounds as colored cool pigments. Dyes Pigm. 99 (2013) 527-30.
[252] X. Zhao, Y. Zhang, Y. Huang, H. Gong, J. Zhao. Synthesis and characterization of neodymium doped yttrium molybdate high NIR reflective nano pigments. Dyes Pigm. 116 (2015) 119-23.
[253] R. Lambourne, T.A. Strivens. Paint and surface coatings: theory and practice. Elsevier1999.
[254] W. Freitag, D. Stoye. Paints, coatings and solvents. John Wiley & Sons2008.
[255] Y. Shi, Z. Song, W. Zhang, J. Song, J. Qu, Z. Wang, et al. Physicochemical properties of dirt-resistant cool white coatings for building energy efficiency. Sol Energy Mater Sol Cells. 110 (2013) 133-9.
[256] S. Samal, S. Mohanty, S.K. Nayak. Superhydrophobic Polymer Coatings: Fundamentals, Design, Fabrication, and Applications. Elsevier2019.